PARTICLE SIZES IN SATURN'S MAIN RINGS, AS REVEALED BY CASSINI-VIMS, AND DYNAMICAL MODELING OF HYPERION

A Dissertation

Presented to the Faculty of the Graduate School

of Cornell University

in Partial Fulfillment of the Requirements for the Degree of

Doctor of Philosophy

by

Rebecca A Harbison

January 2014

PARTICLE SIZES IN SATURN'S MAIN RINGS, AS REVEALED BY

CASSINI-VIMS, AND DYNAMICAL MODELING OF HYPERION

Rebecca A Harbison, Ph.D.

Cornell University 2014

The Cassini spacecraft, which entered orbit around Saturn in 2004, has provided a wealth of observations at resolutions and geometries unavailable from Earth, thereby expanding our knowledge of the Saturnian system. In this work, I study both Saturn's extensive ring system and one of its moons, Hyperion.

Previous Voyager and ground-based work had shown that Hyperion, unlike nearly all inner satellites of the giant planets, rotates asynchronously and about a non-principal axis, as a result of strongly-varying tides from Saturn. Modeling done by Wisdom et al. (1984) showed that Hyperion's rotation was also changing in a chaotic fashion over timescales of several months, making it difficult to predict the moon's past and future orientation from only the Voyager flyby. However, in 2005, Cassini performed three close flybys of Hyperion within the Lyapunov timescale. Not only did this let me construct a model of Hyperion's spin state covering much of 2005, it offered clues to Hyperion's interior structure. Because the effect of Saturn's tidal torques on Hyperion's spin depend on Hyperion's internal structure, I could rule out some internal structures if they could not reproduce the changes in spin state in 2005. In particular, a uniform-density model produces a poor fit to observations, as do models in which the principal axes of rotation align with those expected from Hyperion's shape. Hyperion's lack of apparent in-body precession in 2005 suggests either an unlikely coincidence or that an actual principal axis of rotation is closely aligned with

the spin axis.

With regard to studies of Saturn's rings, Cassini's orbit about Saturn not only permits many more stellar occultations of the rings to be observed than can be seen from Earth, but allow for solar occultations of the rings, a geometry impossible to achieve from Earth. Both the actual resolution of the Visible-Infrared Mapping Spectrometer (VIMS) instrument and the resolution gained from translating the star's apparent motion behind the rings into angular resolution permit the diffraction of sunlight or starlight by ring particles to be observed, thus giving information about the size distribution of ring particles in certain areas of the rings. In this work, I measure both the minimum particle size of the A and C Rings, as well as the outermost edge of the B Ring, and the slopes of regions in the outer A Ring, C Ring, Cassini Division and outer B Ring.

I find that the C Ring contains particles down to $4.1^{+3.1}_{-1.3}$ mm in radius, with a particle-size distribution that can be modeled as a power law with a differential power-law index of ~ 3.0. The outer edge of the B Ring likewise contains particles down to a radius of several millimeters, and has a relatively steep power-law index of ~ 3.4, making it quite different from other studies of other areas of this ring (but rather like the outer edge of the A Ring). I was also able to confirm a shallow ~ 2.8 power-law index for the ring particles in the Cassini Division.

For the A Ring, I report only an upper limit on the minimum particle size of 0.6 mm for the inner and mid-A Ring, and a minimum particle size of 3-7 mm in radius in the outer parts of the A Ring. I confirm the power-law index of 2.9 to 3.0 in the outer A Ring, and discover that in the very outermost portions of the ring, the trans-Keeler region, the power-law index steepens to ~ 3.4 or even steeper. I also discovered that the effect of the A Ring's self gravity wakes – temporary aggregates of ring particles in to 50-100 m structures – makes a

noticeable difference in any attempt to model the ring's particle-size distribution in the inner and mid A Ring, but that wakes appear to play little role near the edges of the two gaps in the A Ring, and at the A Ring's outer edge.

BIOGRAPHICAL SKETCH

Rebecca Harbison was born in Boston, Massachusetts, on February 27th, 1984. After moving around somewhat as a child, her family settled in Lincoln, Nebraska, where, under the suburban skies, Rebecca learned her constellations and used her first telescope. She attended the University of Nebraska, Lincoln campus, from August 2001 to May 2005, where she gained a Bachelor of Science degree in Physics and Mathematics. She took full advantage of replacing as many physics courses as possible with astronomy courses, and spent the summer of 2004 interning at the University of Wyoming under Dr. Daniel Dale.

Rebecca started graduate school at Cornell in August of 2005, gained her Master of Science degree in August of 2008, and, after eight years, she is finally finished.

To my parents: Dad for encouraging my scientific interests (and a lot of nights spent helping with homework and days tramping around the wilds of Nebraska looking for birds) and Mom for making sure I was safe and happy and taken care of, from infancy until now.

To my adviser and research group, for encouragement and generally being a good group of people to work with.

And to my friends, for mental health and cheerleading.

ACKNOWLEDGEMENTS

TABLE OF CONTENTS

LIST OF TABLES

LIST OF FIGURES

CHAPTER 1

INTRODUCTION TO RING PARTICLE SIZES

1.1 Overview

Saturn's Main Rings are one of the most spectacular features of the Solar System. The Main Rings are composed of particles with a wide range of sizes, all orbiting the planet, and composed of mostly water ice, with impurities that act to color and darken the rings (Nicholson et al., 2008). Because the ring particles range in size over several orders of magnitude, no one technique can be used to measure the complete particle-size distribution. As a result, the work of defining the properties of ring particles includes observations using a variety of techniques and at a variety of wavelengths.

We speak of Saturn's Rings, especially the bright Main Rings as an aggregate region, but the rings are traditionally broken into a number of units based on observed boundaries in optical depth and color. The Main Rings themselves are defined as the A, B and C Rings, and the Cassini Division. I will briefly outline the regions, with their most notable features. For more details on the rings themselves, I suggest reviewing *Saturn from Cassini-Huygens*, chapters 13 through 15. The basic 'geography' of the rings is shown in Figure 1.1.
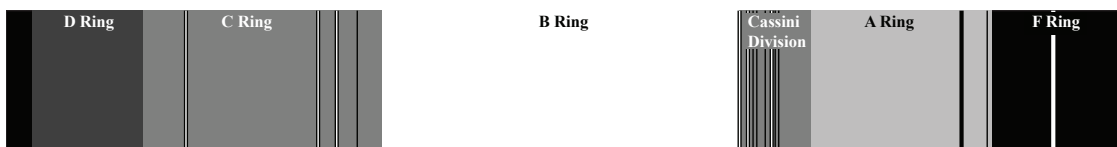
Figure 1.1: A to-scale diagram of Saturn's rings, with major regions labeled and gaps and ringlets drawn on (but unlabeled).

Saturn's C Ring extends from 74,658 to 92,000 km from the planet's center. Interior to the C Ring is only the tenuous D Ring, which I will not be discussing here. The C Ring is mostly optically thin (having an optical depth of less than unity), with various curious structures in optical depth that are not fully understood. The C Ring also hosts several gaps in it. The Colombo Gap, in the inner C Ring, is a 150 kilometer-wide gap at the 0:1 resonance with Saturn's moon, Titan – the location where the orbital period of ring particles equals the orbital precession period of Titan – and includes the Titan Ringlet, a 25-km dense eccentric ringlet that maintains a constant orientation relative to Titan. In the outer C Ring, there is a series of three gaps – the Maxwell, Bond and Dawes Gaps – the inner two of which also contain non-circular ringlets. Finally, just interior to the boundary between the C and B Rings, is a mostly-featureless, increasingly dense region known as the C Ring ramp.

The B Ring extends from 92,000 to 117,580 km, and is the most massive and optically thickest part of the ring system, so much so that many places in the central B Ring appear opaque. It has a complex internal structure, with several distinct sub-regions, that is not fully understood, with the ring's own self-gravity likely contributing to the structure. The outer edge of the B Ring is defined by the inner edge of the Huygens Gap, which occurs at the 2:1 resonance with Saturn's moon, Mimas. There are no gaps within the B Ring.

The Cassini Division is another optically thin region that extends from the Huygens Gap to the Cassini Division ramp, or from 117,580 to 122,170 km. In many ways, the Cassini Division and C Ring are analogous. Within the Cassini Division, there are many gaps – the Huygens, Herschel, Russell, Jeffreys, Kuiper, Laplace, Bessel and Barnard Gaps. The Huygens, Herschel and

Laplace Gaps contain dense non-circular ringlets that take their name from their gaps. Finally, like the C Ring, the outer Cassini Division – beyond the Barnard Gap – has a ramp of increasing optical depth just interior to the A Ring.

The A Ring is denser than the C Ring and Cassini Division, but much less opaque than the B Ring. It extends from 122,170 to 136,775 km, making it the outermost of the Main Rings. Unlike the B Ring, the A Ring is mostly smoothly varying in optical depth, with the dominant features being density and bending waves driven by Saturn's moons. The A Ring has an optical depth which is dependent on viewing geometry, due to the ring's self-gravity arranging the larger particles into roughly linear 'self-gravity wakes'. The outer A Ring contains two gaps, the Encke and Keeler Gaps, both kept open by 10 kilometer-sized moons, Pan and Daphnis, which orbit within the ring system.

Finally, though it is not part of the Main Rings, the F Ring at 140,180 km is addressed briefly in this work, as it is a sort of 'intermediate form' between the denser Main Rings and the diffuse, dusty rings. The F Ring has a core of dense material, with a diffuse halo of dust-sized grains surrounding it, and two moons, Pandora and Prometheus, which may act to confine the core (and create structure that is beyond the scope of this work).

1.2 Radio and Submillimeter Observations

A major constraint on the size distribution of ring particles comes from looking at which wavelengths of light the rings are capable of interacting with. While the rings both reflect sunlight and 'Saturn-shine' and emit thermally in the mid to far-infrared, ring particles are poor at emitting light with a wavelength that is

of the order of their radius or longer. Thus, observations of the rings' emission at sub-millimeter to centimeter wavelengths provide an estimate of the amount of dust, sand and pebble-sized grains within the ring, and constrain the size of the smallest ring particles.

Modeling such data depends not only on the ring particle sizes – particles significantly smaller than the wavelengths observed will not strongly emit, reflect or absorb – but also the optical properties (and hence, composition) of the ring particles, which also sets the ability to see the rings in emission/absorption versus reflection/scattering. The most comprehensive models using exclusively Earth-based data concluded that the majority of the rings' cross-sectional area was provided by ring particles smaller than one meter, but larger than one millimeter, and likely made largely of water ice (with metallic iron fitting the data but considered less likely due to abundance arguments) (Cuzzi and Pollack, 1978; Cuzzi et al., 1980). Cuzzi et al. (1980) note that their conclusions are *not* that such large or small ring particles do not exist, but that they are not the dominant source of opacity. Further radar work has concluded that much of the A and B rings are made of decimeter or meter-sized particles of water ice that can interact with the 12.6 cm radio waves sent from Earth, and that the C Ring and Cassini Division may contain a larger fraction of centimeter and smaller-sized particles to explain the difficulty in observing them in 12.6 cm radio reflection (Nicholson et al., 2005).

With the advent of spacecraft-based observations, scientists have been able to not only rely on passive and reflectivity measurements of the rings at long wavelengths, but to perform absorption and scattering experiments using the spacecraft as a radio source and the Deep Space Network antennae on Earth as

the receivers. The spacecraft would transmit radio waves as it travelled behind the rings from Earth's perspective, and the resulting signal could be analyzed. The Voyager 1 spacecraft performed this experiment once as part of its flyby in 1980, and the Cassini spacecraft has been performing regular radio occultations as part of its ongoing mission since its arrival in the Saturn system in 2004.

As both Voyager and Cassini transmit at several wavelengths – 3.6 and 13 cm for Voyager, and 0.94, 3.6 and 13 cm for Cassini – the simplest thing to examine is the differential optical depth with respect to wavelength. Particles smaller than about one-third of the wavelength of the signal are effectively transparent, as a result, the factor of ~ 3 for Voyager or ~ 14 for Cassini can provide an estimate of what fraction of ring surface area is transparent to longer-wavelength radio waves, providing an estimate of the particle surface area (and thus, number density) between two radius bins. Furthermore, a comparison between the shortest radio wavelength and optical depth measurements in the visible, infrared or ultraviolet can offer the fraction of ring material smaller than the shortest-wavelength radio on board the spacecraft.

When comparing between optical depth data sets, care must be taken to allow for the effects of scattering. When light interacts with a sheet of ring particles, a portion of it is absorbed, a portion is diffracted at a range of angles, and the rest is transmitted. Depending on the wavelength, size of the ring particles, and properties of the appropriate receiver, the diffracted light may or may not be seen. Thus, the observed optical depth, τ, is

$$\tau = \int Q(a, \lambda) \pi a^2 n(a) \, da, \tag{1.1}$$

where $n(a)$ is the differential size distribution of particles of radius a and Q is

the extinction efficiency of particles of this radius, and is between 0 (for particles much smaller than the observation wavelength) and 2 (for particles much larger than the observation wavelength). Papers such as French and Nicholson (2000) also define a Q_{occ} – the extinction efficiency of an occultation – which is not only dependent on the size of particles relative to the wavelength, but also the properties of the detector (specifically if it can distinguish diffracted light).

In the case of measuring the radio optical depth, the monochromatic, directly transmitted signal can often be cleanly separated from the scattered signal either because it is removed from the beam, or by the scattered signal having a Doppler shift induced by interacting with the ring particles. Thus, optical depths within the rings, as measured by radio occultations, are usually extinction optical depths ($Q_{occ} = 2$). The smaller diffraction angles of UV/Visible/IR radiation mean that diffracted light is usually indistinguishable from the transmitted light, so the absorption optical depth ($Q_{occ} = 1$, also called the geometric optical depth) is measured. The intermediate cases – where Q_{occ} is between 1 and 2 – are of the most interest in determining $n(r)$.

The diffraction lobe can also be measured more directly for larger particles. The theory of this work was discussed first by Marouf et al. (1982), and I will only briefly allude to it here. As the beam is diffracted by ring particles, it is Doppler-shifted by the ring's orbital velocity. This separates the diffracted signal from the direct signal when the signal is analyzed spectrally. The average diffracted signal can be inverted to regain an angular scattering function for a given ring region. As the transmitter's beam is not infinitely well-collimated, particles that scatter at angles larger than the beam half-width will appear to scatter isotropically within the beam without changing the shape of the diffrac-

tion lobe. Thus, particles smaller than a minimum size (approximately 1m for the 3-4 meter diameter antennae used by Voyager and Cassini) determined by this angle must be measured by the optical depth method mentioned above, or by other experiments.

The analysis of the Voyager radio occultation was initiated by Marouf et al. (1983), with Zebker et al. (1985) presenting a more detailed model that better accounted for the finite thickness of the rings. Zebker et al. (1985) were able to measure eight regions of the ring – the middle C ring, the C Ring ramp, the Cassini Division ramp, three zones in the mid-A Ring and the trans-Encke A Ring. The same basic properties of the ring particle-size distribution appear in all these regions. As Zebker et al. (1985) had only two measurements of optical depth (plus the inversions of the scattering function), they elected to model the particle-size distribution for particles smaller than 1 meter as a truncated power law, written as

$$n\left(r\right) = n_0 a^{-q} \; a_{\min} \le r \le a_{\max}, \tag{1.2}$$

where the entire particle-size distribution is parameterized by $a_{\min}$, $a_{\max}$, n_0, and q. For particles smaller than one meter, the particle-size distribution appears roughly inverse-cubic ($q \approx 3$), but direct inversion shows a steepening at a particle size of 3-10 meters, where the distribution goes from a power-law index of 3 to $4-5$ or even larger, representing a de-facto cutoff. Furthermore, all ring regions show a greater optical depth at 3.6 cm than at 13 cm, indicating some ring particles down to ≈ 1 centimeter in size.

Marouf et al. (1983) and Zebker et al. (1985) were able to convert the radio optical depth measurements, and the inversions, into a estimate of the power-

law index by assuming a truncated power-law particle-size distribution with a minimum cutoff of 1 cm. Zebker et al. (1985) chose to fix $a_{\min}$ at 1 cm due to their limited sensitivity to smaller particles, and $a_{\max}$ at 1 m (the point at which Marouf et al.'s inversions could take over). They chose n_0 such that the power law plus the inversions would lead to the correct total optical depth of the ring region. Thus, they transformed a differential optical depth into a unique power-law index, q. From this, they derived a power-law index of 3.0-3.1 for the C ring regions, a steepening power law from 2.7 to 3.03 for the A Ring, and a single measurement of an index of 2.79 for the Cassini Division ramp.

The Cassini radio occultation experiments had many improvements over their Voyager counterpart: Voyager had passed through when the rings were relatively edge-on to Earth (about a 6° opening angle), while Cassini arrived when the rings were relatively open (over 20° opening angle). Cassini also could transmit at three wavelengths to Voyager's two. In addition to the smaller particles the 0.94 cm Ka-band signal was sensitive to, having three optical depth measurements breaks the degeneracy between the power-law index and minimum particle size that meant the Voyager RSS (Radio Science Subsystem) team had to assume a lower size cutoff. Finally, Cassini's insertion into Saturnian orbit meant that the experiment could be repeated, including under differing geometries both for better signal-to-noise and to sample ring regions of varying optical depth. Preliminary results from differential optical depths were presented by Marouf et al. (2008), and included in the 'Ring Particle Composition and Size Distribution' chapter of *Saturn from Cassini* (Cuzzi et al., 2009). To date, no inversions of the Cassini radio occultations have been published.

Marouf et al. (2008) report a slightly higher power-law index of $q = 3.2$ in

the C Ring than in the previous Voyager result, with a robust minimum particle radius of 4mm in the mid C Ring. The more open geometries permitted observation of all but the densest part of the B Ring (the 'core', also called B3). The innermost B ring (B1) looks much like the C Ring ramp, with a minimum particle size of 4mm, and a power-law index of 3-3.1. The regions bordering B3 (called B2 and B4) appear to either have a very shallow power-law index of less than 2.7 or contain no free ring particles smaller than half a meter – both regions yield negligible optical depth increases at shorter wavelengths. In the Cassini Division, Marouf et al. (2008) report an increasing maximum particle size with radius, but no new results on the power-law index or minimum particle size. Within the A Ring, Marouf et al. (2008) report a power law steepening from 2.7 to as high as 3.2, increasing with distance from Saturn. The shallow power law in the inner and mid A Ring make it difficult to estimate the minimum particle radius, as explained in the previous paragraph, but Marouf et al. (2008) report a minimum particle size of 20 cm in the inner A ring and a minimum particle size of 4-5 mm in the steeper trans-Encke region where the smallest particles are easier to see.

1.3   Photometry and Spectroscopy

The differential optical depth measurements mentioned in Section 1.2 can be extended to shorter wavelengths, though this requires some cross-calibration of instruments. French and Nicholson (2000) note that the Voyager photopolarimeter (PPS) occultation of the star δ Scorpii (δ Sco), done in the ultraviolet ($\sim$ 270 nm) is mostly comparable in geometric optical depth to the geometric optical depth calculated from the RSS occultation at 3.6 cm, with a scaling factor of 0.9

required in the A Ring, implying that in most regions of the ring, there is an insignificant ring surface area due to free particles smaller than a few centimeters in size.

The phase function of the rings can also tell us something of the particle size, as grains of the order of microns or tens of microns (dust-sized grains) forward-scatter light strongly in visible and near-infrared light, while macroscopic ring particles do not. These measurements have been done by both Voyager and Cassini, as the viewing geometry from Earth covers only very low phase angles. Doyle et al. (1989) and Dones et al. (1993) were able to show that the A and B Rings were mostly dust-free using phase functions derived from Voyager images. Cooke (1991) produced similar results in the C Ring, though their phase function had an element of forward-scattering that they attributed to either free dust-sized grains within the C Ring or surface roughness on larger ring particles.

While Cassini observations have identified a few narrow ringlets within the Main Rings (Hedman et al., 2007b, 2010a) and the D Ring (Hedman et al., 2007a) that contain dust-sized grains, and the transitory 'spokes' of the B Ring show a phase function consistent with dust grains (Mitchell et al., 2006), the majority of the Main Rings show a phase function that is strongly backscattering, indicating macroscopic particles. The depths of the water ice bands in the near-infrared *reflectance* spectra suggest grain sizes of a few tens of microns (Nicholson et al., 2008; Filacchione et al., 2012, 2013), but these are interpreted as referring to regolith grains on the surfaces of much larger ring particles.

1.4 Stellar Occultations

Before Cassini arrived at Saturn, data from stellar occultations of the rings were of limited use for deriving ring particle sizes. Voyager did observe an occultation of δ Sco using the PPS and UVS instruments at near-UV wavelengths. In addition, the 1989 occultation of 28 Sagitarii (28 Sgr) was observed from a number of Earth-based observatories in the visible and near-infrared.

The Voyager PPS observations were analyzed for the effects of the largest ring particles statistically. The occultation was observed at a time resolution of 10 ms, which translated to a spatial resolution of 100 m at the rings. If ring particles existed on that size scale, they would reveal themselves in the structure of the point-to-point variation of the occultation counts. A certain amount of variation would be expected from photon-counting statistics, quantified by the statistical variance $\sigma_{ph} = \sqrt{N}$, where N is the mean photon count rate, but a larger variance than expected from counting noise would be produced if the ring particles were large enough that the presence of individual large ring particles could effect the transmission from sample to sample. Showalter and Nicholson (1990) were able to show that, in fact, regions of the ring did show extra variance that suggested the presence of meter to decameter sized ring particles. However, this work was done before the presence of the self-gravity wakes of the A Ring and the more complex aggregates of the B Ring were theorized, though Showalter and Nicholson did note the possibility of aggregates in the A Ring as a caveat to their work. As a result, it seems likely that Showalter and Nicholson's results were influenced, if not dominated, by aggregates, at least for the A and B Rings. They observed an effective ring particle size of $\lesssim 1.1 - 2.8$ meters in the C Ring and $\lesssim 1.1 - 4.5$ m in the Cassini Division, regions which are not dense enough

to form such aggregates, confirming the presence of meter-sized ring particles (and the relative lack of larger ring particles).

French and Nicholson (2000) used a different method to analyze the 28 Sgr data obtained from the Lick Observatory at 0.9 μm, the McDonald Observatory at 2.1 μm, and the Palomar Observatory at 3.9 μm. Like the radio occultations discussed in Section 1.2, Earth-based stellar occultations are sensitive to the effects of diffraction as electromagnetic radiation shines through the rings. However, a star that emits incoherent broad-spectrum ultraviolet, visible and/or near-infrared light is quite a different source than a coherent radio source emitting narrow-spectrum radio waves, and the instruments required to detect such light are quite different. The Doppler effect method used to separate diffracted radio waves from those directly transmitted is useless, as both the stellar spectrum and the photometric filters used at the telescopes are far too broad to separate a Doppler-shifted diffraction lobe on top of the transmitted light. Furthermore, the wavelengths involved mean that the relevant angular scales are quite different – a meter-sized ring particle will diffract 13 cm radio waves by a substantial ten milliradians (or $\sim 30'$), while the same ring particle will diffract near-infrared light by about a microradian, four orders of magnitude smaller. Thankfully, the same effect that shrinks diffraction angles also acts on the receiver's angular resolution: an optical telescope can often resolve sources to ten-microradian precision (or $\sim 2''$). However, French and Nicholson (2000) did not attempt to resolve the diffracted signal directly, due to the effect of time-variable atmospheric seeing. Instead, they examined optical data derived from aperture photometry.

While some evidence of diffracted light could be seen in the raw occulta-

tion data – the presence of 'overshoots' or 'horns' where starlight scattered from nearby ring material would make it appear as if the star had brightened above 100% transmission as it passed through a gap – the diffracted light was indistinguishable from the directly transmitted light in most of the data set. Thus, the occultation was modeled by using a difference in optical depth measurements. The Voyager PPS occultation was used to produce a geometric normal optical depth profile of the rings, which allowed the directly transmitted light to be estimated, and thus separated from the diffracted light. Given the geometry of the occultation and the wavelengths and aperture sizes used to observe it, a model of scattered light could be created for a given particle-size distribution and this model could be fit to the data. French and Nicholson (2000) chose to model the ring as five regions – the C Ring, B Ring, Cassini Division, inner-to-mid A Ring, and trans-Keeler A Ring – each with a truncated power-law size distribution, as described in the previous section.

French and Nicholson (2000) noted that the C Ring showed a comparatively larger fraction of surface area in small particles, and set their power-law index to 3.1 and their particle size range from 1cm to 10 m to best fit the levels of scattered light seen. They noted that this did not fit all their data – particularly the 0.9 μm observations taken at Lick Observatory – and suggested that the C Ring may not have a uniform power-law index across the entire ring. In the B Ring, they found a similar shallow power law and paucity of small particles that would later be observed by Cassini RSS, and fit a model with a power-law index of 2.75 and a particle size range of 30 cm to 20 m. As in the Cassini RSS data, the B Ring core proved to be too opaque to produce useful results. The relative narrowness of the Cassini Division limited the conclusions to be drawn there, but French and Nicholson (2000) found a power-law index of 2.75 and a

minimum particle size of 1n mm fit best, and chose a maximum particle size of 20 m to match the nearby A Ring, noting that this number is not well constrained by their data.

As in the radio-science experiments, French and Nicholson (2000) noted that the shallow power law of the inner to mid A Ring makes it difficult to constrain the smallest particles, though in their case, they required both a shallow index (2.75) and a large minimum particle radius (30 cm), and found that a maximum particle size of 20m is necessary to reproduce some of the fine structure seen in the scattered light profile; the larger the particles, the smaller the angles they scatter light into, so the less 'smeared out' their scattering profile is. For the outer A Ring, they found a somewhat steeper power law (2.9) and a much smaller minimum particle size (1 cm), though they noted again that the three data sets used did not agree well. Generally speaking, the results inferred so far from the Cassini RSS occultations compare quite well with those from French and Nicholson (2000).

1.5   Direct Imaging

While the average-sized ring particles have not been resolved, even in spacecraft-based imaging observations, the effects of the largest individual ring particles can be seen within the A and B Rings. It could even be argued that the resolved moons Pan (with a mean radius of ~14 km) and Daphnis (with a mean radius of ~ 4 km), that orbit within gaps in the A Ring, are the largest 'ring particles'.

Ring particles smaller than Daphnis are unable to clear an entire gap in

the rings, but their gravity still perturbs the ring material around them. The first four such objects were spotted in very high resolution Cassini images obtained during the spacecraft's insertion into Saturn orbit (Tiscareno et al., 2006) as paired lighter 'streaks' in the A Ring, several kilometers long and with the leading streak displaced hundreds of meters inward from the trailing streak. Though Cassini did not resolve the actual moonlets responsible, theoretical work (Spahn et al., 2000; Seiß et al., 2005) had suggested that this pattern was what one would expect from a large ring particle perturbing smaller ring particles by its own gravity, forming density enhancements and depletions shaped much like the blades of a propeller. Many additional 'propeller moonlets' or 'propellers' have been subsequently seen in more modest resolution images (Sremčević et al., 2007; Tiscareno et al., 2008), including several relatively large 'giant propellers' in the region between the Encke and Keeler gaps (Tiscareno et al., 2010a).

While the actual sizes of these 'propeller moonlets' is uncertain, due to photometric effects beyond the scope of this dissertation, it is generally agreed that such features are caused by ring particles in the tens to hundreds of meter size regime (Tiscareno et al., 2006), possibly as large as 1 km (Tiscareno et al., 2010a). Tiscareno et al. (2008) made an attempt to fit the observed 'propeller moonlets' (as well as Pan and Daphnis) to the particle-size distribution in the A Ring, and noted that, given the number of 'propellers' observed in the A Ring, it fit with Zebker et al. (1985)'s assertion that the particle-size distribution of the A Ring steepens greatly at particle sizes larger than ~10 m.

1.6 Theory

Theory has offered some explanation as to why the rings have a clear truncation in their particle-size distribution. Longaretti (1989) modeled the processes of accretion and disruption of ring particles orbiting within the ring, and noticed that, above a certain ring particle radius, collisions between ring particles becomes increasingly disruptive, eroding the largest particles, and suggested similar processes might account for the lower cutoff. Following up on that work, Bodrova et al. (2012) predicted, based on adhesion versus disruption rates in a collisional system with many differently-sized particles, such as the rings, that the smallest particles will selectively stick to the largest particles, such that a sharp break in the free-floating particle-size distribution will form, with all smaller particles spending the majority of their time adhered to larger particles. Bodrova et al. (2012) predicted, using the ring surface densities measured by Cassini and dynamical estimates of relative velocities within the rings, a minimum particle size of centimeters in less dense or more disturbed regions, up to tens of centimeters in the inner A and B rings.

We can certainly see the effect of small particles covering the rings' exposed surfaces. The spectra of the rings observed by Cassini-VIMS show water ice absorption features that resemble those of $\sim$ 30 micron sized ice grains, with colorants that darken and redden the rings' spectra relative to pure water ice (Nicholson et al., 2008). Modeling suggests that the rings are covered in grains with sizes of of 5-100 μm (Filacchione et al., 2012). Morishima et al. (2012), working with CIRS data, was able to extend the spectral modeling of ring regolith into the mid-infrared, and suggested the regolith's particle sizes extended to the range of centimeter sized particles. Thus, we see exactly the sort of regolith

predicted by Bodrova et al.: a wide range of particle sizes, up to the size of the smallest free-floating particles.

1.7 State of Knowledge Prior to This Work

The general consensus before I began my work was that the Main Rings of Saturn could be modeled by a truncated power-law size distribution. The B Ring and inner and middle A Ring were best represented by a power-law index of ~ 2.75 and a relatively narrow particle size range of ~ 30 cm to 10-20 m. Outside of the Encke Gap, the A Ring had a steeper distribution of q = 2.9-3.2 and smaller particles that extended into the difficult-to-measure size range below 1 cm. The C Ring, likewise, had a relatively steep particle-size distribution of q = 3.0-3.2 and a particle size range of 4 mm to 5-10 m. The Cassini Division, due to its narrowness, complex internal structure and low optical depth, was the least well studied. It seemed to show the same shallow (q = 2.75) power-law index as the neighboring A and B Rings, but a particle size range that extended down to centimeter sized particles and up to 5-20 meter sized particles.

A summary of our understanding of the rings' size distribution circa 2008 is shown in Figures 1.2 and 1.3. Note that there is a generally consistent picture of the power-law index over the rings, but the minimum particle size is not well-constrained in the C Ring and trans-Encke A Ring, and is almost totally unknown in the Cassini Division.

After a brief discussion of a separate project on Hyperion's rotation (Chapter 2, originally published in *Celestial Mechanics and Dynamical Astronomy* in 2011), this work will examine the use of occultations in the near-infrared as observed
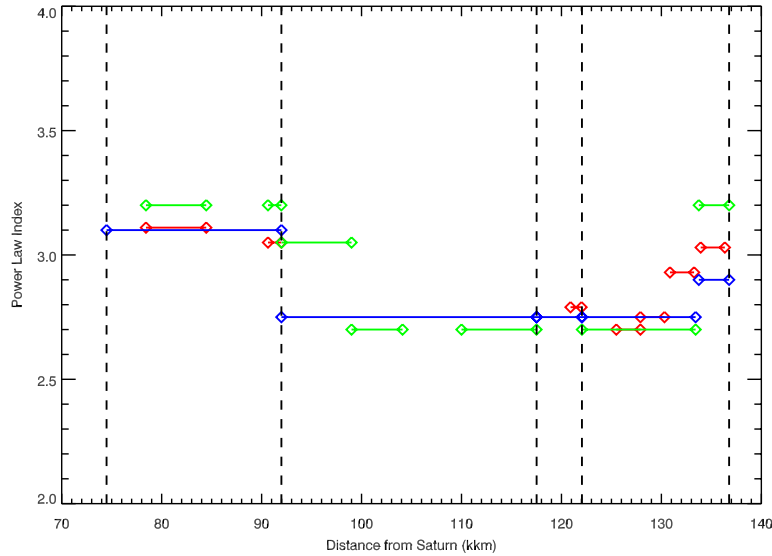
Figure 1.2: A plot of the estimated power-law index of various regions of Saturn's rings using Voyager RSS (red, (Zebker et al., 1985)), Cassini RSS (green, (Marouf et al., 2008)) and Earth-based stellar occultation (blue, (French and Nicholson, 2000)), with diamonds marking endpoints of line segments indicating the regions modeled. Dashed lines mark the boundaries of various ring regions (the C Ring, B Ring, Cassini Division and A Ring). The general trends are that the C Ring and trans-Encke A Ring particles have a steep ($q > 3$) power-law index, while the rest of the ring system has a more shallow power-law index. As French and Nicholson (2000) used the Voyager estimates as a starting place for their work, close agreement may not be surprising.

by the Cassini spacecraft to expand this picture of the Main Rings and the particles that make them up. This dissertation will cover work on solar occultations (Chapter 3, previously published in *Icarus* in 2013) and work on stellar occultations (Chapter 4, in preparation for submission to *Icarus*).
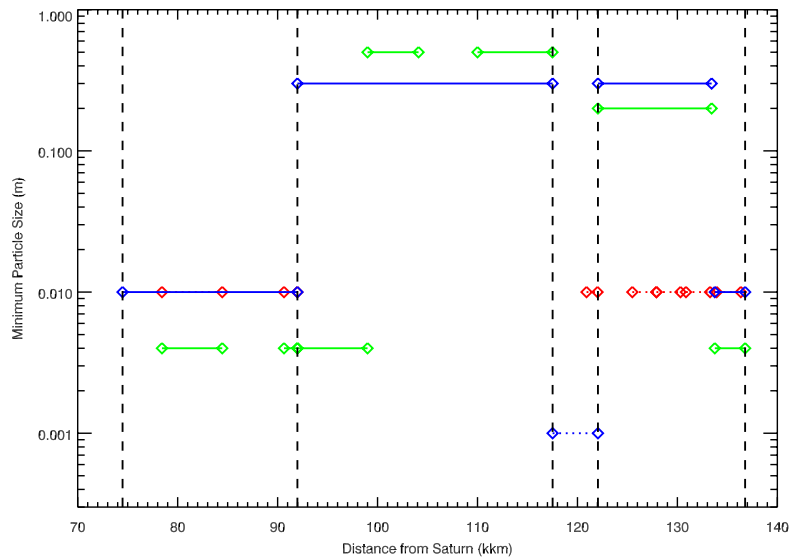
Figure 1.3: A plot of the estimated minimum particle sizes of various regions of Saturn's rings using Cassini RSS (green, (Marouf et al., 2008)) and Earth-based stellar occultation (blue, (French and Nicholson, 2000)), with diamonds marking endpoints of line segments indicating the regions modeled. Dashed lines mark the boundaries of various ring regions (the C Ring, B Ring, Cassini Division and A Ring). Note that the inner A and B rings have minimum particle sizes on the order of decimeters, while the C Ring and trans-Encke A ring particles have minimum sizes in the millimeter range. The Cassini Division is almost totally unconstrained, though French and Nicholson (2000) note they require millimeter-sized particles to best fit their data. The assumed minimum particle size of 1 cm used by Voyager RSS (red dotted line) is also shown.

CHAPTER 2

ROTATIONAL MODELING OF HYPERION. HARBISON, R. A., THOMAS, P. C., & NICHOLSON, P. D., *CELESTIAL MECHANICS AND DYNAMICAL ASTRONOMY*, VOLUME 110, ISSUE 01, 2011.

2.1   Introduction

Since the Voyager era, the Saturnian moon Hyperion has been known observationally to be a non-synchronous rotator. Wisdom et al. (1984) theoretically showed that given Hyperion's large resonantly-forced eccentricity and the non-spherical shape observed by Voyager, the satellite couldn't rotate synchronously and would most likely be in a tumbling state. Large portions of the phase space for its spin state, including many of the low-order spin-orbit resonances, would be chaotic with short (several orbits) Lyapunov timescales.

Despite this, several attempts have been made to model the spin of the moon over short time periods, to determine if the moon's spin state was consistent with that of a homogenous body of its shape. Klavetter (1989) was the first; using ground-based photometry and the Voyager images, he was able to produce fits consistent with a homogenous body, though the limited dimensionality of the data meant he could not guarantee that he had found a unique solution. Starting from the high-resolution Voyager images, Black et al. (1995) were able to model the low-resolution photometry obtained over 18 days prior to the encounter.

The Cassini spacecraft, in orbit around Saturn, made three close passes by Hyperion in 2005. For each fly-by, an instantaneous spin state and partial shape

model were obtained (Thomas et al., 2007). Hyperion's rotational rate was observed to be between 72 and 75° day^{-1} (for comparison, Hyperion's orbital mean motion is 16.94° day^{-1}) and the spin vector was neither constant in space nor within the body. Perturbations to Cassini's orbit indicated Hyperion's mean density to be a surprisingly low 544±50 kg m^{-3}, implying a porosity of at least 42±6 %, assuming pure water ice (Thomas et al., 2007).

Using these three high-resolution passes in 2005, we will search for possible fits of the moments of inertia ratios within the errors set by the shape model. Furthermore, given the porosity of Hyperion, a search for better fits, allowing for the principal axes to vary from those derived from a shape model, will also be done to look for possible large-scale inhomogeneities caused by voidspace or regions of solid ice.

2.2 Data

From the current shape model (Thomas et al., 2007), and assuming a homogenous interior, we obtain dimensionless moments of inertia $A = 0.314 \pm 0.010$, $B = 0.474 \pm 0.008$, and $C = 0.542 \pm 0.008$ in units of $M \langle R \rangle^2$, where M is the mass of Hyperion and $\langle R \rangle$ is mean radius (135 ± 4 km). This gives $A/C = 0.58 \pm 0.03$ and $B/C = 0.87 \pm 0.03$.

Tables 2.1 and 2.2 give data previously presented in Black et al. (1995) and Thomas et al. (2007), as well as 2007 observations first presented in this paper, but obtained by the same methods as used in Thomas et al. (2007). Osculating orbital elements for Hyperion were obtained from JPL's HORIZONS database, and were calculated via numerical integration with initial conditions taken from

							ω_A	ω_B	ω_C	
Date	e	ϖ	M	θ_0	ϕ_0	ψ_0	$/|\omega|$	$|\omega|$	$/|\omega|$	$|\omega|$
2005-06-10	0.115	105°	295°	0.004	1.441	0.427	0.890	0.067	0.451	4.433
2005-08-16	0.115	102°	342°	1.885	2.118	1.180	0.907	0.162	0.389	4.255
2005-09-25	0.113	99°	303°	2.989	1.685	1.641	0.902	0.133	0.411	4.255

Table 2.1: Initial conditions of the orbit and spin at the mid-point of each fly-by. The values of e, ϖ and M were used to derive the distance to Saturn (r) and the true anomaly, f. θ, ϕ and ψ are the calculated Euler angles describing the change of coordinates from the Saturn-centric coordinate system (used to find the influence of torques from Saturn) to the body-centric principal-axis coordinate system (see Section 2.3 and Black et al. (1995)), and the ω's are the angular velocity (in units of orbital frequency) about each of the shape-determined principal axes.

Date	$\omega_A/|\omega|$	$\omega_B/|\omega|$	$\omega_C/|\omega|$	ω_x	ω_y	ω_z	$|\omega|$ (° d^{-1})	σ_ω(°)
1981-08-23	0.986	0.160	-0.049	-2.457	-2.501	2.409	72±3	10
2005-06-10	0.890	0.067	0.451	3.399	-1.511	2.411	75±1	2
2005-08-16	0.907	0.162	0.389	3.026	1.909	2.303	72±1	4
2005-09-25	0.902	0.133	0.411	1.151	2.018	3.565	72±1	10
2007-02-16	0.749	0.080	0.659	-3.797	1.905	0.250	72±1	10

Table 2.2: Rotation state observed during all close flybys of Hyperion, including results presented in Thomas et al. (2007) and Black et al. (1995). Angular velocity measured both in the body-centric frame and in the *xyz* quasi-inertial coordinate frame, with *z* as the direction of Saturn's pole, *x* as the direction from Saturn towards Hyperion's pericenter at the time of the observation, and *y* chosen to form a right-handed coordinate system. All results in the *ABC* frame, save the 1981 data, were calculated with the current shape model; the 1981 data are taken directly from Black et al. (1995), and used the Voyager-era shape model. The total spin frequency (in units of orbital frequency) is also noted, with estimates on the error, as is the error in position of the spin axis in inertia space (in degrees).

Jacobson (1996).

Some things are readily apparent from the measured instantaneous spin states. During all five close fly-bys, Hyperion was observed in a similar state, that of non-principal axis rotation with a spin axis closest to the long shape axis (presumably corresponding to the A principal axis), and 4.2 to 4.4 times faster than synchronous. The three 2005 observations show the same in-body location of the spin axis within errors, though it has moved between 1981, 2005 and 2007. Rotation about the A axis would be dynamically stable when it comes to free-body rotation, but under dissipation and without strong forcing, the rotation should shift to the minimum energy state about the C axis. Indeed, this is what most natural satellites show. However, Black et al. (1995) did perform long-term ($\sim 10^6$ orbit) integrations, showing that the near-A-axis rotational state seen in 1981 (and 2005, and 2007) was not unusual for Hyperion. A similar quasi-stability was seen in rotational models of Prometheus and Pandora done by Melnikov and Shevchenko (2008), where even chaotic solutions to the moons' rotation have a preferred orientation.

Movement of the spin axis in inertial space is also evident, and obvious even on the 40 to 70 day timescale between the 2005 fly-bys. Again, unlike the minimum-energy Cassini state occupied by more regular satellites, Hyperion's spin axis is not confined to near the orbit normal (here, the z axis). Black et al. (1995)'s models showed the expected forced nutation and precession about the orbit normal with a 300-day period, as well as a shorter 10-20 day precession about the A axis, and the 100-day span between the 2005 observations would easily show these motions.

2.3   Dynamical Modeling

The model used to calculate the rotation is a six-dimensional system of differential equations, with three coordinates tracking the angular orientation of Hyperion in space, and three tracking the angular velocity of Hyperion's spin. The full system of equations of motion, taken from Black et al. (1995), is:

$$\dot{\theta}_E \;=\; \frac{\omega_A \sin \psi_E + \omega_B \cos \psi_E}{\sin \phi_E} \tag{2.1}$$

$$\dot{\phi}_E \;=\; \omega_A \cos \psi_E - \omega_B \sin \psi_E \tag{2.2}$$

$$\dot{\psi}_E \;=\; \omega_C - \dot{\theta}_E \cos \phi_E \tag{2.3}$$

$$\dot{\omega}_A \;=\; \frac{B-C}{A}\left(\omega_B \omega_C - \frac{3\beta\gamma}{r^3}\right) \tag{2.4}$$

$$\dot{\omega}_B \;=\; \frac{C-A}{B}\left(\omega_A \omega_C - \frac{3\alpha\gamma}{r^3}\right) \tag{2.5}$$

$$\dot{\omega}_C \;=\; \frac{A-B}{C}\left(\omega_A \omega_B - \frac{3\alpha\beta}{r^3}\right). \tag{2.6}$$

We use the conventional Euler angles (θ_E, ϕ_E, ψ_E) to specify angular position of Hyperion's principal axes, which were computed from the current shape model and the assumption of constant density, relative to the *xyz* axes. Because the Euler angles have a singularity when $\sin \phi$ approaches 0, a transformation to Wisdom's alternate angular coordinates (a set of angles where the third rotation is about the *y* axis, rather than the *z* axis used in conventional Euler angles) is made when $|\sin \phi_E| \leq 10^{-6}$ and we return to the conventional Euler angles when $|\cos \phi_W| \leq 10^{-6}$.(Wisdom et al., 1984) The transforms are:

$$\tan \theta_W \;=\; \frac{\cos \theta_E \sin \psi_E + \sin \theta_E \cos \phi_E \cos \psi_E}{\cos \theta_E \cos \phi_E \cos \psi_E - \sin \theta_E \sin \psi_E} \tag{2.7}$$

24

$$\tan \phi_W = \sin \phi_E \cos \psi_E \tag{2.8}$$

$$\tan \psi_W = \frac{-\sin \phi_E \sin \psi_E}{\cos \phi_E} \tag{2.9}$$

$$\tan \theta_E = \frac{\cos \theta_W \sin \psi_W + \sin \theta_W \sin \phi_W \cos \psi_W}{\cos \theta_W \sin \phi_W \cos \psi_E - \sin \theta_W \sin \psi_W} \tag{2.10}$$

$$\tan \phi_E = \frac{1}{\cos \phi_W \cos \psi_W} \tag{2.11}$$

$$\tan \psi_E = \frac{-\cos \phi_W \sin \psi_W}{\sin \phi_W}. \tag{2.12}$$

Unlike previous work (Wisdom et al., 1984; Black et al., 1995; Melnikov and Shevchenko, 2008), instead of using the derivatives of Euler angles with respect to time as our measure of angular velocity (and thus using equations for the second derivatives of Euler angles to compute the changes in angular velocity), we use the instantaneous angular velocities about the principal axes, ω_A, ω_B and ω_C. This reduces the number of coordinate changes should the problem approach the singular situation of $\sin \phi = 0$, and eliminates the need to convert derivatives of Euler angles into a more physically intuitive coordinate system for display.

The variables α, β, and γ in Eqs. 1-6 are the direction cosines from the principal axes to the instantaneous direction of Saturn, defined as (Black et al., 1995)

$$\alpha = \cos(\theta_E - f)\cos \psi_E - \sin(\theta_E - f)\cos \phi_E \sin \psi_E \tag{2.13}$$

$$= \cos(\theta_W - f)\cos \psi_W - \sin(\theta_W - f)\sin \phi_W \sin \psi_W \tag{2.14}$$

$$\beta = \cos(\theta_E - f)\sin(-\psi_E) - \sin(\theta_E - f)\cos \phi_E \cos \psi_E \tag{2.15}$$

$$= \sin(\theta_W - f)\cos \phi_W \tag{2.16}$$

$$\gamma = \sin(\theta_E - f)\sin \phi_E \tag{2.17}$$

$$= \cos(\theta_W - f)\sin \psi_W + \sin(\theta_W - f)\sin \phi_W \cos \psi_W, \tag{2.18}$$

where f is the true anomaly of Hyperion in its orbit. A, B and C are the values of the shape-derived moments of inertia, and r is the distance between Hyperion and Saturn (in units of $a = 1$). Time is measured in units of $P_{Hyp} = 2\pi$, so that the orbital angular velocity, $n = 1$, and the spin angular velocities are thus measured in multiples of n. In physical units, $P_{Hyp} = 21.43$ days and $a = 1.484 \times 10^6$ km, or 24.6 Saturn radii.

The orbit of Hyperion is modeled as a static (non-precessing) ellipse about a spherical planet in the equatorial plane. Hyperion's orbital inclination is small, and it is sufficiently far from Saturn that its apsidal precessional period due to Saturn's oblateness – the pericenter moves 6° between June and September 2005 – is long compared to the spin, orbital and Lyapunov timescales. Hyperion is in a 3:4 orbital resonance with Titan, which forces additional variations in its eccentricity and longitude of pericenter (Peale, 1999), but the 18.8 year variation in eccentricity (Duriez and Vienne, 1997) again occurs over a much longer timescale than our integrations of its spin state.

The integration of the system of equations (1-6), as well as Hyperion's orbital position and velocity was performed using a fourth-order Runge-Kutta algorithm. The initial conditions, which are presented in Table 2.1, are set by the observations during one of the close fly-bys of Hyperion by Cassini. Initially, the middle observation was used, and the integration was performed in two directions. However, further data analysis showed that the first (June) observation had the lowest uncertainty in spin axis direction and this datum was settled upon as the initial conditions for all runs mentioned in this text. At each step, the orbital position and velocity were calculated using Newton's Laws and substituted into the rotational equations to calculate the torques from Saturn.

Step size was chosen as a compromise between speed of integration and accuracy, and was varied between runs – integrations which need not be compared to data used a step size of $\pi/400$ (1/800th of an orbit, or approximately 1/160th of a rotation), while integrations fitted to the three Cassini observations were subdivided into 5000 steps between June and August (or a step size of 6.28×10^{-4} of an orbit), and another 5000 steps between August and September (or a step size of 3.78×10^{-4} of an orbit) . Tests using larger and smaller step sizes produced comparable results, with steps a quarter, a half and double the length not producing quantifiably different (within the output precision) results, while steps four times as long showed less than one part in 10^4 difference in spin rate over 100 days.
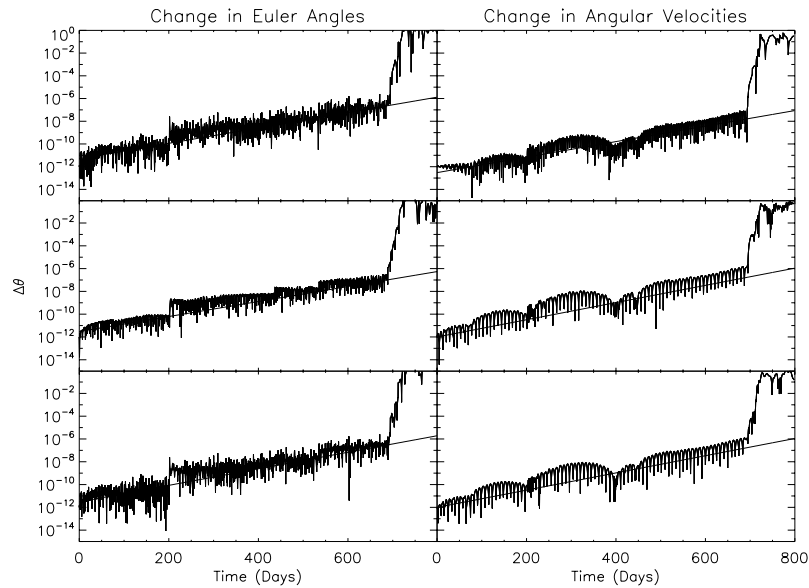
Figure 2.1: Relative differences in rates and principal axis orientations ω and θ as functions of time (in days), starting from a difference of 10^{-12} (machine double precision). The behavior for the first 700 days is roughly exponential, as expected for a chaotic system, with similar Lyapunov exponents, producing a mean exponential-growth timescale of 61.4 ± 3.6 days.

As a test of our integration code and in order to find the Lyapunov timescale,

the inputs were perturbed by one part in 10^{12} and four integrations offset in different directions in parameter-space from a fifth were compared for a period of 800 days. The difference in Euler angles and angular velocities between one such run and the 'reference' integration are plotted versus time in Fig. 2.1, where they show a good fit to the chaotic behavior expected, growing exponentially with respect to time (and appearing linear in the semi-log plot). Fitting the slope of the divergence between solutions with respect to time to an exponential function returns a Lyapunov time of 61.4 ± 3.6 days. While this timescale is slightly longer than that reported by Wisdom et al. (1984), who assumed a near-synchronous initial state, they do show that dynamical models cannot be expected to be predictive over a period of more than a few months.

The first run of the model started from the June 2005 (Day 161) fly-by, and extrapolated Hyperion's rotation forward (and backward) in time. The reported error of the spin axis's position is 2° in the June 2005 measurement, as seen in Table 2.2. Given the measured Lyapunov timescale, the error in the predicted spin axis direction should grow to 6° at the time of the August fly-by and 11° in September. Both of these numbers are larger than the uncertainties in the observations, but not significantly so, making it possible to compare the observations with the model's results as long as the effects of the chaos are kept in mind.

The results, shown by the magnitude of the spin and the decomposition of the spin along the shape model's axes, are plotted versus time in Fig. 2.2. Note that the spin rate predicted by the model fits the September 2005 (day 268) datum quite well, though it is noticeably different than the August 2005 (day 228) observation. However, the position of the spin axis within the body – as seen in the decomposition of the spin rate into its A, B, and C components – does not
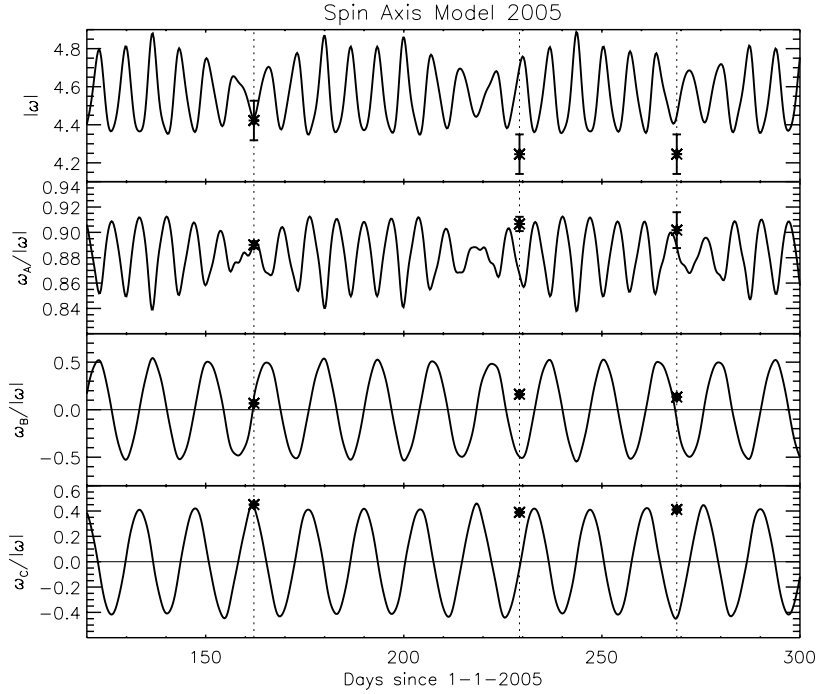
Figure 2.2: Model of the spin rate and position of the spin axis in body-centric coordinates – using as measures the component of spin around each principal axis – starting from the June 2005 observation and progressing forward for approximately 140 days, using the Thomas et al. (2007) values for A, B, and C. All three observations are marked as points on the graph. Note the predicted period of about 16 days in ω_B and ω_C and 8 days in ω_A, and the near-identical values of the three observations compared to the large variations in ω_B and ω_C predicted by the integration.

match the observations well. It is observed to stay relatively fixed, while the model predicts it to precess about the A axis, with a period of about 16 days. This was also seen by Black et al. (1995), who calculated a theoretical free precession period of 15.2 days. This motion can better be seen in a polar plot, such as Fig. 2.3.

Fig. 2.3 depicts the positions of the spin poles observed during all close fly-bys of Hyperion, in addition to the trace of the pole position from the simulation
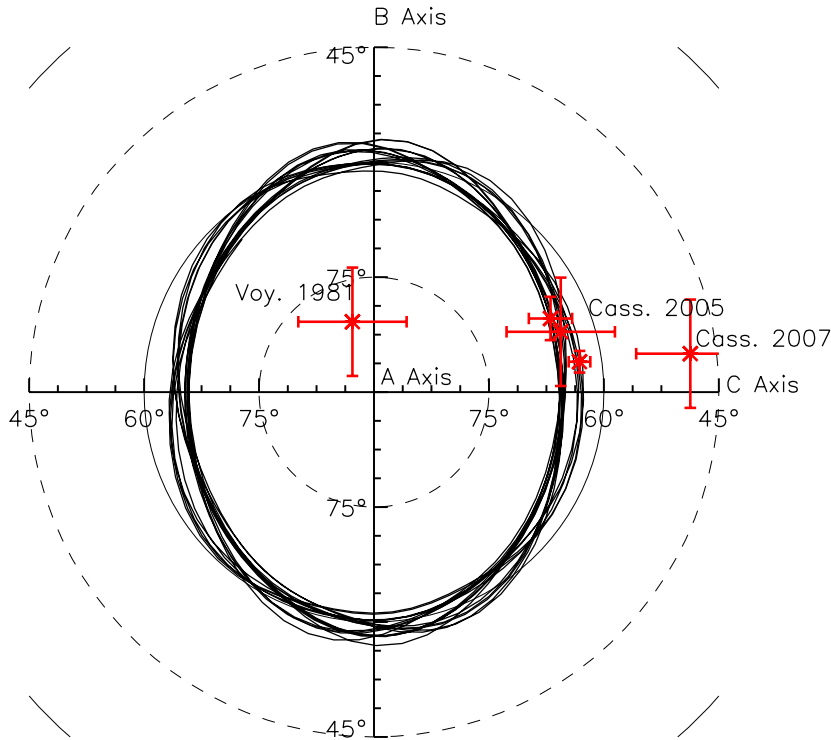
Figure 2.3: A projection of the spin axis into a body-centric coordinate frame, with a pole at the shape-defined A (long) axis of the body, and the *x* axis set by the shape-defined C (short) axis. Observations are marked with stars, while the projected 100-day path of the spin pole within the body, as plotted in Fig. 2.2, is marked with a black line – the period is roughly 16 days.

shown in Fig. 2.2. Note that the free precession is about the A axis, as one would expect for an ellipsoid that is nearly a prolate spheroid. The torques from Saturn do not change the general behavior on this timescale. Also note how far the 2007 point is from the no-torque-equilibrium point of either A-axis or C-axis rotation, confirming that Hyperion is in a state of non-principal axis rotation.

Fig. 2.4 unfolds the simulation trajectory plotted in Fig. 2.3 and plots it and the spin rate with respect to time. Though the error is large in the latitude of the spin axis, the measured latitudes are consistent with the model. However, this plot shows vividly the 180° discrepancy in the longitude of the September 2005
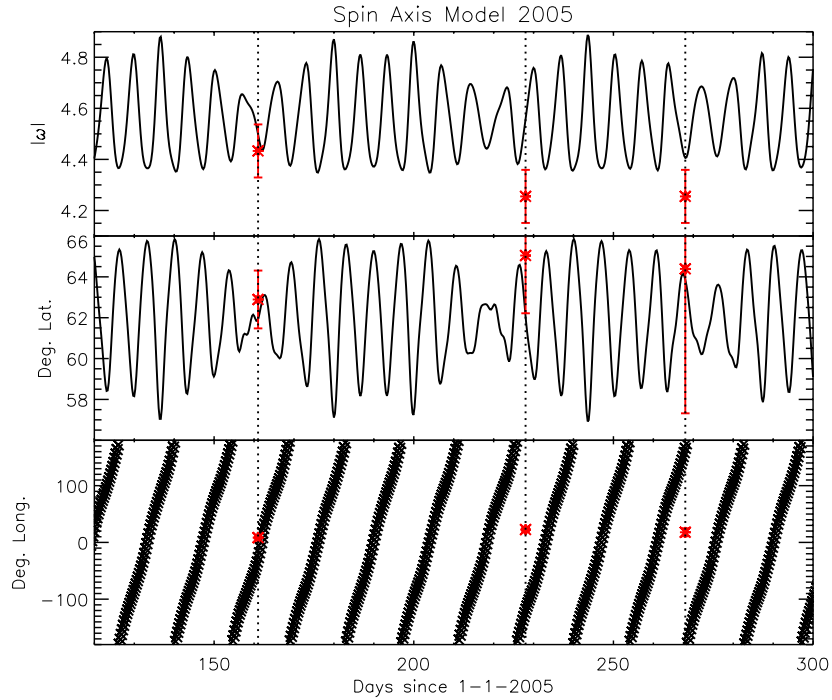
Figure 2.4: Fig. 2.3 unfolded in time, and plotted in units of body-centric latitude and longitude (with the A axis as the pole and the A-C meridian marking 0 degrees longitude) and spin rate. Note that the observations (stars) show that the latitude is consistent with the shape-derived model (line), but not the longitude.

point, and~ 120° in August of 2005. This suggests that the assumption that Hyperion is a uniform-density body whose mass distribution can be derived from the shape model should be examined further, to see if an acceptable solution can be found within the errors of the observations and shape model.

2.4 Varying the Initial Conditions and Moment Ratios

The rotational pole of Hyperion was observed to move less than 10° with respect to the surface between the three 2005 flybys (Fig. 2.3). But the spin axis should be freely precessing around the A axis as it rotates, as shown in the model. Two

explanations for this make dynamical sense: either the spin axis is closer to the true A axis, making the amplitude of precession less than observational error, or that the three observations happen to be separated by roughly integer multiples of the precessional period. The precessional period is affected by the moments of inertia, the rotation rate, and the offset between the spin axis and axis of precession, while the position of the spin axis relative to the principal axis will affect the amplitude of precession.

In this section, we explore the parameter space, varying the spin axis, spin rate and moment of inertia ratios, to see which solutions consistent with the estimated error bars might bring the spin axis back to the same position at each close fly-by of Cassini. We assume fixed locations of the principal axes based on the Thomas et al. (2007) shape model with a homogenous interior.

Two sets of model integrations were done, one in which only the spin axis was allowed to vary within the estimated errors in the data, and one in which only the moments of inertia were allowed to vary. To quickly sample a multi-dimensional parameter space, a random value was chosen for each parameter, using a Gaussian distribution with the nominal value as the mean and the estimated observational or modeling error as the standard deviation. The set of 100 results for the variation in the moments of inertia (or more properly, their ratios, A/C and B/C) can be seen in Fig. 2.5, and the 100 results for the variations in position and magnitude of the June 2005 spin vector can be seen in Fig. 2.6.

The nominal model rotates primarily about the A-axis. This is unusual for a rotating body in general, as it is a higher-energy state compared to rotation about the C-axis, and should not persist for long periods. However, this was also the state observed by Voyager 2.2. Varying the moments of inertia (Fig. 2.5)
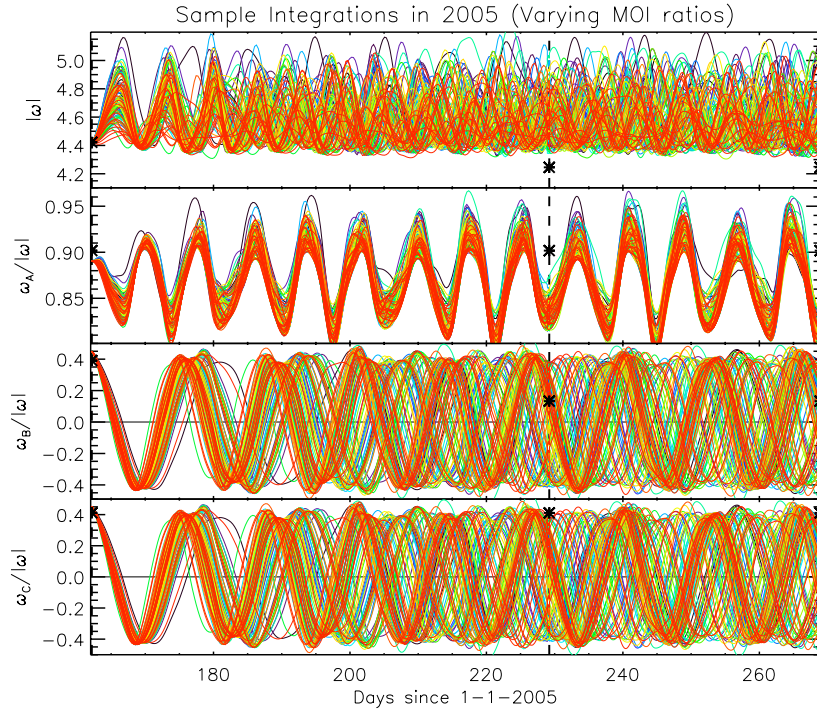
Figure 2.5: Model of the position of the spin axis and magnitude of Hype-
rion's spin in body-centric coordinates, starting from the June
2005 point and progressing forward in time for 107 days. All
three Cassini observations are marked as asterisks on the plot.
The moments of inertia were given random Gaussian errors of
σ=0.027 for A/C and B/C, while the initial spin state was held
as observed. The principal effect of changing the moments of
inertia seems to be a variation in the precessional period (as
seen in the phase shift in the rotation about the B and C axes),
with some variation in the amplitude of the periodic oscilla-
tions. 100 trajectories are plotted.

does not seem to change this rotational state. However, it does have the desired

effect on the precessional period, changing it to produce possible returns to the

June location of the spin pole during the other fly-bys. Changing the initial

spin state within observational errors (Fig. 2.6) produces an effect of similar

magnitude. The primary effect here is of moving the spin axis towards or away

from the axis of precession, with a corresponding change in the amplitude of

precession about the A axis and the wobble towards and away from the A axis.
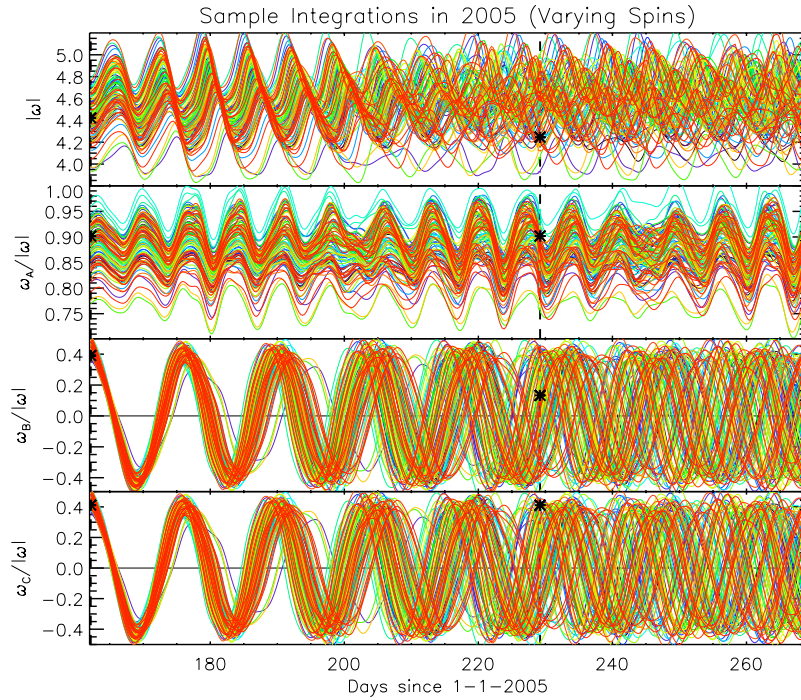
Figure 2.6: Model of the position of the spin axis and magnitude of Hyperion's spin in body-centric coordinates, starting from the June 2005 point and progressing forward in time for approximately 107 days. All three Cassini observations are marked as asterisks on the plot. The spin magnitude was given a random Gaussian error of $\sigma = 0.047n$ (1° per day). The error in spin direction was given a random Gaussian error of $\sigma=2°$. The moments of inertia were held constant at the ones derived from the shape model. 100 trajectories are plotted.

Although all three measurements of ω_A, ω_B and ω_C appear to be within the ranges of our solutions, two or three-dimensional cuts through parameter space such as these do not tell the whole story. While Figs. 2.5 and 2.6 shows that the individual components of the spin vector in August and September can be reached within their uncertainties from the June measurement, it does not answer the question of whether the full six-dimensional spin states are recovered. We will address better methods to examine this issue in the next section.

2.5 Limits on the Moments of Inertia

As the model demonstrates, Hyperion's spin axis has two motions within the body on 100-day timescales – a small 'wobble' in the spin axis towards and away from the A axis, and a precession of the spin axis around the A axis, with the precession being the larger motion. Black et al. (1995) give an exact expression for the spin axis's free precessional period in their Eq. 8, but, given the near-equality of B and C, the assumption of a prolate spheroid should produce a reasonable approximation. The precessional period of the spin axis within the body, given $\omega_{rot} = \frac{2\pi}{P_{rot}}$, for a prolate spheroid is (Fowles and Cassiday, 1999):

$$P_p = \frac{\bar{C}}{\bar{C} - A} \frac{P_{rot}}{\cos \delta} \tag{2.19}$$

where $\delta \approx 30°$ is the angle between the spin axis and the A axis, and $\bar{C}$ is the geometric mean of the B and C moments. Note that this is distinct from the forced precession of Hyperon's spin axis in inertial space due to the mean torque from Saturn, whose period is on the order of 200-300 days (Black et al., 1995).

If we re-write this equation in terms of the moment of inertia ratios, rather than their individual values, we get

$$P_p = \frac{\sqrt{B/C}}{\sqrt{B/C} - A/C} \frac{P_{rot}}{\cos \delta} \tag{2.20}$$

or

$$B/C = \frac{(A/C)^2}{\left(1 - \frac{P_{rot}}{P_p \cos \delta}\right)^2}. \tag{2.21}$$

35

From this expression, and assuming that $\delta \approx 28°$ (from Fig. 2.4) and an average rotational frequency of $4.5n$, the expected precessional period for the nominal moments of inertia derived from the shape model is 15.1 days. This compares well to the precession seen in the model, and agrees almost exactly with Black et al. (1995)'s more precise calculation. Given a tweaked precessional period – say, one for which small integer multiples were equal to the intervals between successive fly-bys of 40 and 67 days – one could work backward to determine a function of B/C versus A/C that would produce that period. Should such a solution exist, this would neatly solve the matter of whether Hyperion's spin axis could have been observed at the same position during all three 2005 fly-bys.

In reality, of course, this is a simplification. Hyperion's triaxial shape means that the above calculation is but an approximation to reality, and there are other factors not considered here – Hyperion's instantaneous spin rate is changing and the pole is wobbling within the body. But this gives a conceptual idea of what dominates the fitting process.

In order to do a more detailed analysis, we divided the A/C and B/C parameter space into a 30 by 30 grid centered on the shape-model's estimate and scaled so the search space was six σ by six σ (or 0.18 by 0.18), and integrated each curve from the June 2005 observation forward to August 2005 and September 2005. The resulting spin state were then compared to the observations by the function

$$\chi^2 = \sum \frac{\left|\vec{\omega} - \vec{\omega_0}\right|^2}{3\left|\omega\right|^2 \sigma_\omega^2} + \frac{3 - \left(\vec{A} \cdot \vec{A_0}^2 + \vec{B} \cdot \vec{B_0}^2 + \vec{C} \cdot \vec{C_0}^2\right)}{3\sigma_\theta^2}. \tag{2.22}$$

where $\vec{A}$, $\vec{B}$ and $\vec{C}$ are the principal axis vectors as predicted from the model, $\vec{\omega}$ is the vector composed of ω_A, ω_B, and ω_C, predicted from the model, and $\vec{\omega_0}$, $\vec{A_0}$, $\vec{B_0}$ and $\vec{C_0}$ are those observed. σ_ω and σ_θ represent the angular errors in the spin axis and body orientation, respectively. The χ^2 is summed over all observations excluding the initial conditions of the integration. In this case, that means summing the August and September 2005 observations, but not those from June 2005.

From Equation 2.21, we would expect that curves of constant precessional period will be parabolas in A/C versus B/C space. Given the modest uncertainties in the measurements, the parabolas of equal precessional period should be picked out strongly in A/C versus B/C space, with those that produce near-integer periods of precession between the pairs of observation producing low χ^2 valleys, and those that have half-integer periods between one or both pairs producing high χ^2 peaks.

The results, smoothed by a median filter and plotted as a contour plot of A/C versus B/C can be seen in Fig. 2.7. There is a local minimum near the shape-derived values of the moments of inertia with a reduced χ^2 (with 10 degrees of freedom) of 80. As mentioned above, the precessional period at the local minimum near the shape-derived moments of inertia has a period of approximately 15.1 days. Remembering that the later two fly-bys in 2005 were 67 and 107 days from the first fly-by, this yields intervals of 4.4 and 7.0 periods between flybys.

There is a similarly-deep minimum at A/C $\approx$ 0.61; B/C $\approx$ 0.80, as well as other noteworthy minima in the lower-right quadrant of the figure. The local minimum at A/C= 0.61, B/C=0.80 gives a precessional period of 18.0 days, giving intervals of 3.7 and 5.9 periods between the first and subsequent flybys.
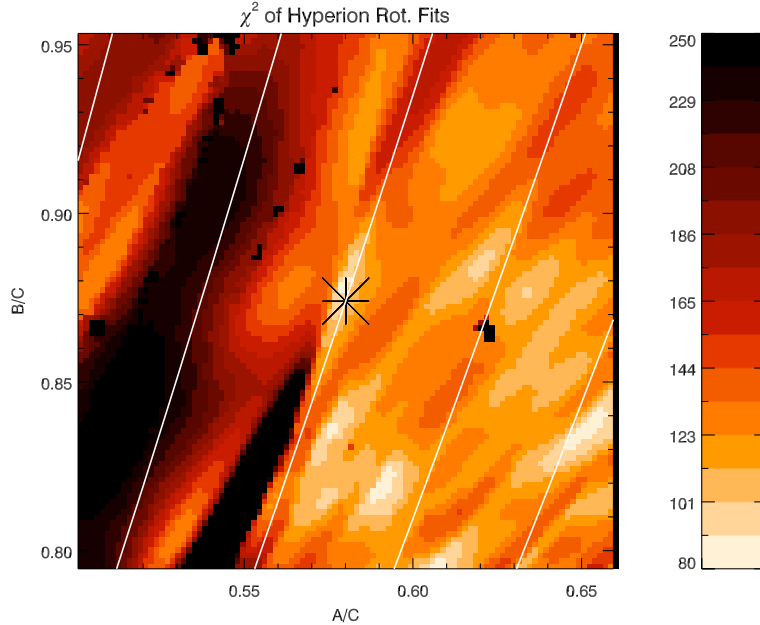
Figure 2.7: The χ^2 of the observed rotation states in August and September 2005 given the rotation state in June 2005 as a function of A/C and B/C. Lighter color indicates lower values of χ^2, and the star in the center of the diagram marks moments derived from the shape model. For reference, the plot is 6 times larger than the estimated errors in A/C and B/C. The model was smoothed with a median filter to eliminate spurious results. Parabolas are lines of theoretical constant precessional period, plotted at semi-regular intervals.

As expected from Eq. 2.21, areas of good and bad fits follow curved shapes, though not quite the predicted parabolas (plotted in white in Fig. 2.7). Both solutions mentioned above yield a near integer-number of precessional periods between June and September, but a non-integer between June and August. Integrating the position of the spin axis at these minima confirms that there are a whole number of cycles of precession between the first and last fly-bys.

The more detailed integration does correspond with our naive expectation that the best-fit models would be ones where precession returns the spin axis to the same position during each fly-by. However, the parameter search did not

produce a solution that would return the location of the August 2005 spin axis relative to the surface to its June location. Our integrations held the June 2005 spin vector fixed as the initial conditions; allowing this to vary might produce better fits, but the exponential growth in the spin axis uncertainty due to chaos rapidly overwhelms any plausible initial error. On the other hand, we must consider the possibility that merely adjusting the moments of inertia is not enough to produce a good fit to the data.

2.6   Variations in Orientation of the Principal Axes

Our nominal model assumes a homogenous Hyperion to calculate the moments of inertia, which are then used in the rotation model to evolve the spin states between flybys. While the models in Fig. 2.7 relax the assumption of homogeneity, we have still assumed that the principal axes lie along the long and short symmetry axes of the shape model. However, that need not be the case.

Hyperion is known to have a large degree of voidspace (Thomas et al., 2007), which indicates that it is a mix of solid material, most likely an ice mixture at densities around 1000 kg m^{-3}, and empty space. While a simple inhomogenous density model (for example, a density increase towards the center) might result in a change in the moment ratios without a change in the principal axes from a homogenous model, an asymmetric distribution of voidspace would produce changes in both.

In order to simulate an offset from the shape model axes, a second set of Euler angles was specified and then the long and short shape-model axes and the spin axes were rotated through these angles. This represents a shift in the true

principal axes from the ones derived from the shape model. These angles were selected to be within 45 degrees of the (0,0,0) triplet of angles that specified that the shape axes were identical to the principal axes. The differential equations were then integrated starting from the June 2005 body orientation and instantaneous spin state, and the transformation was then done in reverse to compare the final spin state and body orientation to the right ascension and declination observations of the shape and spin axes.

While the Euler angles cannot be visualized as a physical location of the principal axes in space without a conversion, as offsets in right ascension and declination might be, they are easier to sample in a uniform manner. This gives a 3-dimensional phase space within which to search for the best fit to the data. For ease of display, the minimum of each 2D sub-space is plotted in Figs. 2.8, 2.9 and 2.10, with the χ^2 calculated as specified in Equation 2.22.

As Figs. 2.8, 2.9 and 2.10 show, there is a large minimum in phase space that is located some tens of degrees from the principal axes derived from the shape model, near $\theta' = 40°$, $\phi' = 20°$, $\psi' = 10°$. This is deeper than the minima seen in Fig. 2.7, with a reduced χ^2 of 57, significantly less than the ~ 80 when only the moment of inertia ratios were adjusted.

Using the position of the principal axes after the rotation from the shape axes, we can reproject Figs. 2.8, 2.9 and 2.10 to a more physically-meaningful coordinate system. This was done in Fig. 2.11, which plots the location of the A axis (i.e., the minimum moment of inertia) in terms of the body-centric coordinate system used previously in Fig. 2.3, where the pole of the plot is the shape-derived A axis, and 0° longitude is the location of the shape-derived C axis. Here the location of the deep minimum, indicating the best fit of the actual
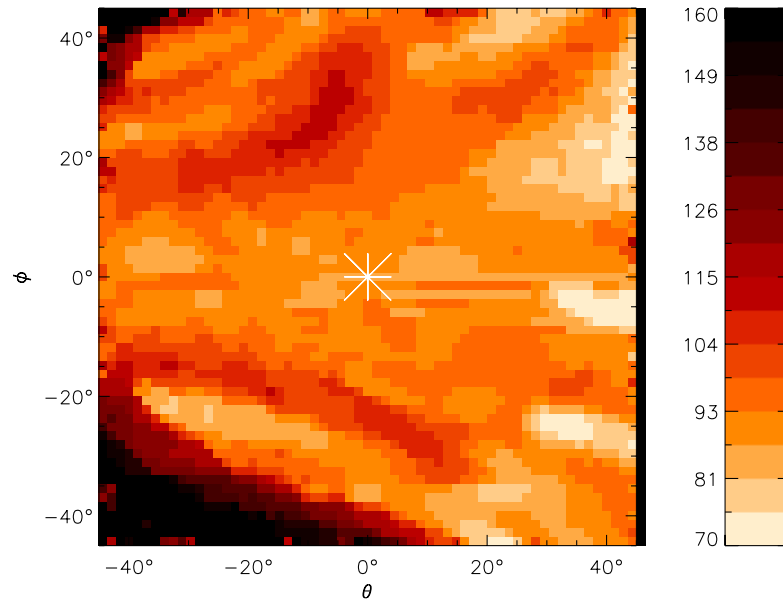
Figure 2.8: The χ^2 of the observed rotation states in August and September 2005 given the rotation state in June 2005 as a function of the Euler principal-axis-offset angles θ and ϕ, and minimized along ψ. The star in the center of the diagram marks the principal axis locations derived from the shape model, and lighter shading indicates a lower reduced χ^2. The model was smoothed with a median filter to eliminate spurious results, which raised the plotted χ^2 in local minima.

A axis, seems to be very near the location of the spin pole observed in 2005, some 30° from the shape-derived a axis. This is what one would expect in order to minimize in-body precession without relying on specific moment ratios to make the intervals between flybys match the precessional period.

2.7 Conclusions

At the time of the Cassini fly-bys in 2005, Hyperion was found in a state of non-principal axis rotation, with the spin axis nearly coincident with the long
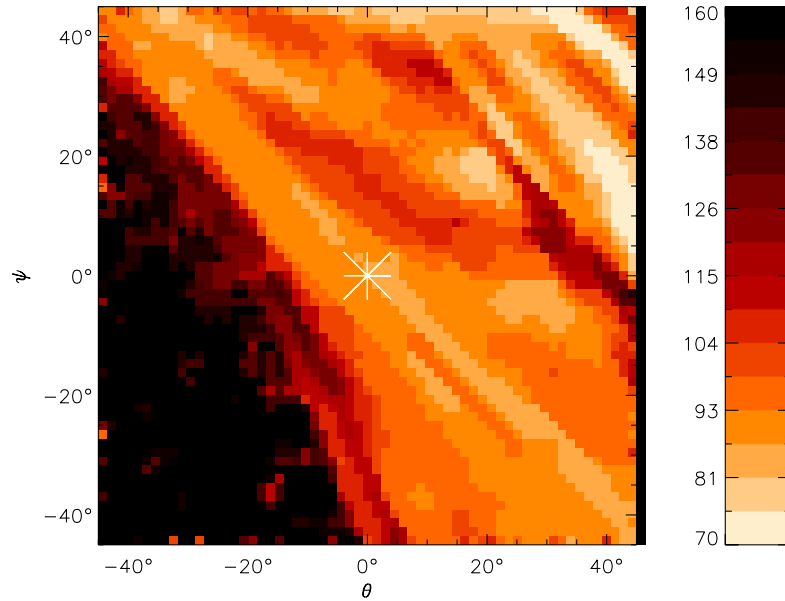
Figure 2.9: The χ^2 of the observed rotation states in August and September 2005 given the rotation state in June 2005 as a function of the Euler principal-axis-offset angles θ and ψ, and minimized along ϕ. The star in the center of the diagram marks the principal axis locations derived from the shape model, and lighter shading indicates a lower reduced χ^2. The model was smoothed with a median filter to eliminate spurious results, which raised the plotted χ^2 in local minima.

shape axis and a spin period 4.2 to 4.5 times synchronous, similar to what was observed during the Voyager flyby, and again by Cassini in 2007. Modeling suggests that this state is in fact more stable than a near-synchronous rotational state (Black et al., 1995). In-body precession of the spin axis should be observed, but it is not.

It is possible to adjust the moments of inertia such that the precessional period becomes the correct value to return the spin axis to the same position within the body for two of the flybys, but not all three. However, Hyperion's large fraction of voidspace (revealed by its low bulk density) suggests a possible alternate
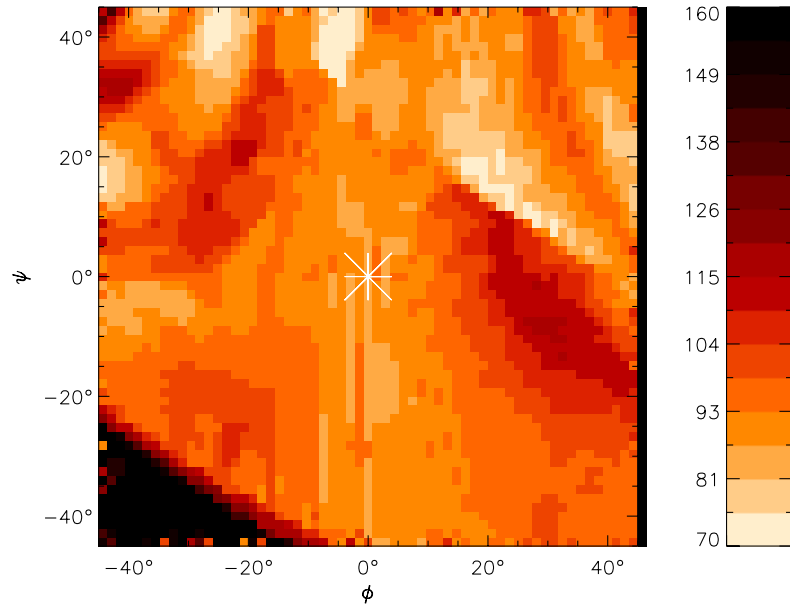
Figure 2.10: The χ^2 of the observed rotation states in August and September 2005 given the rotation state in June 2005 as a function of the Euler principal-axis-offset angles ψ and ϕ, and minimized along θ. The star in the center of the diagram marks the principal axis locations derived from the shape model, and lighter shading indicates a lower reduced χ^2. The model was smoothed with a median filter to eliminate spurious results, which raised the plotted χ^2 in local minima.

explanation: that the satellite's shape may not necessarily reflect the interior mass distribution, and, thus, correctly predict the principal axes of inertia. We have shown by trying alternate principal axes and moment-of-inertia ratios that a better fit is available after the principal axes are rotated ~30° with respect to the shape model's axes, such that the A axis was, in fact, close to the spin axis position in 2005.

Thus, we conclude that it is unlikely that the assumption of homogeneity is valid for Hyperion and, furthermore, that the long and short axes of the shape model are not accurate guides to the principal axes of inertia. A five-
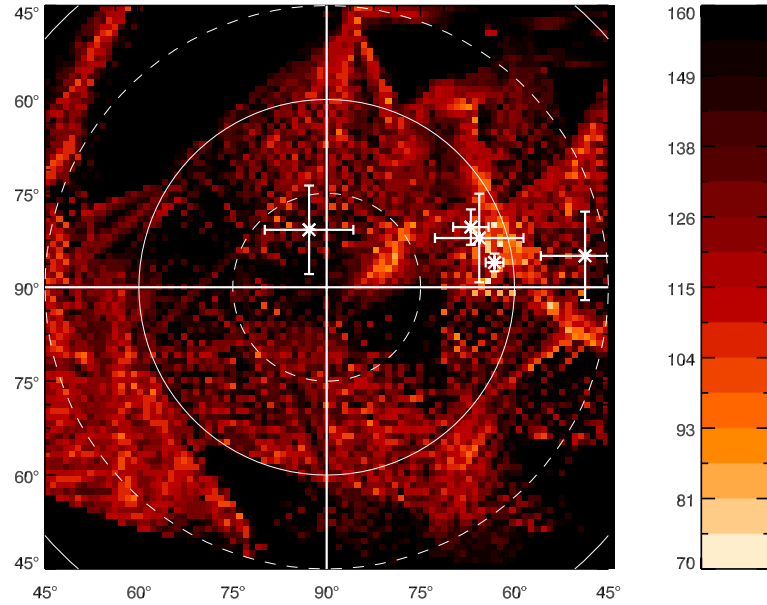
Figure 2.11: The data from Figs. 2.8 to 2.10, reprojected to show the location of the A axis, relative to the shape-derived a axis (90° latitude) and c axis (0° latitude, 0° longitude). The stars with error bars marks the location of the spin axes, seen in 1981 (leftmost), 2005 (center cluster) and 2007 (right). Note the deep minima from Figs. 2.8 through 2.10 place the preferred location of the A axis almost directly beneath the location of the spin pole in 2005.

dimensional combinational model – one in with both the axis positions and moment-of-inertia ratios are varied – could probably return a better fit (as measured by reduced χ^2) than either the two-dimensional or three-dimensional models shown in Figs. 2.7 through 2.11. Given that our best three-dimensional model has a reduced χ^2 of 57, rather than the near-unity expected for an excellent fit, there is room for improvement. However, such a model may not be justifiable by the limited amount of available data (essentially the orientation and spin states at only three epochs), and Hyperion's short Lyapunov time.

44

CHAPTER 3

THE SMALLEST PARTICLES IN SATURN'S A AND C RINGS.

HARBISON, R. A., NICHOLSON, P. D. & HEDMAN, M. M. *ICARUS*,

VOLUME 226, ISSUE 2, 2013.

3.1 Introduction

The vast majority of particles that make up Saturn's main rings cannot be seen individually, but as an aggregate they become one of the most striking objects in the Solar System. From past observations, we know that the ring particles come in various sizes.

The Voyager radio science experiment used radio occultations at 3.6 and 13 cm to probe the ring particles by two methods. Direct inversion of the radio signal forward-scattered by meter-sized particles produced a size distribution showing a sharp drop-off above a radius of ~5 m, while the differential optical depth measured between the two bands used in the occultation allowed a power-law to be fit between particle radii of 1 m and 1 cm (Marouf et al., 1983; Zebker et al., 1985). However, the Voyager radio science experiment was insensitive to particles smaller than 1 cm; smaller ring particles do not absorb even the shorter 3.6-cm radio waves from Voyager.

French and Nicholson (2000) used the 28 Sagittarii (28 Sgr) stellar occultation, as observed from Earth in July, 1989 at wavelengths between 1 and 4 μm, to look for light forward-scattered by ring particles. Unlike the monochromatic radio-science experiments, they could not separate forward-scattered light from light directly transmitted through the rings. However, the differing range and

acceptance angle between this and the Voyager PPS stellar occultation allowed a gross measurement of forward-scattering. This measurement could then be modeled with a truncated power-law. The 28 Sgr occultation, like Voyager, had limited sensitivity to particles under 1 centimeter, but for a different reason: the scattering angles of such small material was larger than the photometric aperture size, so could not be measured.

Previous radio occultation and stellar occultation experiments were thus most sensitive to particles in the centimeter to meter range. This situation changed with the arrival of the Cassini spacecraft at Saturn in 2004. As Saturn was near its northern winter solstice in 2004, the rings were more open than when Voyager observed them, reducing the effective optical depth as seen from Earth and increasing the signal-to-noise for occultations by dense rings. In addition to the 3.6 and 13 cm radio bands, Cassini can also transmit at 1.3 cm. Not only does a shorter wavelength probe smaller particle sizes, but three measurements of the optical depth at different wavelengths allow for more exact models to constrain both the effective minimum particle size and effective power-law index. The C ring minimum particle size was estimated at 4 mm, while the data for the A ring suggest a larger minimum particle size (Marouf et al., 2008). A fuller discussion of these results can be found in Cuzzi et al. (2009).

While some micrometer-sized particles have been seen within the main rings, they are either found in transient spoke features (D'Aversa et al., 2010; Mitchell et al., 2013), probably dislodged from the surfaces of larger ring particles (Mitchell et al., 2006), or are confined to narrow, diffuse regions of the rings such as the Encke Gap ringlets (Hedman et al., 2007b) and the 'Charming Ringlet' in the Laplace Gap (Hedman et al., 2010a). Differential optical depth,

phase-function, and microwave emissivity measurements all show that very little dust persists within the main rings on a large scale in both space and time (Dones et al., 1993; French and Nicholson, 2000; Spilker et al., 2005). Theoretical work by Bodrova et al. (2012) also has shown that, under unperturbed main ring conditions, particles smaller than a few centimeters will adhere onto larger ring particles.

When Cassini entered Saturn orbit in 2004, its wide range of orbital geometries not only allowed for multiple radio and (space-based) stellar occultations, but also permitted the first solar occultations by the rings to be observed. The Visual and Infrared Mapping Spectrometer (VIMS) onboard Cassini can accept light through a special solar port, which has the attenuation needed to safely observe the Sun with the VIMS detector array. Given the 0.5 milliradian pixel size of VIMS and its near infrared (0.9 to 5.2 microns) spectral range, the VIMS data are most sensitive to the previously-unsampled size regime of 100 microns to a few millimeters.

In this work, we will use the VIMS solar occultations to examine this neglected regime, with the goal of setting an effective minimum radius on the ring particle size distribution in different regions. Following a description of the VIMS solar port and the data taken during solar occultations, we will present our method for reducing the solar port data and separating the component of light scattered at small angles from the direct solar image. Once this component is separated, it can be compared to a model of particle diffraction to estimate an effective minimum particle size for the C ring. This model is then refined to account for the self-gravity wakes and higher optical depths observed within the A ring – which violate several simplifying assumptions made at first – and

47

applied to that ring.

3.2 Data

3.2.1 Basic Processing

As of February 2010, Cassini had observed eleven solar occultations of the rings:
see Tables 3.1 and 3.2 for a list. The procedure for observing solar occultations
involves taking a series of 12 pixel by 12 pixel (6 x 6 milliradians) multispec-
tral images of the area of the sky around the Sun using the VIMS solar port,
which has an attenuation on the order of 10^5. The instrument's visible channel
is turned off, as the visible-light spectra, even through the solar port, saturate
within a few milliradians of the Sun. Thus, data obtained through the solar
port have a wavelength coverage of 0.9 to 5.2 μm. A single VIMS 'cube' of two
spatial and one spectral dimensions is constructed pixel by pixel, using a 2D
scanning mirror. Each pixel has an exposure time of 40 ms, and approximately
5 cubes of 144 pixels each are obtained for every minute of the occultation. Each
occultation data set is thus a time series of cubes – one temporal dimension, two
spatial, and one spectral. For full details of the VIMS instrument, see Brown
et al. (2004).

The onboard VIMS signal processing electronics perform automatic back-
ground subtraction. At the end of each line of 12 pixels, VIMS takes a spectrum
of the thermal background signal by closing off the spectrometer from outside
light and taking a measurement. Four measurements of this dark spectrum are
averaged together, then subtracted from the last four lines of pixels taken. As

a result, each cube has a slightly uneven background subtraction, as there is some shot-noise variance even after averaging over four measurements. In most cases, these three background spectra are within a data number (DN) or two of one another[1], but a cosmic ray can hit the detector during a background measurement, producing an artificially high background in one or more spectral channels.

In order to correct this, the background was re-added to the signal, returning the data to its raw form, and then the median of the three dark current spectra recorded for each cube was used as the background instead. The slight temperature change when Cassini moves into the rings' shadow lowers the dark current by approximately 2 DN. Hence the dark background subtracted is slightly dependent on the position of Cassini, so further time-averaging of the background was not done.

The cubes showing the unocculted Sun were used as a reference to define transmission of the rings, and all measurements are reported either in units of transmission or in 'raw' data numbers (DN), rather than absolute flux. The position of the Sun within the image varied by well under a single pixel in each occultation, making any variable response due to a slightly different beam path within the solar port or the spectrometer minimal.

---

[1]Raw VIMS spectra represent photo-electron counts, but are returned in scaled integer form as Data Numbers. The instrumental gain was set such that the detector read noise is ≈ 1 DN, or ~ 300 electrons.

3.2.2 Instrumental Effects

The VIMS solar port is designed to attenuate the Sun enough to make it safe to observe with the VIMS instrument. However, the optics that do this also produce abundant stray light within the instrument. As a result, in addition to the normal solar image that can be fit to a two-dimensional Gaussian point-spread function (PSF), there is also a diffuse component that extends at least 6 solar diameters from the Sun (Figure 3.1). To first order, this diffuse component is flat over the 12 by 12 pixel images. At approximately 1/10th of the peak of the solar signal, the diffuse signal is ∼ 10 times larger than the flux within the nominal solar image when integrated over the entire cube (Figure 3.2). In addition, the diffuse component is spectrally different from the direct component, being distinctly 'redder'. This greatly complicates any attempt to look for scattered light from millimeter-sized ring particles, but a method to exploit the stray light will be discussed in Section 3.5.2.
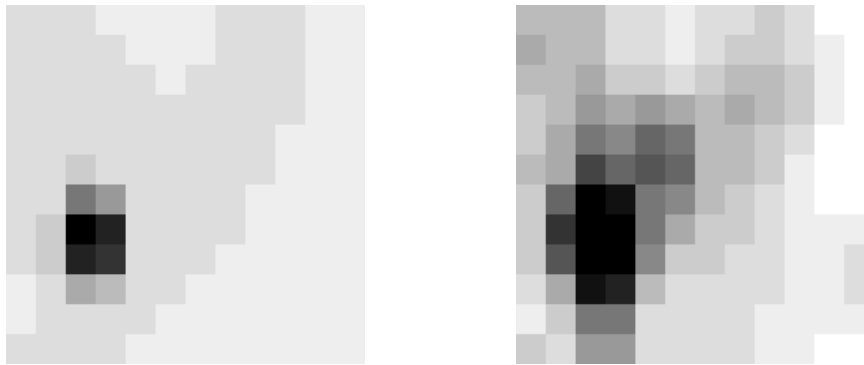
Figure 3.1: Contrast-reversed images of the Sun at 2.40μm though the VIMS solar port – both unstretched (left) and stretched (right) by displaying the square root of the DN value of each pixel. The greyscale is such that 0 DN is 'white', and the peak solar signal is 'black'. To first order, the diffuse background is flat, but when stretched, the nonuniform features become clear.
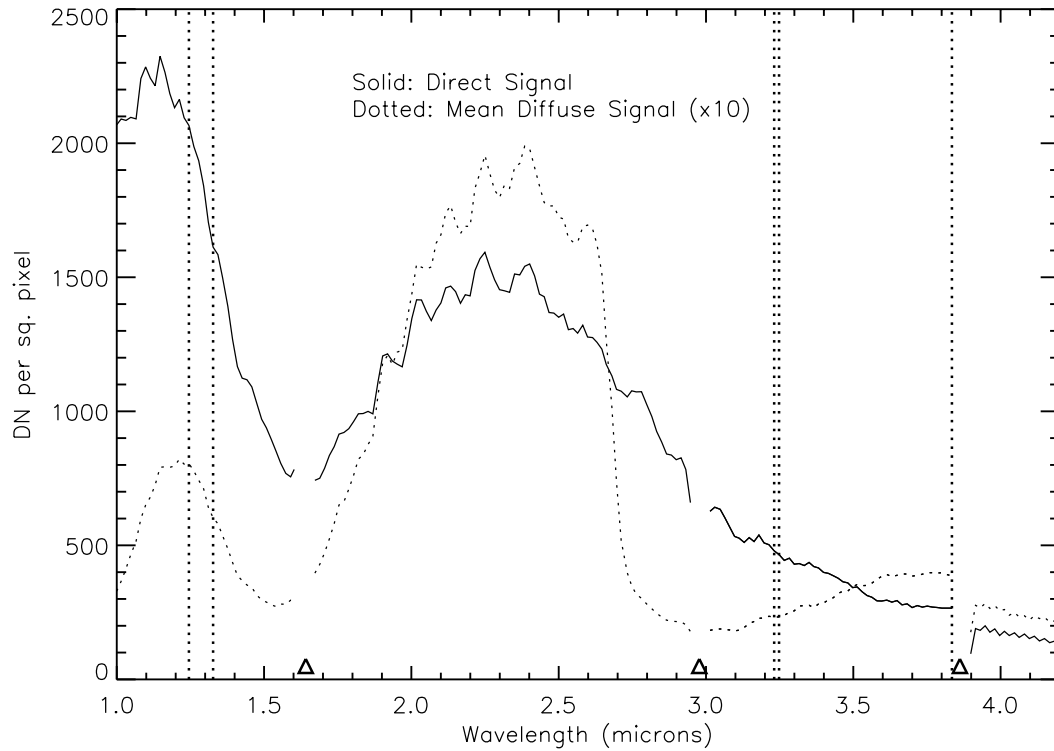
Figure 3.2: Plot of the peak direct recorded signal (solid) and mean diffuse signal (dotted, magnified by 10 times) per pixel in the images taken of the Sun outside the rings on the Rev. 55 occultation. Peak values were measured by a Gaussian fit, and were recorded in units of DN per pixel. Note that the signals have different spectral shapes, and that, in a 12 by 12 VIMS cube, the total diffuse signal is about an order of magnitude larger than the direct signal. Triangles mark the locations of the edges of VIMS's order-sorting filters (which ensure only the listed wavelengths of light are measured by rejecting higher order signals from the diffraction grating), where the data become unreliable, while the vertical dotted lines mark spectral channels known for increased noise in calibration images.

3.2.3   Data Selection

Of the eleven solar occultations taken before equinox in 2009 and observed by VIMS, nine cover the A ring, and six extend into the C ring. The A ring occultations (Table 3.1) are mixed between nearly-radial occultations for which the Sun passed behind all of the rings (and then behind Saturn itself), and chord occultations for which the Sun passed behind one of the ansae, giving two 'cuts' across the outer rings. For the A ring, both the radial and chord occultations sample nearly uniformly in the radial direction as well as sampling only a limited range of longitude ($\lesssim 5°$).

The six occultations clearly covering the C Ring (Table 3.2) are also a mix of chord occultations and radial occultations. As all of the chord occultations 'turn around' in the C ring, the data here have variable radial sampling, with the inner parts of the occultation (near the turnaround point) sampled more finely than outer parts.

All data are not equal: the quality of the data is related to the opening angle of the ring. For the A ring, occultations done later in the mission are almost opaque due to the low opening angle of the rings. The C ring has the opposite problem; the large opening angles at the beginning of the mission meant that most of the sunlight is transmitted without interacting with the ring at all. Different occultations also had different number of cubes covering each area of the ring: the more cubes, the more data available.

Rev.	Date	Ring Open. Angle (°)	Ave. Long. (°)	Number of Cubes	Ave. Trans.
9	08 Jun. 2005 (R)	21.45	78	47	0.348
43	24 Apr. 2007(E)	12.77	297	70	0.270
55	03 Jan. 2008 (I)	9.00	61	37	0.201
55	03 Jan. 2008 (E)	9.00	143	37	0.041
59	20 Feb. 2008 (R)	8.27	108	18	0.109
62	23 Mar. 2008 (I)	7.79	41	15	0.099
62	23 Mar. 2008 (E)	7.79	150	17	0.025
65	20 Apr. 2008 (I)	7.36	45	16	0.099
65	20 Apr. 2008 (E)	7.36	143	18	0.019
66	30 Apr. 2008 (I)	7.21	46	16	0.098
66	30 Apr. 2008 (E)	7.21	142	18	0.023
85	17 Sept. 2008 (I)	5.05	47	7	0.044
85	17 Sept. 2008 (E)	5.05	136	8	0.011
90	24 Oct. 2008 (I)	4.49	50	7	0.037
90	24 Oct. 2008 (E)	4.49	133	7	0.008

Table 3.1: Observations of solar occultations covering the A ring. Included is the date, the opening angle of the rings relative to the Sun at the time of occultation, the average longitude (ϕ) of the observed place in the ring plane (measured relative to the sun-planet line), the number of cubes that clearly cover the A ring, and the average transmission measured. Each occultation is marked as either a nearly-radial cut across the rings (R), or as the ingress (I) or egress (E) half of a chordal cut across the ring ansa.

3.2.4   Transmission Spectra

Transmission spectra of the main rings can be produced by summing the cubes over their spatial dimensions and normalizing to the solar spectrum as measured outside of the A ring. This offers a high signal-to-noise spectrum of the ring's transmission properties in the near infrared, given the brightness of the Sun. Combining repeated measurements at slightly different locations in the ring (sampled as the occultation progressed), we can increase signal-to-noise further at the expense of spatial resolution. This gives a transmission spectrum with errors between 0.005 and 0.022 (in units of transmission).

Rev.	Date	Ring Open. Angle (°)	Number of Cubes	Ave. Trans	Min. Dist (Mm)
9	08 Jun. 2005 (R)	21.45	65	0.781	–
11	15 Jul. 2005 (R)	21.07	81	0.776	–
59	20 Feb. 2008 (R)	8.27	51	0.498	–
62	23 Mar. 2008 (C)	7.79	145	0.628	68.375
65	20 Apr. 2008 (C)	7.36	94	0.497	74.529
66	30 Apr. 2008 (C)	7.21	84	0.520	83.844

Table 3.2: Observations of solar occultations covering the C ring. Included is the date, the opening angle of the rings relative to the Sun at the time of occultation, the number of cubes that clearly cover the C ring, and the average transmission measured. Each occultation is marked as either a nearly-radial cut across the rings (R), or a chordal cut across the rings (C), in which case the minimum distance into the C ring that the chordal cut extends is listed in the last column. Note that while the Rev. 62 and 65 chordal occultations cover most of the C Ring, the Rev. 66 chordal occultation only samples the outer half.

In Figure 3.3, we plot mean transmission spectra of the three main rings and the F Ring. The spectra were constructed by fitting a gaussian curve to the image of the Sun in each wavelength, then taking the integral over that curve to find the total flux at that wavelength. Then an 'average' spectrum for each area of the ring was produced by taking the mean over each cube 'on' the rings, and normalizing to a solar spectrum obtained by taking the mean of cubes outside of the ring system.

The main rings' transmission spectra show no obvious bands, and are remarkably flat in the region of 2 to 4 microns (the region from 4 to 5 microns is not plotted due to a much lower signal-to-noise ratio). This is in marked contrast to the *reflection* spectra of the main rings, which show strong water ice bands in this region (see Nicholson et al. (2008) for a fuller discussion of the rings' reflectance spectra). This indicates that the vast majority of ring particles

are so large as to be opaque in the near infrared.

However, not all regions of Saturn's rings behave in this matter. Free ring particles in the tens of microns (or smaller) size range *do* show prominent features in transmission, as is seen in our mean F Ring spectrum (Figure 3.3), and described by Hedman et al. (2011) in transmission spectra of the F Ring taken during stellar occultations. Most visible in F Ring spectra is a strong increase in transmission at ~ 2.9 μm due to the Christensen effect: the optical properties of water ice at this wavelength minimize absorption and internal reflection. (Hedman et al., 2011; Vahidinia et al., 2011)

Other features, such as the peaks and dips near the order-sorting filters, are likely artifacts due to a lack of signal. However, the slight 'blue' slope around 1 to 1.5 microns may be a real measure of ring properties and will be discussed later in this chapter.

3.3   Transmission Spectra Analysis

Hedman et al. (2011) introduce the variable ρ to measure the ratio in optical depth in and out of the 2.9 μm feature in stellar occultations. In order to avoid contamination from reflected sunlight in addition to the transmitted starlight, they define ρ as the ratio of optical depths at 2.9 and 3.2 μm, as the rings are dark in reflection at both wavelengths. As solar occultations focus entirely on the dark sides of ring particles, the choice of a reference wavelength out of the 2.9 μm feature is less constrained. We define $\rho_{2.5}$ as

$$\rho_{2.5} = \frac{\tau_{2.9}}{\tau_{2.5}}, \tag{3.1}$$

or the ratio between the optical depth of the 2.9 micron band (defined as the integrated optical depth from 2.82 to 2.93 μm) and the optical depth at 2.5 microns (defined as the integrated optical depth from 2.45 to 2.56 μm), with optical depths found in the conventional way, from the transmission, $T = \exp \tau/\mu$. 2.5 μm was chosen as a reference wavelength based on the high signal-to-noise in this region of the solar spectrum as measured by VIMS.

Figure 3.4 plots the composite spectra of the A, C and F rings from the Rev. 9 solar occultation in terms of the optical depth normalized to the optical depth at 2.5 μm. In Figure 3.4, the 2.9 μm peak in the F Ring transmission spectrum is seen as a dip, while the A and C ring spectra continue to appear flat. The measurements of $\rho_{2.5}$ from six solar occultations (Revs. 9, 43, 55, 59, 62 and 65) are included in Table 3.3. From the table, the F ring shows a $\rho_{2.5}$ of between 0.77 and 0.86, with a mean value of 0.82 ± 0.03. The A and C rings, however, yield values consistent with unity.

If we assume the A and C rings are a mixture of F ring-like material, with a $\rho_{2.5}$ equal to the mean F ring value of 0.82, and 'large ring particles' with a $\rho_{2.5}$ of 1, we can set a limit on the amount of dusty or F-ring-like material. From the measured values of $\rho_{2.5}$, we conclude that neither the A nor the C Ring shows a significant difference from a flat spectrum. The A Ring can contain less than 5.5% (1 σ) by cross sectional area of F-ring-like material, while the C Ring can contain less than 1.4% of F-ring-like material. From this, we can infer that free-floating ice grains in the tens of microns size range, capable of producing the Christiansen effect (Hedman et al., 2011), are quite rare within the main rings,
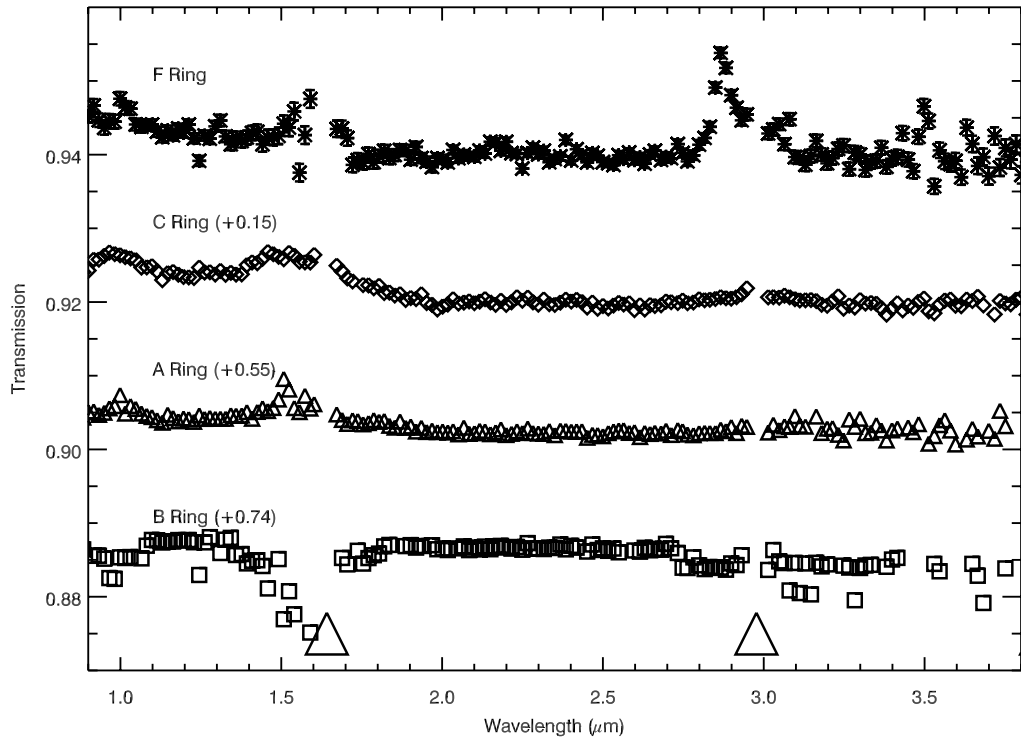
Figure 3.3: Average transmission spectra of various regions of the rings as measured during the Rev. 9 solar occultation. Large triangles at the bottom of the plot mark the locations of VIMS's order-sorting filters (features at those locations are artifacts). Statistical error bars are not plotted for the A, B and C Ring spectra, as they are smaller than the plotted symbol. The A, B and C rings are also offset for clarity by the amounts indicated.

unlike within the F Ring.
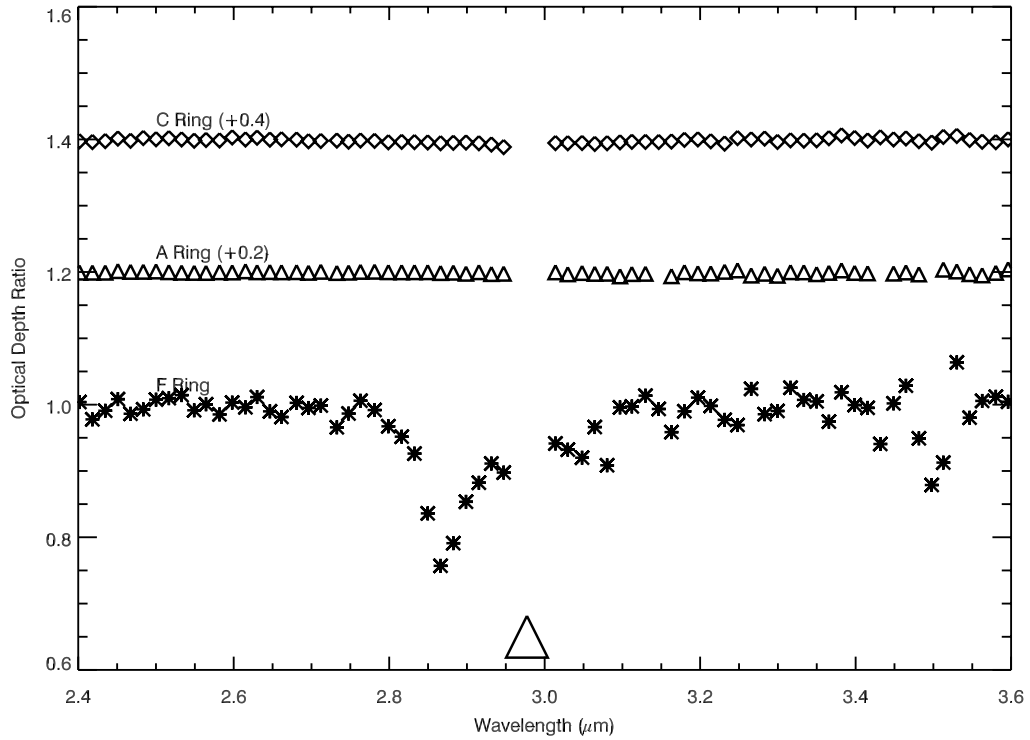
Figure 3.4: The data from Figure 3.3, replotted in units of optical depth and normalized so that τ at $2.5\,\mu$m is unity. The F Ring (stars) shows a marked decrease in optical depth at 2.9 μm due to the presence of free-floating water-ice grains tens of microns in size. The A (triangles) and C (diamonds) Rings show no such feature at 2.9 μm, limiting the number of free-floating ring particles smaller than 100 μm. The region around 2.95μm, marked by the large triangle at the plot's bottom, was not plotted due to the presence of one of VIMS's order-sorting filters, as mentioned in the caption to Figure 3.2. The A, B and C rings are also offset for clarity by the amounts indicated.

Rev.	$\rho_{2.5}$	Rev.	$\rho_{2.5}$
F Ring		**A Ring**	
9	0.852 ± 0.004	9	0.9991 ± 0.0005
43	0.858 ± 0.002	43	0.9989 ± 0.0002
55 I	0.810 ± 0.008	55 I	0.9977 ± 0.0003
55 E	0.848 ± 0.008	65 I	1.0177 ± 0.0003
59	0.809 ± 0.017	**Mean ρ_A =**	1.003 ± 0.010
62 I	0.774 ± 0.009	**C Ring**	
62 E	0.782 ± 0.017	9	0.9951 ± 0.0008
65 I	0.820 ± 0.014	59	1.0002 ± 0.0014
65 E	0.824 ± 0.008	62	0.9978 ± 0.0003
Mean ρ_F =	0.82 ± 0.03	65	1.0002 ± 0.0008
		Mean ρ_C =	0.998 ± 0.002

Table 3.3: Measure of the optical depth ratios between 2.9 μm and 2.5μm, as described by $\rho_{2.5}$. Dusty water-ice rings, such as the F Ring, show a decrease in optical depth at 2.9 μm, resulting in $\rho_{2.5} < 1$. Errors in the mean values listed for $\rho_{2.5}$ are calculated by taking the standard deviation of the set of measurements.

3.4   Diffraction Theory

3.4.1   Introduction

While, in the previous sections, we rule out a significant population of particles smaller than 100 μm in the main rings due to the lack of an observable Christiansen effect, somewhat larger particles can produce observable effects by diffraction, while being opaque. The spatial data taken by VIMS become useful to observe this diffracted signal.

To first order, sunlight diffracted by ring particles of radius a will scatter into a cone of angular radius $\theta \simeq \lambda/2a$. Given VIMS's pixel size (0.5 milliradians) (see Figure 3.5), the solar diameter at Saturn ($\approx$ 1 milliradian) and operating wavelengths (1 - 5 μm), VIMS should be able to best image diffracted light from

ring particles with a radius of several millimeters and less:

$$\theta_d \simeq \frac{\lambda}{2a} \simeq 1.0\frac{\lambda/2\mu m}{a/1mm}\text{mrad.} \tag{3.2}$$

A full model of the diffraction of sunlight by ring particles will be presented in the following section.
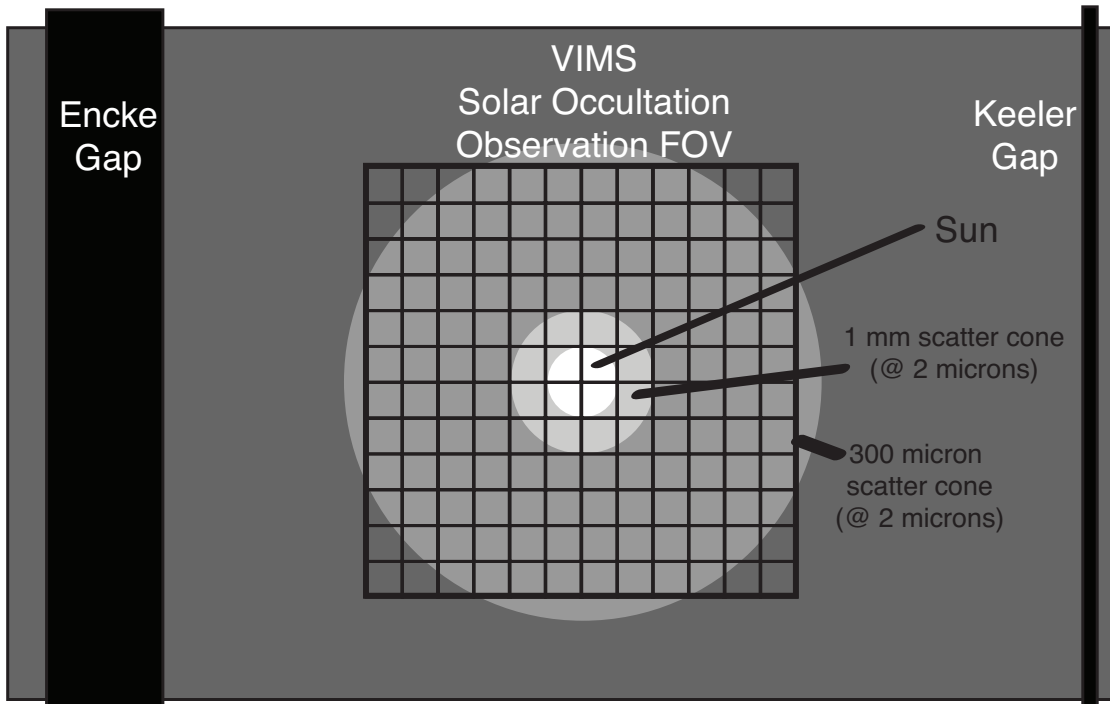
Figure 3.5: Schematic diagram showing how the Sun would appear as it passes through the outer A Ring. The diagram plots the size of a VIMS pixel, the 12 by 12 VIMS image taken during a solar occultation, and the Sun at Saturn during the 8 June 2005 solar occultation. The estimated diffraction cones of a 1mm (light gray) and 300 μm (medium gray) ring particle at 2 microns are shown around the solar disk. The Encke Gap (325 km wide) and Keeler Gap (40 km wide) at a typical Cassini-ring separation of 200,000 km are shown for scale.

3.4.2   General Expression

The model of French and Nicholson (2000) was chosen as a representation of forward scattering and absorption in a ring. French and Nicholson (2000) assume a simple truncated power-law size distribution and, for further simplicity, neglect any contribution from multiple scattering – which is a valid assumption for $\tau/2\mu \lesssim 1$. We accept this for now, but in Section 3.6.3, we extend our analysis to include multiple-scattering for higher optical depths. As higher-order scattering broadens the phase function, ignoring higher-order effects will, in general, underestimate the minimum particle size. (French and Nicholson, 2000)

This model states that the flux incident on the detector from light scattered by a uniform sheet of particles as a function of scattering angle, $F(\theta)$ is

$$ F(\theta) = F_0 \frac{\tau}{4\pi\mu} e^{-\tau/\mu} \langle \varpi_0 \rangle \overline{P}(\theta) A, \tag{3.3} $$

where F_0 is the solar flux incident on the rings, μ is the cosine of the incidence angle, $\langle \varpi_0 \rangle$ is the single scattering albedo, assumed to be 0.5 for particles much larger than the wavelength of light being studied[2], A is the solid angle of the detector (in this case, one VIMS pixel), and $\overline{P}(\theta)$ is the mean phase function of the diffracted light, normalized such that the integral over all solid angles is 4π (thus the flux from scattered light integrated over all solid angles is $F_0\tau/2\mu \exp(-\tau/\mu)$). $\overline{P}(\theta)$ depends on the distribution of particle sizes assumed.

Note that the optical depth, τ, used in Equation 3.3 and for the rest of the paper (unless otherwise noted) is the extinction optical depth, which, for particles much larger than the wavelength of light, is twice that of the *geometric* optical depth, $\tau = 2\tau_{geo}$, where τ_{geo} is typically used in optical and near-infrared studies

of the rings, including French and Nicholson (2000).

For a full derivation of the model, please see Appendix A. We chose a truncated power-law with particles between $a_{\min}$ and $a_{\max}$ in size, and with a power-law index of $-q$. To speed computational time over many orders of magnitude, we implement this in our code by two approximations valid over different angular regimes: the medium-angle case and the large-angle case, which are defined by the characteristic diffraction angle of the smallest particles in the size distribution, $\theta_2 = \lambda/2a_{\min}$. These cases are also useful in understanding the behavior of the model.

The value of θ_2 is unknown, because the minimum particle size is the quantity we are trying to measure. Given that the size of one VIMS pixel – and coincidentally the solar radius at 9 AU – is 0.5 milliradians on the sky, our data will be most sensitive to diffraction by particles with $x \lesssim 6000$, where $x = 2\pi a/\lambda$. At 2 microns wavelength, the corresponding particles have a radius of 2 millimeters or less. Barring a much-lower-than-expected minimum size cutoff, the large-angle scattering case will be most relevant, though we will include the medium-angle case in our calculations to account for the possibility of free-floating particles from ~100 microns to ~2 millimeters.

The large angle case, where the scattering angle, θ, is much larger than the characteristic diffraction angle of the smallest particles ($\theta \gg \theta_2$) has a phase function of approximately

---

[2]For our purposes, we may 'lump' all light scattered at angles $\theta \gg \theta_d$ in with the light absorbed by the particles, so that the absorption coefficient, $Q_{abs} \approx 1$. Since $Q_{ext} = Q_{abs} + Q_{sc} \approx 2$ for macroscopic particles, we have $\varpi_0 = Q_{sc}/Q_{ext} \approx 0.5$. By the same token, we exclude all reflected light from the phase function, $\bar{P}(\theta)$. For further discussion on the importance of Q, we refer the reader to Cuzzi (1985) and Roques et al. (1987).

$$\overline{P}(\theta) \approx \frac{4}{\pi\alpha}(\sin\theta)^{-3}\frac{x_{\min}^{2-q}}{q-2}, \tag{3.4}$$

where the dimensionless size parameter $x_{\min} = 2\pi a_{\min}/\lambda$ and α is a normalization factor given by

$$\alpha = \begin{cases} \ln\frac{a_{\max}}{a_{\min}} & q = 3 \\ \frac{x_{\max}^{3-q}-x_{\min}^{3-q}}{3-q} & q \neq 3 \end{cases}. \tag{3.5}$$

The medium angle case, where θ is in between the characteristic diffraction angle of the smallest and largest particles ($\theta_2 \gg \theta \gg \theta_1; \theta_1 = \lambda/2a_{\max}$), has a phase function of approximately

$$\overline{P}(\theta) \approx \frac{4}{\alpha}(\sin\theta)^{q-5}\,\mathcal{J}_0^\infty(q), \;\; \theta_1 \leq \theta \leq \theta_2. \tag{3.6}$$

The $\mathcal{J}_0^\infty(q)$ in Equation 3.6 is shorthand for $\int_0^\infty z^{2-q}J_1(z)^2\,dz$, where $J_1(z)$ is a Bessel function of the first kind. $\mathcal{J}_0^\infty(q)$ is nearly constant over the range of $2 \leq q \leq 5$, except when q approaches 2 or 5. Previous studies indicate that q is between 2.7 and 3.1 within the main rings, giving $J_0^\infty \approx 0.5$ (Zebker et al. 1985, French and Nicholson 2000, Cuzzi et al. 2009).

At this point, we remind the reader that most of the light diffracted by the centimeter to meter-sized particles which dominate the main rings at near-infrared wavelengths is *not* detectable, since it is confined to angles much less than the solar radius. Our only hope is to detect the 'tail' of the scattering function, due primarily to millimeter and smaller sized particles, if they exist in sufficient numbers.

Finally, we note that for the large-angle case, the *slope* of $\bar{P}(\theta)$ is independent of q, but the absolute level depends on q and $x_{\min}$ (or $a_{\min}$), while for the medium-angle case, the slope of $\bar{P}(\theta)$ depends on q, but the absolute level depends only weakly on q (via $\mathcal{J}_0^\infty$) or $x_{\min}$ (via α).

3.5 Spatial Data Analysis

3.5.1 Simple Attempts

Our goal is to detect and measure a faint 'halo' of diffracted light around the image of the occulted sun, in the presence of a much brighter background of instrument-scattered light, and fit this by the method described in the previous section. Our first approach was to attempt to create a template from the data of the unocculted Sun as seen through the solar port to serve as our comparison for cubes containing the occulted Sun. We selected cubes outside of the F ring or inside the C ring to construct the template. As observations were structured to give such windows on either side of solar occultations, these data were available for all occultations. While the shape and spectrum of the diffuse background does vary depending on where in the field the Sun is, based on solar calibrations performed in flight, Cassini is a very stable platform for observations, and the movements of the Sun within the field during any single occultation are much smaller than a VIMS pixel. As a result, the diffuse background changes little during an occultation, other than to scale with the total solar flux transmitted by the rings.

Once we have a template, we can divide data cubes within the rings by that

template. Given the tiny levels of diffracted signal expected, data cubes from nearby radii in the rings were summed, creating composite data cubes for the average A Ring between the radii of 122,000 and 133,000 km and for the average C ring between 75,000 and 92,000 km. Due to previous results which showed that the trans-Encke region of the A ring has a different particle size distribution than the middle and inner A ring (French and Nicholson, 2000; Zebker et al., 1985), all A ring cubes outside of the Encke Gap were omitted from the average. Cubes near ring edges were also omitted. The number of cubes fitting these criteria from each occultation are listed in Tables 3.1 and 3.2 above.

Figures 3.6 (the A ring, from Rev. 43) and 3.7 (the C ring, from Rev. 65) show data from such ratio images, plotted in units of transmission (found by dividing the composite image by the templates constructed for each occultation using cubes containing an unocculted Sun). The data from the ratio cubes were sorted by distance from the center of each pixel to the center of the Sun's image, and then binned in 0.25 milliradian (0.5 pixels) increments.

Due to the non-zero instrumental background of diffusely-scattered light, transmission measurements can be recorded even far from the Sun itself, and are not themselves a sign of diffraction from ring particles. Although at first glance the transmission profiles are 'flat', closer inspection does show some evidence for diffracted light. Figure 3.7 shows a significant increase of a fraction of a percent in transmission at around 1 milliradian. If a similar peak is present in Figure 3.6, it is invisible compared to the pixel-to-pixel variation (as seen in the error bars, which mark the standard error). Also note that the innermost datapoints (seen most clearly in Figure 3.6.c and Figure 3.7.b, but present in others) show a significant *decrease* in transmission relative to the 'far-field' mean
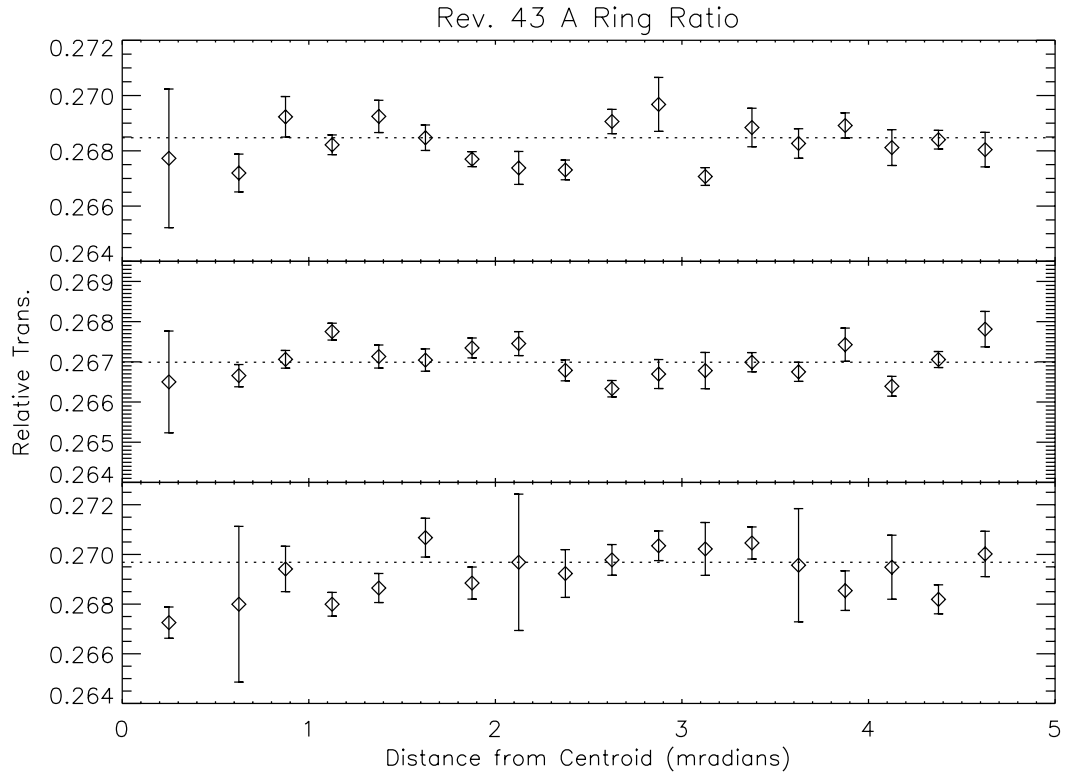
Figure 3.6: A plot of the ratio of the composite A ring image from the Rev. 43 occultation to the template created from the same occultation versus angular separation from the Sun. Data are grouped in 0.25 milliradian bins, and the error bars mark one standard error of the mean for the binned data. The dotted line is an average transmission for the area from 1 to 4 millradians from the Sun. Each panel is a different wavelength – 1.2, 2.4 and 3.6 microns from top to bottom.

transmission measured from 1 to 4 milliradians (and plotted as a horizontal line). These pixels are within the 0.5 milliradians that define the solar angular radius as seen by VIMS, indicating that the transmission as measured by looking directly at the Sun is lower than that measured from the diffusely-scattered background, which is also produced by sunlight shining through the rings.

This apparent contradiction can be reconciled by remembering that when
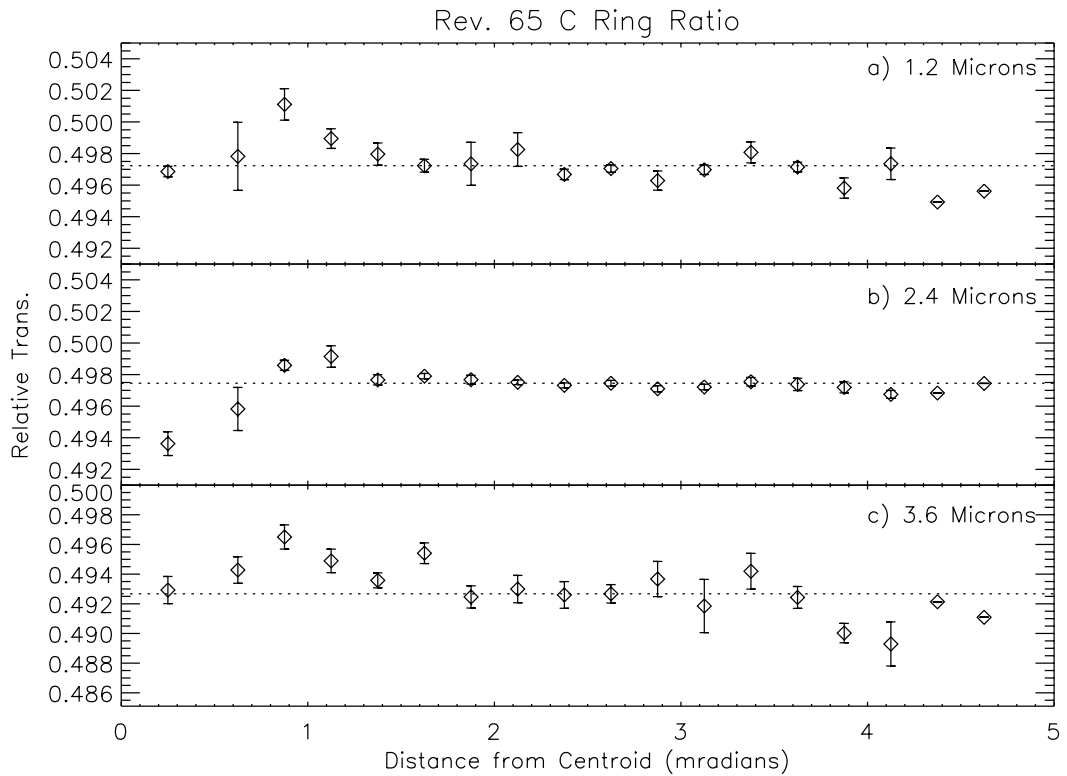
Figure 3.7: A plot of the ratio of the composite C ring image from the Rev. 65 occultation to the template created from the same occultation versus angular separation from the Sun. Data are grouped in 0.25 milliradian bins, and the error bars mark one standard error of the mean for the binned data. The dotted line is an average transmission for the area from 1 to 4 millradians from the Sun. Each panel is a different wavelength – 1.2, 2.4 and 3.6 microns from top to bottom. Error bars are not plotted for the last two points, due to the paucity of data near the edge of the image.

sunlight is diffracted into a halo, it has to come from somewhere. The individual pixels 'on' the Sun will show some additional attenuation due to light scattered out of the beam. However a wider-angle measurement – like that of the stray light scattered within the VIMS instrument – will collect both the direct and scattered light. Were the Sun a point source and a VIMS pixel small enough to exclude all scattered light, the difference in transmission would correspond to a factor of two in optical depth. Since neither is the case here, the difference is much more modest. However, this difference in transmission can be measured, and, thus, can allow the amount of light diffracted at angles larger than a VIMS pixel to be measured, even if a clear diffraction halo is not seen (as in the A Ring measurements shown in Figure 3.6). This provides the concept behind our second approach, which we will elaborate on in the next section.

3.5.2   Quantifying Transmission Differences

Let us construct a simple model for imaging the Sun with VIMS. The Sun is not a point source, so even an unocculted Sun will take up several VIMS pixels. For simplicity, we assume that the direct solar flux – that not scattered by the solar port's optics or diffracted outside the sun's disc by small ring particles – is confined to an area of N_s pixels, which can be measured from the unocculted template we created in the previous section. When the Sun is behind the rings, there is an additional halo of diffracted light from small particles (defined as those capable of scattering light outside of the solar disc), covering N pixels. This is shown in Figure 3.8.

Let the total direct (i.e., excluding that scattered within the VIMS solar port
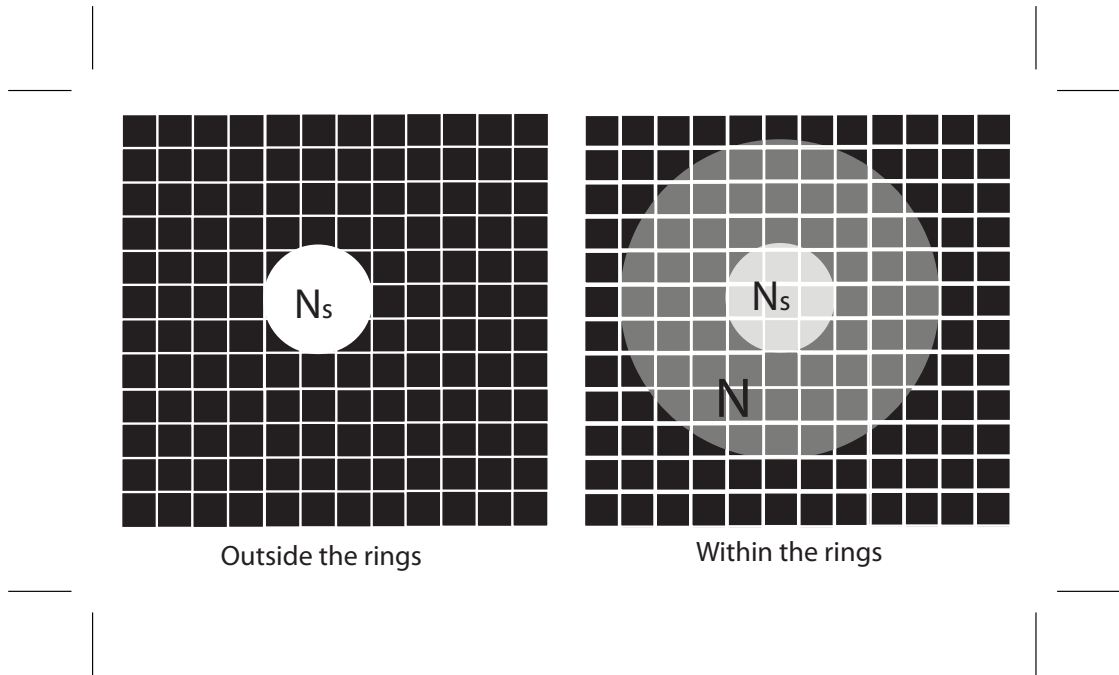
Figure 3.8: Diagram showing our model for measuring light diffracted by the rings. The Sun takes up a small number of VIMS pixels, N_s. While behind the rings, N pixels (including the N_s pixels) would show a small increase in flux from diffracted light. If one were to coadd the image as a single measurement, the Sun would appear to have a higher transmission (and, thus, a lower optical depth) than if we were to only examine the N_s pixels 'on' the Sun. This difference in optical depths should be easier to measure than attempting to measure the increase in signal in one (or a few) of the N pixels, as it sums the entire effect of light scattered outside the central N_s pixels.

optics) unocculted solar signal be S_s, measured in DN per integration at a specific wavelength, λ. In addition, as mentioned in Section 3.2.2 and illustrated in Figure 3.1, there is a diffusely-scattered background signal, spatially non-uniform, denoted by

$$\sigma_{ob}(x, y) = \beta(x, y) S_s \tag{3.7}$$

which we assume scales in brightness with the direct solar signal, but is spectrally different than the direct signal S_s (Figure 3.2). The total integrated signal within the unocculted solar image (the N_s pixels that are 'on' the Sun) can be written schematically as

$$S_0 \approx S_s + N_s \langle \sigma_{ob} \rangle, \tag{3.8}$$

where $\langle \sigma_{ob} \rangle$ is a mean of $\sigma_{ob}(x, y)$. We can estimate the values of S_s and $\langle \sigma_{ob} \rangle$ by fitting a two-dimensional Gaussian profile, plus a constant offset, to the central part of the template image.

With the sun occulted by the rings, its total flux (direct plus diffracted) is reduced by a factor $T = e^{-\tau/2\mu}$. The total flux from the sun is thus TS_s. A portion of this flux has been diffracted by the rings at angles $\theta \lesssim \theta_2$. We denote the fraction of the full solar flux diffracted into the range $\theta_s \leq \theta \leq \theta_2$ by f, where θ_s is the effective radius of the solar image in the VIMS cubes, or about 0.5 mrad. Therefore, $N_s \approx \pi \theta_s^2$. The diffracted flux is then fS_s, which is assumed to be spread uniformly over an area of $N \approx \pi \theta_2^2$ pixels, centered on the solar image.

Three measured quantities are of interest in the cubes obtained during the occultation:

1. the background signal outside the diffraction halo,

$$\sigma_{rb}(x, y) = TS_s \beta(x, y) = T\sigma_{ob}(x, y); \tag{3.9}$$

2. the background signal within the halo (i.e., in the annulus described by $\theta_s \leq \theta \leq \theta_2$), which has a mean value of

$$\sigma_{rb'}(x, y) = T\sigma_{ob}(x, y) + fS_s/N; \tag{3.10}$$

70

3. the total signal within the solar image (defined as the same area of N_s pixels above) of

$$S_r = (T - f) S_s + N_s \langle \sigma_{rb'} \rangle \qquad (3.11)$$

or

$$S_r = T (S_s + N_s \langle \sigma_{ob} \rangle) - f (1 - N_s/N) S_s. \qquad (3.12)$$

Given that we can measure S_0 and $\langle \sigma_{ob} \rangle$ by fitting a two-dimensional Gaussian curve plus a constant to the data of the unocculted sun, as mentioned above, the only remaining unknown is S_s. We can use Equation 3.8 to rewrite Equation 3.12 in terms of observables, rather than the unknown S_s, and we can normalize this by S_0 to get an effective transmission, T_s, measured only within the solar image:

$$T_s = S_r/S_0 = T - f (1 - N_s/N) (1 - N_s \langle \sigma_{ob} \rangle /S_0) . \qquad (3.13)$$

Note that all quantities in this expression, with the exception of f (which is the measure of scattering by 'small' particles in the ring, and which it is our goal to quantify), and N (which is set by θ_2 and thus the size of the smallest particles) can be directly measured from the data. If we estimate a minimum particle size of $a_{\min} \approx 0.5$ mm, this gives $\theta_2 \approx 2$ mrad at 2 μm. Since $\theta_s \approx 0.5$ mrad, the quantity $N_s/N \approx (\theta_s/\theta_2)^2$ is 1/16. We can thus assume that $1 - N_s/N \approx 1$, and solve Equation 3.13 for f:

$$f \approx \frac{T - T_s}{1 - N_s \langle \sigma_{ob} \rangle / S_0} \tag{3.14}$$

T is most readily obtained from Equation 3.9, using the measurements of the instrument-scattered background. In reality, $\sigma_{rb}(x, y)$ is spatially variable, so we use a Gaussian plus a constant offset fit to occulted and unocculted cubes to find the local mean background in each image. Then we obtain T by dividing the constants of the two fits:

$$T = \frac{\langle \sigma_{rb} \rangle}{\langle \sigma_{ob} \rangle}. \tag{3.15}$$

T_s is also obtained by fitting offset gaussians to the occulted and unocculted solar images and integrating over the solar disk:

$$T_s = \frac{\int F(x, y) \, dx \, dy}{\int F_0(x, y) \, dx \, dy}. \tag{3.16}$$

While gaussian curves are bounded at infinity, the constant background needed to properly fit the images are not. We chose to assume the background under the solar image covers an area equivalent to the ellipse described by the fitted standard deviations of the gaussian function. This 'footprint' was chosen instead of a circle of angular radius θ_s (or the angular radius of the Sun at Saturn) to account for the distortion in the solar image: while the width of the gaussian in the x direction matches the angular size of the Sun, the image appears stretched in the z direction, as is clearly visible in Figure 3.1.

Effectively what these calculations do is to estimate f not from the diffracted light itself, but via its *removal* from the direct solar flux. The advantage of this

somewhat indirect method is that the diffracted light is spread over N pixels, while the solar image covers only N_s pixels, where $N_s/N \ll 1$ for $a_{\min} \lesssim 0.5$ mm. A secondary benefit is that the derived value of f is almost independent of the unknown quality N, so long as $N_s/N \ll 1$. Our first method (as explained in the previous section and shown in Figures 3.6 and 3.7) amounts to trying to measure the difference between the $\sigma'_{rb}/\sigma_{rb} \approx 1 + fS_s/(NT\sigma_{ob})$, which dwarfs the quantity of interest, f, by other factors, rather than measure it directly as we do here.

French and Nicholson (2000) define a similar measure of the observed scattered light, Q_{occ}: the ratio of the observed optical depth, including some fraction of scattering, to the geometric (or absorption) optical depth, as defined in their Equation 15; $\tau_{obs} = Q_{occ}\tau_{geo}$. They define the total scattered flux measured in their Equation 18, which can be written in our notation as

$$ f \approx (2 - Q_{occ}) \frac{\tau}{2\mu} e^{-\tau/\mu} \tag{3.17} $$

As a test of concept, we can refer back to Figure 3.3, which plots the direct solar signal (as measured by a Gaussian fit) in terms of transmission and as a function of wavelength. We would expect that shorter-wavelength light would have less light scattered at angles large enough to be removed from the direct signal, producing a slightly blue slope as the redder regions of the spectrum had some light removed. In a qualitative sense, this can be seen in Figure 3.3's spectrum of the C Ring (and possibly the A Ring): the region of the spectrum blueward of ~1.6 μm has slightly increased transmission than the rest of the spectrum. We also would expect that this effect would be somewhat dependent on optical depth – at low or high optical depths, such a signal would not be as

prominent as the intermediate optical depths that contain enough material to scatter, but not so much as to absorb the scattered light.

3.5.3   Measuring the Diffracted Light

Given the indications in Figures 3.6 and 3.7 that T_s is indeed slightly less than T, we can calculate f numerically as described in Section 3.5.2, by using a gaussian fit to both the template and individual cubes to calculate T_s and T – and thus, f, the fraction of light diffracted out of the solar image. As in the simple test performed above, it was necessary to take the mean of f over the entire A or C ring – with the same caveats of avoiding the trans-Encke region and the edges of the ring – in order to achieve a satisfactory signal-to-noise level. In addition, the data were binned by wavelength, taking the median of f over 10 channels, with error bars calculated from the standard errors within each bin. Based on those error bars, we focus on the region from 1.8 to 2.8 microns.

Note that this bins data far more than in the simple plots we did in Section 3.5.1. While Figures 3.6 and 3.7 were means over wide ring regions, as are these measurements of f, here we bin ten adjacent wavelength channels as opposed to examining a single channel, and reduce an entire 144-pixel image into a single measurement (while in Figures 3.6 and 3.7 each bin contains roughly a half-dozen points). Thus, we should expect a corresponding reduction of noise.

In order to predict f for a particular assumed size distribution, the model described in Section 4.3 is used and integrated over an annulus centered on the Sun. A circle of radius 0.5 milliradians (1 pixel) was chosen as the inner boundary for the model's integral. However, as a result of the optics, the data show

a clearly elliptical image of the Sun, and our measurements of f (derived from the Gaussian fits to the data) take the apparent ellipticity into account. The distortion from the optics that produced an elliptical solar image could introduce a systematic difference between model and observation, but attempting to fit the image with a circular solar image would also introduce or exclude light. Without a better mapping of the distortions caused by the boresight optics, an empirical measurement seems the best guess as defining the difference between 'Sun' and 'sky'.

As the amount of scattered light drops off sharply with increasing angle, we assume an outer radius of infinity. This introduces a negligible increase in the modeled value of f for a given $a_{\min}$ compared to what we measure. Thus, f is simply an integral over the intensity function, as specified in Equation 4.3, divided by the unocculted solar flux:

$$ f = \int F\left(\theta\right)\, d\Omega/F_0 = \frac{\tau}{4\pi\mu}e^{-\tau/\mu} \int_{0.5\mathrm{mrad}}^{\infty} \int_{0}^{2\pi} \langle \varpi_0 \rangle \overline{P}\left(\theta\right)\, \theta d\phi d\theta. \qquad (3.18) $$

As a test of robustness, we integrated a hypothetical C ring model of $\tau/\mu = 0.5$, $q = 3.1$, $a_{\max} = 10$m and several lower particle size cutoffs for varying inner radii. The results are shown in Figure 3.9. Expanding the inner radius to an unphysical two times the solar angular radius in the image can reduce the minimum particle size by a factor of 2. Consequently, any plausible error in estimating the 'correct' annulus for the model would result in an overestimate of the particle size (as it seems unlikely that the most appropriate annulus would have an inner radius smaller than the solar radius).

The C Ring occultations yield three data sets (those from Revs. 9, 62, and 65)

75
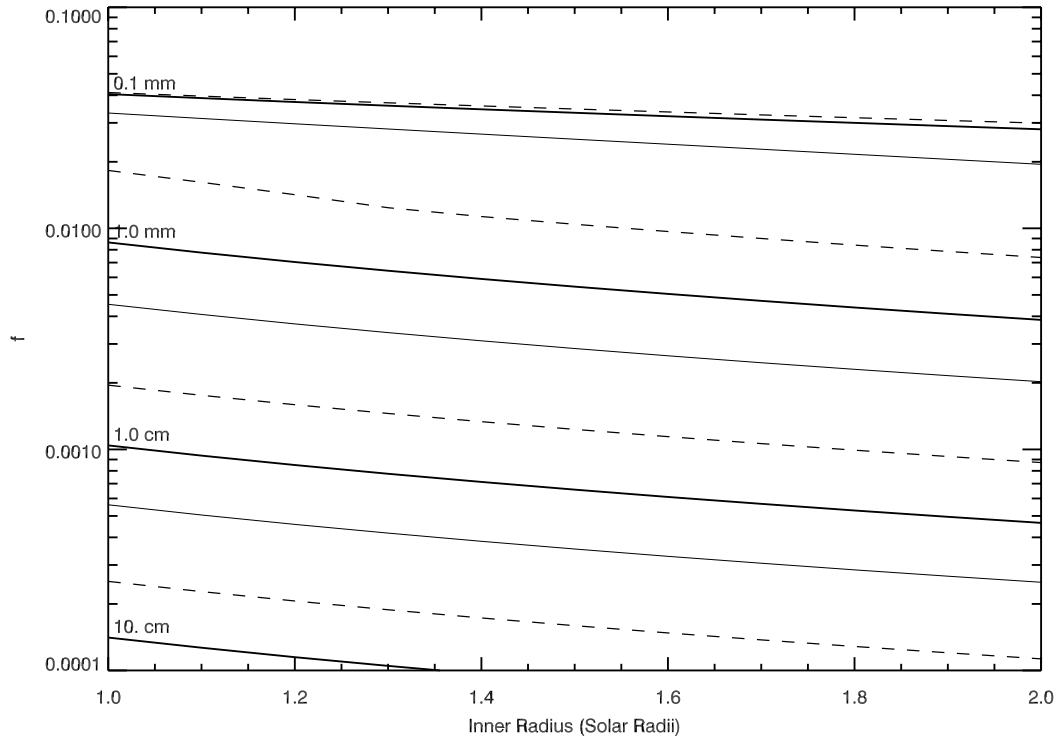
Figure 3.9: Plots of the fraction of scattered light expected from hypothetical C ring models ($\tau/\mu = 0.5$, $q = 3.1$, $a_{\max} = 10$m, $a_{\min}$ as listed) versus the inner radius of the integral in terms of solar angular radius at Saturn. While there is a clear dependence, varying the inner radius by a factor of two can, at most, produce an effect of a factor of two on inferred particle size.

which show a significant fraction of scattered light over the full spectral range considered (2 to 2.8 microns), and one more (Rev. 59) which shows a significant non-zero fraction of scattered light over part of this range. Table 3.2 includes the mean transmissions (T) and opening angles. The Rev. 11 occultation does not give a significant detection; of the occultations, Rev. 11 has the highest background and it could be that statistical noise overwhelmed the signal.

Figure 3.10 shows our three positive (and one marginal) detections. As many of the C Ring solar occultations are non-uniformly sampled by radius, direct

comparisons between occultations may be misleading if there are variations in particle size within the C Ring. There is a mix of nearly radial occultations (Revs. 9 and 11), which sample all parts of the C Ring evenly, and occultations that cut across the ansae, which sample the innermost portions of the occultation more heavily (Revs. 59, 62, and 65).

Given a model of the scattered light as discussed above and using values of a_{max} = 10 meters and q = 3.1(Zebker et al., 1985), the three positive detections (Rev. 9, Rev. 62 and Rev. 65 occultations) yield a minimum particle size of between 0.2 and 2 cm. This range is of the same order as that derived by Marouf et al. (2008) for the C Ring. The slightly lower signal in the Rev. 65 and 62 occultations could indicate a slightly larger particle size cutoff in the inner portions of the C ring, as these two occultations oversample the inner regions, but the result is not at the 3σ level given the error bars, especially those of the Rev. 62 occultation.

The minimum particle size derived is somewhat dependent on the other model parameters a_{max} and q – a steeper power-law or a smaller maximum particle size will increase the fraction of optical depth in smaller particles, and increase the amount of scattering at angles greater than θ_s. In our angular regime, namely that of large-angle scattering, the strongest effect is with q: a steeper power-law (larger q) implies more particles with sizes small enough to scatter at the relevant angles. Consequently, for a given value of f, a steeper power-law leads to a larger a_{min}. a_{max} has only a weak effect; a larger maximum size reduces the number of particles per unit area for a given optical depth, slightly lowering the minimum size for the same value of f. However, for $q > 3$, as has been previously derived for the C ring (Zebker et al., 1985), most of the cross-sectional
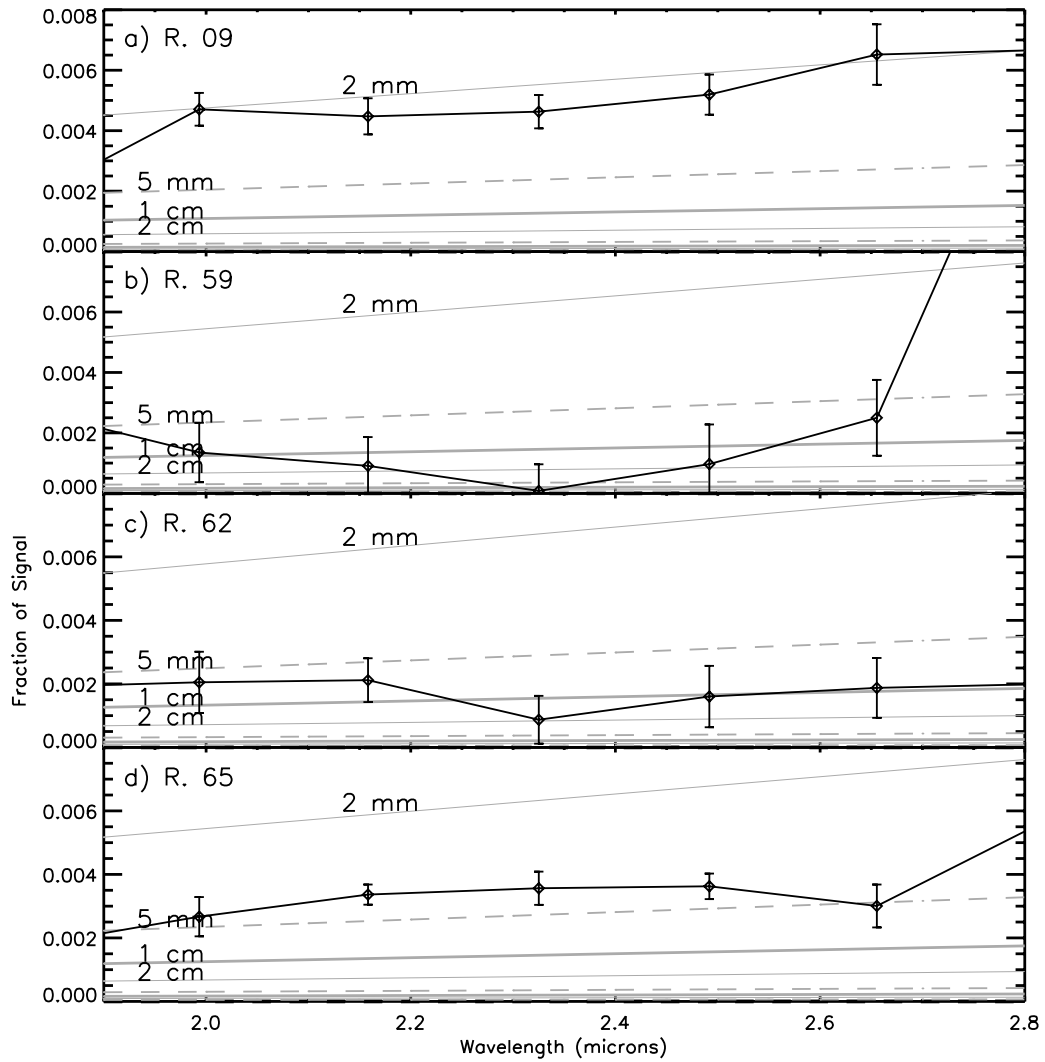
Figure 3.10: Plots of the scattered light fraction, f, versus wavelength for four C ring occultations – Rev. 9 (a), Rev. 59 (b), Rev. 62 (c), and Rev. 65 (d) – calculated using Equation 3.14. The regularly-spaced arcs show models with $a_{max} = 10$ m, $q = 3.1$, and minimum particle sizes of 2, 5, 10, 20, 50, and 100 mm (unlabeled). Note that Revs. 9, 62 and 65 show a significant fraction of scattered light that corresponds to a minimum particle size between 2 and 20 mm, while the Rev. 59 occultation only produces a marginal detection of diffracted light with a minimum particle size larger than 5 mm.

area is in small particles, so a modest increase in the number of large particles produces an inconsequential effect on scattering at this angular scale.

Figure 3.11 plots a_{min} vs. q for the C ring. The function was calculated by taking the scattering fraction from the Rev. 9, Rev. 62 and Rev. 65 occultations (the three in which a clear positive detection was made) at a wavelength of 2.3 μm, and calculating the a_{min} for a given q needed to produce the observed scattered light. The line plotted in Figure 3.11 is then a mean of the values of a_{min} calculated from each of the three occultations. At $q = 3.1$, corresponding to previous estimates of the C ring power-law index (Zebker et al., 1985; French and Nicholson, 2000; Marouf et al., 2008), we find a value of $a_{\mathrm{min}} = 4.1^{+3.8}_{-1.3}$ mm. The C ring shows a robust value of a_{min} somewhere between 0.3 and 1 cm for values of q between 2.95 and 3.5.

Completing the same analysis on the A ring – shown in Figure 3.12 – shows a significant fraction of scattered light in five occultations (Revs. 9, 43, 55, 59, and 62) over the same wavelength range. Rev. 65 shows a partial detection over some of the range. Note that comparing the far-field signal to the decrease in signal, and binning by wavelength, produces a far clearer detection in Rev. 43 than seen in Figure 3.6. However, unlike the C ring, which is homogenous and optically thin ($\tau/\mu \lesssim 1$), the A Ring is neither. Those complicating factors, self-gravity wakes and the possibility of multiple scattering, are examined below and our simple model modified appropriately.
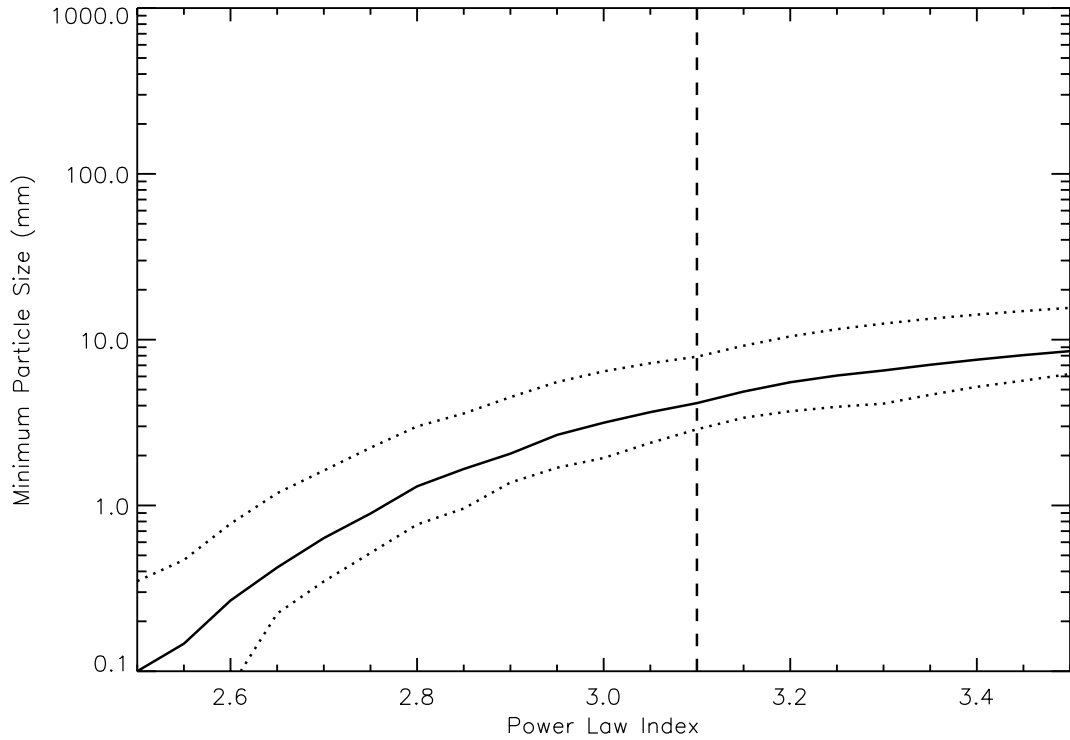
Figure 3.11: A plot of a_{min} as a function of q in the C ring, assuming a maximum particle size a_{max} = 10 m and for a wavelength of 2.3 μm. The dotted lines represent 1σ errors on the estimates, combining both the differences between the calculated value of a_{min} from each occultation, and the errors of each occultation's a_{min} (calculated from the errors in f calculated from binning nearby wavelengths). The dashed line at $q = 3.1$ represent previous estimates of the power-law index for the C Ring. (Zebker et al., 1985; French and Nicholson, 2000; Marouf et al., 2008)
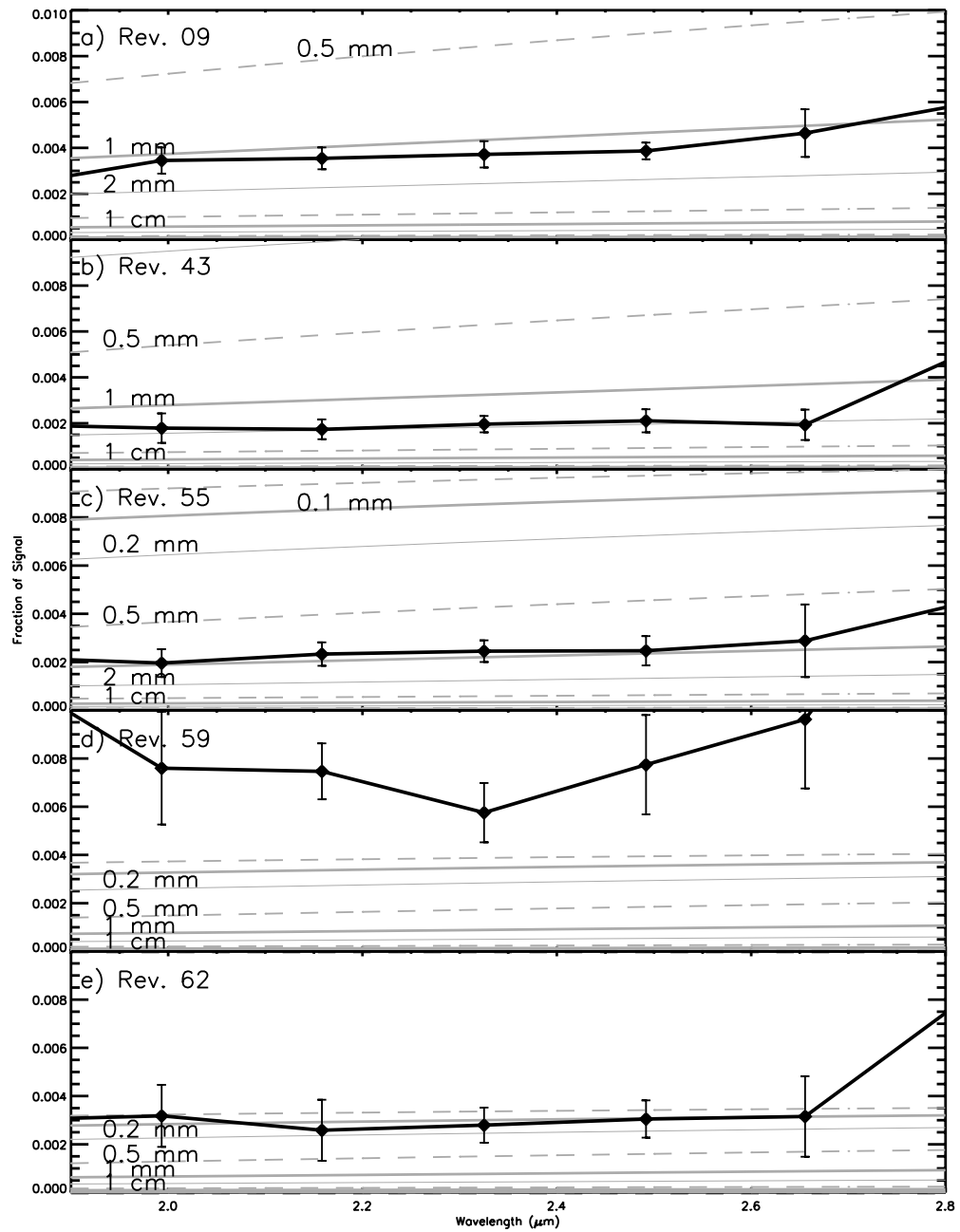
Figure 3.12: Five A ring occultations – Rev. 9 (a), Rev. 43 (b), Rev. 55 (c), Rev. 59 (d), and Rev. 62 (e) – compared with single-scattering models (a_{max} = 10 m, q = 2.9, and minimum particle sizes from 0.1 mm to 10 cm) with minimum particle size listed, calculated using Equation 3.14.

3.6 The A Ring: Increased Optical Depth and Inhomogeneities

3.6.1 Introduction to Self-Gravity Wakes

Re-examining the assumptions made in the model described in Section 4.3, we see that one stands out. The model assumes that the ring in question is made up of a thick slab with a homogenous distribution of particles. However, the A ring is not well described by this model. Observations show that the A ring has an azimuthally-dependent optical depth, which varies by up to a factor of a few depending on the longitude relative to the planet-to-star direction that is sampled by the occultation (Colwell et al., 2006; Hedman et al., 2007c). The accepted explanation for this variation, based on numerical simulations of this ring, is the presence of self-gravity wakes (Salo, 1992).

Because the self-gravity wakes are long aggregates of particles with a characteristic trailing orientation with respect to the radial direction, they change the optical depth depending on the cross section they present to the beam of light, which depends on the observed longitude with respect to the stellar direction, ϕ. They also don't show the simple $1/\mu$ dependence of τ on opening angle, instead following a more complicated relation.

Our next step in modeling ring scattering within the A ring is to account for the wakes within the ring.

3.6.2 Scattering with Opaque Wakes

Following Hedman et al. (2007c), we assume the A ring consists of a parallel series of cylindrical wakes of characteristic width W, height H, spacing λ and alignment ϕ_W measured relative to the radial direction. The wakes themselves are opaque, but the interwake 'gaps' have a finite optical depth τ_G due to particles outside the wakes. Tiscareno et al. (2010b) show that this is not an exact description of the wake behavior in dynamical simulations, but that this simple model reproduces optical depth measurements for opening angles larger than $\sim 10°$. As none of the occultations we use for the A ring measurements are less than $\approx 8°$, Hedman et al.'s wake model should be sufficient for our purposes.

We assume that the particles within the gaps form a homogenous layer so that the same model used earlier applies within the gaps. If f_W is the fractional area of ring covered by the wakes as viewed by VIMS (which depends both on the opening angle of the rings (B), and the longitude (ϕ), as well as the parameters W, H, λ and ϕ_W), then the fraction of scattered light can be written as

$$f = (1 - f_W(B, \phi)) \frac{\tau_G}{4\pi \sin B} e^{-\tau_G / \sin B} \int \langle \varpi_0 \rangle \overline{P}(\theta) \, d\Omega, \qquad (3.19)$$

where the integrand is calculated as before. Note that for $f_W = 0$ (and τ_G, the extinction optical depth of the interwake material, equal to τ), this equation reduces to the simpler case used in the previous section.

A full derivation for f_W is given by Hedman et al. (2007c), resulting in the expression

$$f_W = \left| \frac{H \sin (\phi - \phi_W)}{\lambda \tan B} \right| \sqrt{1 + \left[\frac{W \tan B}{H \sin (\phi - \phi_W)} \right]^2}.$$ (3.20)

The values of ϕ, the longitude of the area sampled, and B are known for each occultation and are listed in Table 3.1. ϕ changes slightly as the occultation progresses, as none are totally radial occultations, but for the regions of the A ring sampled, this change is small. Repeated stellar occultations suggest that τ_G is between 0.3 and 0.6, H/λ is between 0.09 and 0.12, and W/λ is between 0.3 and 0.65 for the A ring (Nicholson and Hedman, 2010). Note that Nicholson and Hedman's values for optical depth (τ_g) correspond to absorption, so we have used the equation $\tau_G = 2\tau_g$ to derive values for extinction optical depths within the gaps. These and other studies of A ring photometry show that the wakes are oriented to have a peak transmission at $\phi_W \approx 70°$ and 250° longitude (with 0° being the direction to the Sun (or star) from Saturn) (Nicholson and Hedman, 2010).

The effect of the wakes on f is not simple. While f_W decreases the ring area which provides the scattered signal, replacing τ by the much smaller τ_G increases the amount of scattered light available when $\tau/\mu > 1$, which is usually the case in solar occultations by the A Ring.

3.6.3 Effects of Multiple Scattering

Our first model assumed that all light interacts with a ring particle once and is absorbed, (singly-)diffracted or transmitted. However, in reality the ring particles we are considering are far smaller than the thickness of the ring, so multiple scattering is possible. For $\tau/2\mu \ll 1$, the contribution from light diffracted

more than once is small. However, even when we consider an expected normal optical depth of 0.3 to 0.65 (the estimated extinction optical depth between self-gravity wakes in Hedman et al. (2007c)), only the Rev. 9 occultation at $B = 21.5°$ (and the lowest optical depth estimate of the gap material) satisfies $\tau/2\mu < 1$.

Zebker et al. (1985), in analyzing the low incidence Voyager radio occultations, developed a scheme for handling multiple scattering in a thin ring. They treat the ring as N layers of optical depth $\tau_1 = \tau/N$, where $\tau_1 \ll 0.5$, so that within each layer, the single scattering approximation holds. This model allows for multiple scattering (to degree N) by calculating the fraction of absorption, scattering or transmission through each layer and treating it as a sum of terms to produce the intensity function. The phase function for multiple scattering is treated of a convolution of single scattering, as Zebker et al. (1985) do in their Equation 7. In the notation used in this paper, we can write their equation as

$$\frac{I_{sca}(\theta)}{F_0} = \sum_{k=1}^{N} \binom{N}{k} e^{-\tau(N-k)/N\mu} \left[\frac{I_1(\theta)}{F_0} \right]^k, \tag{3.21}$$

where $I_1(\theta)$ is the intensity distribution from single scattering within a layer of ring, as calculated from Equation 4.3 (but without the solid angle that changes an intensity into a flux), using τ_1 as the optical depth. $[I_1]^k$ represents the kth convolution of I_1 with itself, so each term of the sum represents the contribution of kth order scattering to the whole, with an attenuation factor to account for absorption by the $N-k$ other layers, and a combinatoric factor $\binom{N}{k}$ to account for the k layers chosen from N to scatter photons. We can also re-write Equation 3.21 in terms of the phase function for single scattering, $P(\theta)$, to remove quantities not dependent on θ, and to bring out the 'hidden' τ_1 in the intensity distribution:

$$\frac{I_{sca}(\theta)}{I_0} = e^{-\tau/\mu} \sum_{k=1}^{N} \binom{N}{k} \left(\frac{\varpi_0 \tau}{4\pi N\mu}\right)^k [P(\theta)]^k. \tag{3.22}$$

N is an approximation for the number of particles (of the size doing the scattering) thick the ring is. As mentioned earlier, the Voyager radio occultation was most sensitive to suprameter particles, with smaller particles sensed only as a differential optical depth between the two wavelengths of radio waves transmitted through the rings. As the rings are thin relative to meter-sized particles, even when considering the slant-path at low incidence angles, Zebker et al. could assume N was small and search for the value of N which best agreed with the data. However, in the case of millimeter-sized particles, the rings are no longer physically thin relative to the particle diameter, even at normal incidence angles. Thus, rather than N being a few, it becomes on the order of a thousand.

If we let N become large, then the equation becomes

$$\frac{I_{sca}(\theta)}{I_0} = e^{-\tau/\mu} \sum_{k=1}^{\infty} \frac{1}{k!} \left(\frac{\varpi_0 \tau}{4\pi\mu}\right)^k \left[\bar{P}(\theta)\right]^k. \tag{3.23}$$

We will be using this equation to include the effects of double- and triple-particle scattering. Higher-order terms are small relative to these terms, so were omitted. From Figure 3.13, we can see that double-particle scattering produces the dominant effect at angles larger than the ~ 0.5 milliradians that marks the size of the solar image (and, thus, the minimum angle required to remove light from the signal), confirmation of the necessity of accounting for multiple-particle scattering. Conceptually, this can be explained as the more times a photon is scattered, the broader the diffraction cone becomes. If little light is being singly scattered at a certain angle, doubly scattered light will dominate if the ring is optically thick enough. The decrease in intensity from single and double-particle scattering to triple-particle scattering justifies our neglect of

higher-order terms.
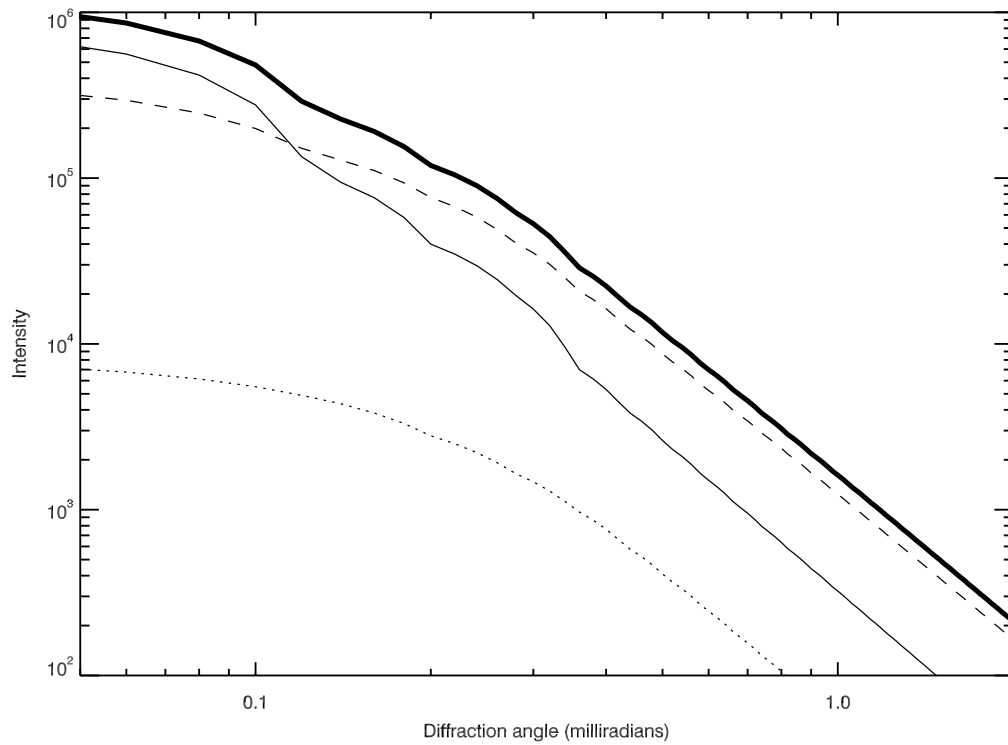
Figure 3.13: Plot of the contributions of single (solid), double (dashed) and triple (dotted) particle scattering to the total intensity (thick) of the scattering versus diffraction angle for an optical depth of $\tau/\mu = 1$, a wavelength of 2 μm, and a power-law particle-size distribution of index $q = 2.9$, from 1 mm to 10 m. These conditions are roughly analogous to the A Ring. Note that, in fact, double-particle scattering dominates over single-particle scattering at ~1 milliradian where our observations are most sensitive. Triple-particle scattering and higher-order terms (not shown) make up a minor part of the scattering function.

3.6.4   Measuring Diffracted Light in the A Ring

Now that we have discussed the complicating effects of multiple-order scatter-ing and self-gravity wakes, we can add them to the model. Note that the two

effects to an extent work against each other: multiple-order scattering will increase the amount of scattered light for a given optical depth, while self-gravity wakes will lower the material available to scatter light, which will decrease the scattered light in general (as well as add a longitude-dependent term). It is not obvious which (if either) effect will dominate at the scales we are interested in for this problem.

To model the A Ring, we had to choose parameters to represent the self-gravity wakes. The wake dimensions of W/λ=0.5 and H/λ=0.1 were chosen as representative parameters from the stellar occultation data discussed in Section 3.6.2. Individual values of τ_G for each cube were calculated based on those numbers and assuming $T = (1 - f_W) e^{-\tau_G/2\sin B}$, with T being the calculated transmission in that cube and f_W calculated from Equation 3.20.

As before, the values of f were averaged over the entire A ring, and binned spectrally. Figure 3.14 shows the binned and rescaled measurements of f for five occultations, with representative models. For a comparison, a wakeless model using the full observed optical depth (but including multiple scattering), is also shown in Figure 3.15.

Of the five clear positive detections mentioned in Section 3.5.3 the diffracted light measurements were larger than we'd expect from models for the Rev. 59 and Rev. 62 occultations. Below $a_{\min} \approx 100$ microns, the fraction of light removed from the direct signal becomes nearly constant, as the models are no longer dominated by the large-angle 'tails' of diffraction from the millimeter-sized and larger particles in the ring. Rev. 62's measurements only allow an upper limit on $a_{\min}$ to be set, rather than having a value that best agrees with the data, and the data from Rev. 59 are inconsistent with the model entirely for the value of
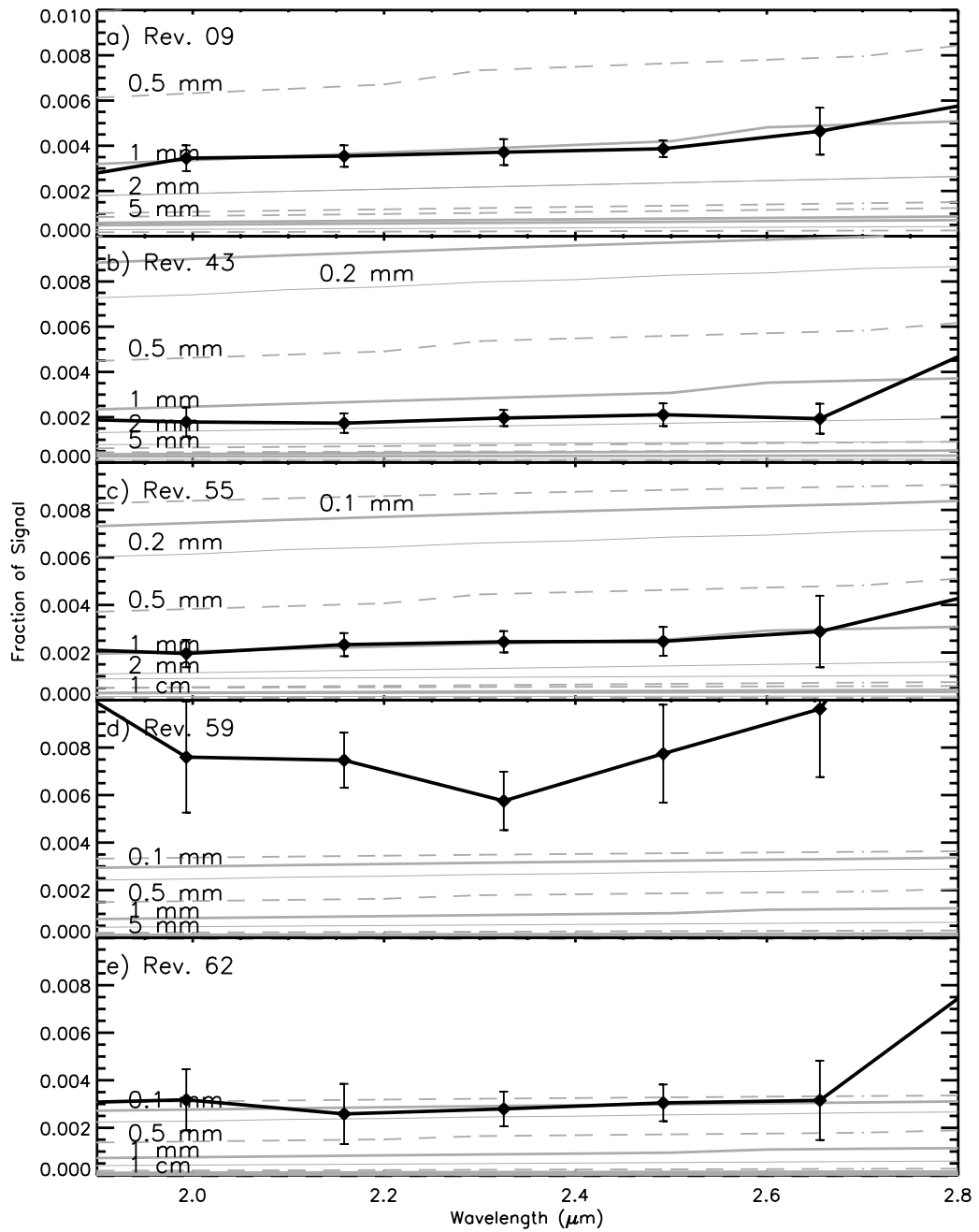
Figure 3.14: Five A ring occultations – Rev. 9 (a), Rev. 43 (b), Rev. 55 (c), Rev. 59 (d), and Rev. 62 (e) – compared with models ($a_{\max} = 10$ m, $q = 2.9$, minimum particle sizes from 0.1 mm to 10 cm, self-gravity wakes and multiple scattering included) with minimum particle size listed.
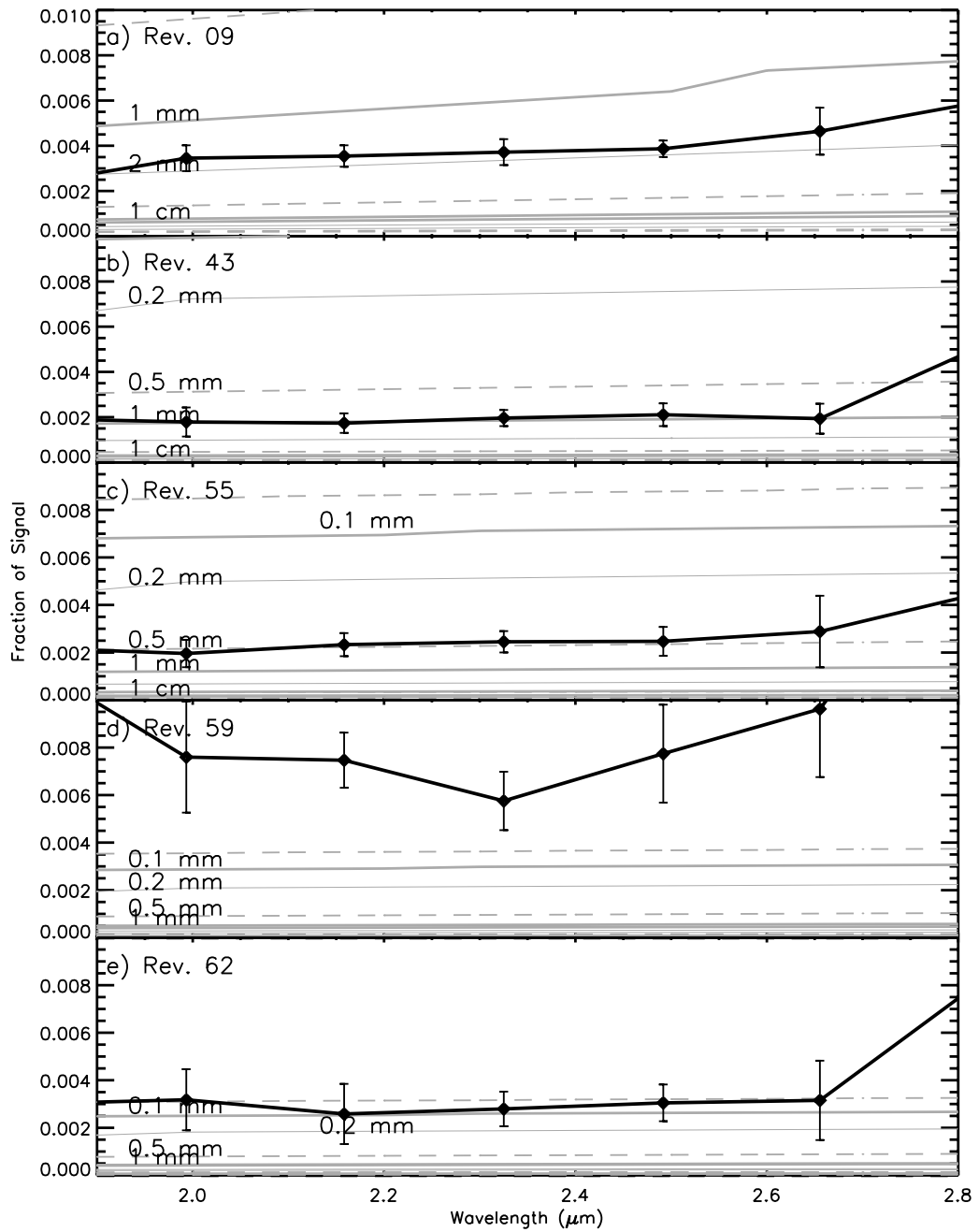
Figure 3.15: Five A ring occultations – Rev. 9 (a), Rev. 43 (b), Rev. 55 (c), Rev. 59 (d), and Rev. 62 (e) – compared with models ($a_{max} = 10$ m, $q = 2.9$, minimum particle sizes from 0.1 mm to 10 cm, and multiple scattering included, but self-gravity wakes not included) with the minimum particle size listed.

q used. Omitting the effects of self-gravity wakes, as in Figure 3.15, changes the minimum particle size corresponding to a given value of f, but still cannot reproduce the Rev. 59 observations.
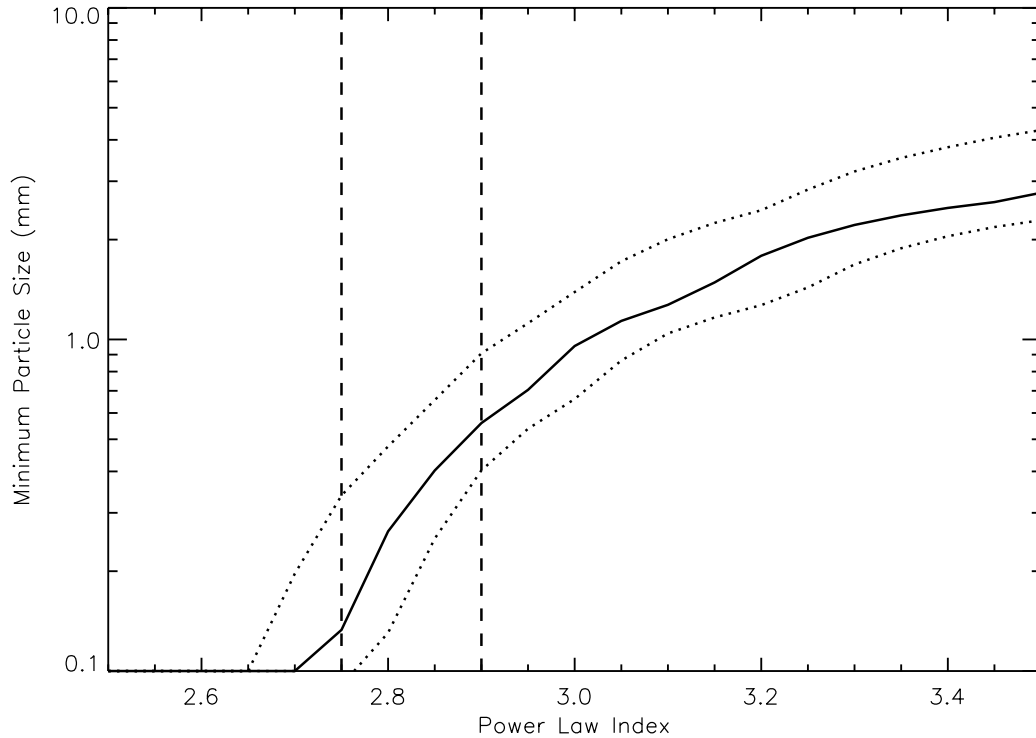
Figure 3.16: A plot of a_{min} as a function of q in the A ring for a wavelength of 2.3μm, assuming wake properties as listed in the body of the text and a maximum particle size a_{max} = 10 m. The function was calculated by taking the scattering fraction from the Rev 9, 43, and 55 occultations, and calculating the a_{min} for a given q needed to produce the observed scattered light. A mean was then taken of the three functions. The dotted lines represent 1σ errors on the estimates, combining both the differences between the calculated a_{min}s from each occultation, and the errors of each occultation's a_{min} (calculated from the errors in f calculated from binning nearby wavelengths). The dashed lines at q = 2.75 and q = 2.9 represent previous estimates of the power-law index for the A Ring. (Zebker et al., 1985; French and Nicholson, 2000; Marouf et al., 2008)

To better quantify our results, we again calculated the mean $a_{\min}$ over the three occultations (Revs. 9, 43 and 55) for which a clear detection (rather than an upper bound) was observed, as a function of q from the fraction of scattered light observed at 2.3 microns, just as we did for the C ring. The results are shown in Figure 3.16. Using the diffraction model that accounts for both the effects of self-gravity wakes on optical depth and double- and triple-particle scattering, we infer that the minimum particle size is $0.56^{+0.35}_{-0.16}$ mm at a power-law index of 2.9, the index inferred by the Voyager Radio Science experiment (Zebker et al., 1985). The shallower $q = 2.75$ power-law index observed by French and Nicholson (2000) lowers the minimum particle size to an upper limit of < 0.18 mm. Including the Rev 59 and 62 occultations in the mean $a_{\min}$ lowers these values further to $0.38^{+0.27}_{-0.12}$ mm at $q = 2.9$, but cannot replicate all the observations using $q = 2.75$.

Both the homogenous ring and wake model give a minimum particle size somewhat smaller for expected values of q (between 2.7 and 3.0) than those seen by the Cassini RSS measurements and French and Nicholson's observation of few sub-centimeter-sized particles in the 28 Sgr occultation (Marouf et al., 2008; French and Nicholson, 2000). Zebker et al. (1985) note that the difference in optical depth between that measured at λ=3.6 cm by Voyager and that measured at 0.5 μm is large enough to suggest the existence of a substantial population of sub-centimeter sized particles, but a significant difference in optical depth between the 3.6 and 0.9 cm bands in the A Ring was not seen by Cassini RSS occultations (Marouf et al., 2008), implying few particles in the centimeter size range.

A major caveat to all of these studies is that none of them accounted for

the effects of self-gravity wakes, though Zebker et al. (1985) and Marouf et al. (2008) both included analysis of multiple scattering effects. French and Nicholson (2000) even notice what could have been a longitudinal asymmetry in optical depth in the A Ring between the δ Sco and 28 Scr optical depths, but, without a model, chose to adopt a 'fudge factor' to scale the two occultations as best they could. A model of the A Ring that includes self-gravity wakes would lower the expected differential optical depths between all wavelengths smaller than the wake size, as a fraction of the optical depth would be caused by the wakes themselves, rather than the continuum of ring particles. Therefore, a wakeless model would find larger minimum particle sizes for a given differential optical depth than a model that included self-gravity wakes. It is also worth mentioning that our (and others') observations derive distributions for the material in-between the wakes, which may be different in size distribution from the ring as a whole.

Using the three-occultation mean, our model requires < 12.1 % of the inter-wake optical depth to be from particles smaller than 1 cm at q = 2.75, which increases to $20.1^{+4.2}_{-1.2}$ % for q = 2.9. For typical interwake optical depths used earlier (τ_G between 0.3 and 0.65 in extinction), this gives extinction optical depths due to such small particles of between 0.03 and 0.16, within Zebker et al.'s range.

3.7   Conclusions

When analyzing the solar occultation data recorded by Cassini-VIMS, we observed a small excess of forward-scattered light, once instrumental effects were taken into account. We believe this to be due to diffraction by small particles in the rings and have used it to estimate minimum particle sizes, assuming a

power-law index, q, and maximum particle size from previous work (Zebker et al., 1985; French and Nicholson, 2000; Marouf et al., 2008).

Among the three C Ring solar occultations in which a clear positive excess was measured, a minimum particle size of $4.1^{+3.8}_{-1.3}$ mm is inferred for a canonical value of $q = 3.1$. For a wider range of likely q values, the data still indicate a minimum particle size between 3 and 10 mm. This is somewhat larger than the $a_{\min} \approx 4$ mm measured by Marouf et al. (2008) using the Cassini Radio Science experiment, and it's possible this could be due to a radial variation of minimum particle size in the C Ring, as the chord occultations (Rev. 62 and 65) show a larger minimum than the Rev. 9 radial occultation. Further work would be required to confirm such a variation.

In the A Ring observations, multiple-particle scattering produces a non-negligible effect due to the larger optical depths involved, and must be taken into account to explain the larger-than-expected amount of scattered light seen. The effects of the A Ring's self-gravity wakes on the amount of scattering are more complicated, but are clearly seen in optical depth measurements of the A Ring from both these solar occultations and other data sets (such as stellar occultations). The shallow power-law indices of $q = 2.75$ found by French and Nicholson (2000) and Marouf et al. (2008) require a very small $a_{\min}$ of < 0.34 mm to explain our observations, even accounting for multiple scattering and self-gravity wakes. Raising the power-law index to $q = 2.9$ as measured by the Voyager radio occultations (Zebker et al., 1985) still requires particles of $0.56^{+0.35}_{-0.16}$ mm to explain the amount of scattered light measured by our solar occultation observations. These numbers appear to be inconsistent with estimates of a lack of material smaller than one centimeter advanced by French and Nicholson

(2000), but the shallow power-law and amount of material sequestered in self-gravity wakes may mean the optical depth required in particles smaller than 10 mm could be as small as $\tau = 0.03$ in extinction. This may render our data consistent with this lack of optical depth variation with wavelength seen in radio occultations, especially when the effects of self-gravity wakes are taken into account.

We were also able to constrain the fraction of free-floating ice grains smaller than 100 μm in the A ring to be $\leq$ 5%, assuming a dust size distribution similar to the F Ring. The fraction within the C ring was even smaller: $\leq$ 1.4%. Regardless of their minimum particle sizes, it is clear that the A and C Rings lack the persistent icy dust that is a strong feature of the F Ring.

CHAPTER 4

PARTICLE SIZES NEAR THE GAPS OF SATURN'S RINGS, HARBISON, R. A. & NICHOLSON, P. D. IN PREP. FOR *ICARUS*

4.1 Introduction

The size distribution of particles within Saturn's rings has been characterized in the last few decades mostly through the diffraction and absorption through occultations. Typical ring particles – with sizes in the centimeter, decimeter and meter range – diffract at tiny angles in the visible and near infrared (from a fraction of a milliradian down to tens of *nano*radians). With the exception of Harbison et al. (2013)'s work at the smallest end of the particle-size distribution, this effect has not been observed spatially. However, both radio (Marouf et al., 1983) and visible/near infrared(French and Nicholson, 2000) have observed the effects projected into other dimensions of their data.

Specifically French and Nicholson (2000) observed the occultation of the star 28 Sagitarii (28 Sgr) by the rings from Earth in 1990. During the occultation, French and Nicholson collected time series of 28 Sgr's brightness as it crossed through the rings, as well as background measurements of ring and planet brightness to correct for those effects. Thus, they were able to produce a detailed time series of ring optical depth, which could be converted into a radial measurement based on the star's apparent track across the rings. During these observations, they observed that several gaps in the C and A Rings and Cassini Division, as well as the regions immediately interior and exterior to the Main Rings, had total fluxes above the baseline for the star, measured to be 5-10 % larger than the unocculted stellar flux. They attribute this to starlight diffracted

by nearby ring material at angles such that it appears to come from the empty gap, and successfully model this using a simple truncated power-law particle size-distribution and an assumption that each region of the rings (the A, B and C rings, the Cassini Division and the trans-Encke A Ring) is uniform in particle properties.

French and Nicholson's work 2000, combined with the radio occultations by Voyager (Marouf et al., 1983; Zebker et al., 1985) and Cassini (Marouf et al., 2008) and near infrared solar occultations observed by Cassini (Harbison et al., 2013), have given us a more complete picture of the particles within Saturn's rings. The varying wavelengths and geometries of these observations prove to be complimentary in filling in different regimes of the particle-size distribution. A fuller description of the work can be found in Cuzzi et al. (2009), but we will give a brief overview here.

Direct inversion of radio occultations shows a strong break in particle radius at 3-5 m (Marouf et al., 1983) in those regions of the rings measured, making a power-law truncated at the meter scale a reasonable model. For the C Ring, Zebker et al. (1985) and French and Nicholson (2000) agree on a power-law index in the centimeter and decimeter particle size regime of $q \approx 3.1$, with Marouf et al. (2008) preferring a slightly larger $q \approx 3.2$, with errors of roughly 0.1 in both papers. Both Marouf et al. (2008) and Harbison et al. (2013) agree on a minimum particle size of about 4 mm. In the Cassini Division, the outer ramp is the main region studied by radio occultation, but all three experiments agree on a power-law index of about $q \approx 2.75$ (Zebker et al., 1985; French and Nicholson, 2000; Marouf et al., 2008). All three also agree that the power-law index within the A Ring steepens as one looks outward, with estimates of the index outside the

Encke Gap ranging from 2.9 (French and Nicholson, 2000) to 3.2 (Marouf et al., 2008). Marouf et al. (2008) also estimates a minimum particle size of 4-5 mm in the region outside the Encke Gap (Harbison et al.'s work does not extend to the outer A Ring).

Since its insertion into Saturn orbit in 2004, the Cassini spacecraft has measured dozens of stellar occultations using several instruments. We will be focusing on those observed in the near-infrared, using the Visible-Infrared Mapping Spectrometer (VIMS). In these occultations, the increase in stellar flux is often visible on inspection of the data, and even shows a 'horned' structure due to the change in number and size of ring particles diffracting light that appears to come from a certain location within the gap. Individual ringlets within gaps – such as the Huygens, Herschel and Laplace Ringlets in the Cassini Division and the Maxwell and Titan Ringlets in the C Ring – even produce their own horned features surrounding them as separate from the gap edges.

In this chapter, we will be measuring and modeling these features using the same truncated power-law particle size-distribution. While the particle sizes we are sensitive to are in the same centimeter to decimeter range that has been well covered, the angular and time resolution of Cassini's occultations allows for a study of regions of the rings that are only hundreds of kilometers wide, rather than the wide swaths modeled in the radio science occultations, or the whole ring regions used in the earthbound work, as well as examination of the ringlets. As our measurements correspond to the middle of the truncated power-law size distribution, we are most sensitive to the effective power-law index, but we also discuss the effects of lower particle size cutoffs and what can be learned from this data set.

4.2 Data Collection

We are examining a collection of stellar occultations of Saturn's Rings as observed from the Cassini Spacecraft. The data were collected over four years by VIMS. VIMS was operated in occultation mode, disabling the visible light detectors. In addition, the infrared detectors were binned on board the spacecraft from 256 channels to 32, spanning 0.9 to 5.2 microns. Sampling was done at intervals from 20 to 80 milliseconds, determined by the brightness of the star in the near infrared. For more information about VIMS occultation data sets, see Hedman et al. (2007c) and Nicholson and Hedman (2010).

In total, Cassini has observed 74 stellar occultations of the rings as of late 2009. Not all are suitable for this work, as those with too little signal or baselines that drifted strongly were not used. In total, 22 occultations were chosen, with inclinations ranging from 74.19° (α Triangulum Australis) to 3.45° (o Ceti).

VIMS takes periodic 'background' measurements to monitor the dark current and thermal background in the instrument, and these are subtracted automatically from the data. We observe at 2.92 μm, where the rings are dark due to the deep water-ice absorption band. Therefore we can assume that all signal seen once the dark current is subtracted comes from attenuated starlight, rather than the sunlit portions of the ring. We are able to use reconstructions of the spacecraft's path relative to Saturn and the rings during the occultation, and the right ascension and declination of the star to reconstruct the radius and relative longitude where the starlight observed by VIMS crossed the ring plane and interacted with the ring.

Rather than use absolute measurements of intensity, as we are uninterested

in the absolute brightness of the star, we calibrate the occultation profile in terms of transmission through the ring by measuring the brightness of the star in a region known to be clear of ring material. As even the most stable occultations have some drift, changing the baseline measurement of the mean Data Number (DN) per integration for the unocculted star, different calibrations are used for different ring regions. For the A Ring, a mean of 100 observations taken from the Roche Division between the A and F Rings (but well clear of either) is used. We do not use the Encke Gap, as it may not be wide enough to be free of the scattered light we seek to measure. The C Ring and Cassini division use linear trendlines as their baseline, with the C Ring's drawn between the region interior to the C ring and the middle of the Maxwell Gap, and the Cassini Division's drawn between the middle of the Laplace and Huygens gaps.

Visual inspection of these data shows that, even when correctly converted into units of transmission, empty areas of the rings that are close to areas of ring material often show apparent transmissions of greater than one, suggesting that not only is all of the starlight making it through the empty area (as expected), but additional light is being added, just as French and Nicholson (2000) observed in their Earth-based occultation studies. Moreover, the morphology of the occultation profile shows the same general shape of a sharp 'horn' at the very edge of the gap, dropping rapidly away from the edge. For examples of this phenomenon, see Figures 4.1 through 4.4.

Figure 4.1 shows the Maxwell Gap in the C Ring, with the dense Maxwell Ringlet located in the middle of the gap. The low-optical depth regions of the C Ring produce only a trace of 'horns', but, despite being nearly opaque, the ringlet's narrow (~ 10 km) 'horns' are prominent. Figure 4.2 shows the Huy-
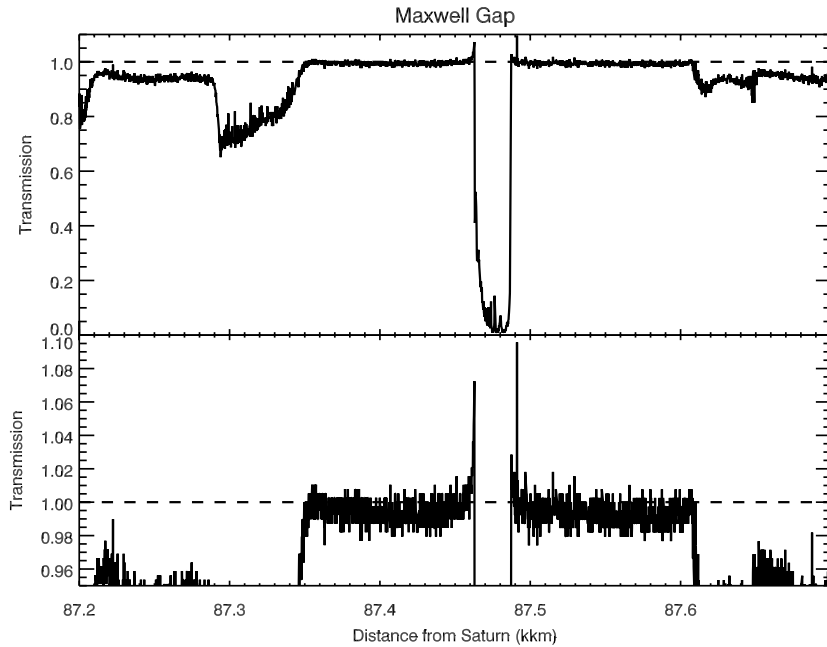
Figure 4.1: Occultation plot showing transmission through the Maxwell Gap in the outer C Ring as a function of radius (using the Rev. 100 γ Crucis occultation at $B = 62.4°$), and calibrated as described in the text, with the bottom frame zoomed to better show the slight variations from full transmission. Note the clear 'horns' around the Maxwell Ringlet, and the suggestion of a slight rise near both gap edges.

gens Gap in the Cassini Division, including the wide Huygens Ringlet and the narrow Outer Huygens (or 'Strange') Ringlet. The 'horns' from the Huygens Ringlet appear wider than both the 'Strange' Ringlet and the outer edge of the gap, though perhaps narrower than that on the inner edge. This figure is an excellent example of how these structures are not identical, suggesting the information about the nearby ring material can be derived. Also note how narrow the 'Strange' Ringlet is, despite showing clear 'horns': for narrow features such as this ringlet, the 'horns' may provide some of the only information about the properties of the particles within it. Figure 4.4 shows the Keeler Gap and the
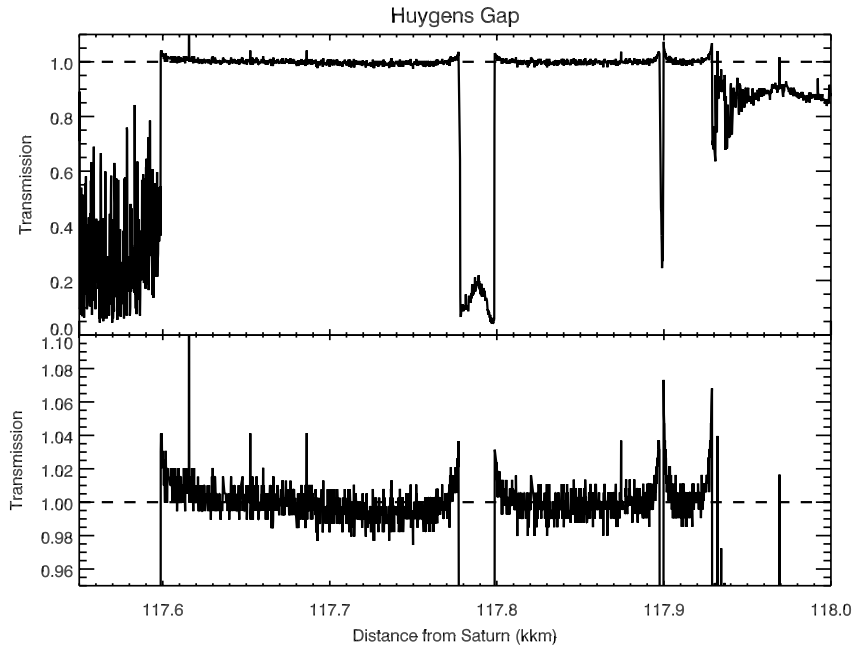
Figure 4.2: Occultation plot showing transmission through the Huygens Gap in the Cassini Division as a function of radius (using the Rev. 100 γ Crucis occultation), and calibrated as described in the text, with the bottom frame zoomed to better show the slight variations from full transmission. Note the clear 'horns' around both ringlets and at both edges.

outer edge of the A Ring. The Keeler Gap has transmission above unity for its entire width – seen relative to the large clear area outside the A Ring – showing why we avoided narrow gaps in trying to normalize our occultations. The Keeler Gap is also visibly asymmetric, indicating that the gap marks a change in ring particles on either side.

These 'horns', like the ones shown, can be seen at the A Ring's outer edge, the Encke and Keeler Gaps (Figure 4.4) in the A Ring, the Herschel, Huygens and Laplace Gaps (and around the Laplace, Herschel, Huygens and 'Strange' ringlets (Figure 4.2)) in the Cassini Division, and around the Maxwell (Figure
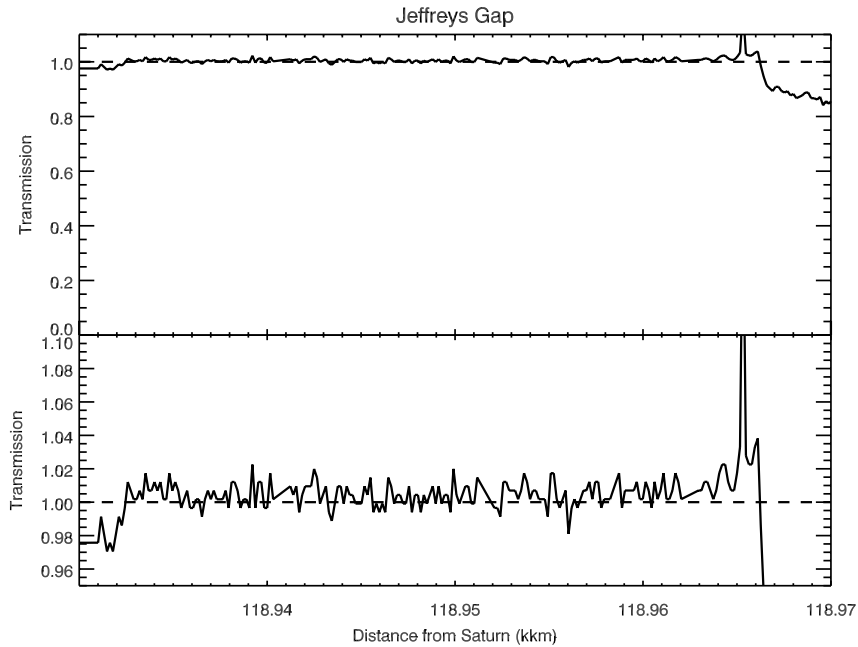
Figure 4.3: Occultation plot showing transmission through the Jeffreys Gap in the Cassini Division as a function of radius (using the Rev. 100 γ Crucis occultation), and calibrated as described in the text, with the bottom frame zoomed to better show the slight variations from full transmission. The inner edge shows no horn, while the outer edge has a 'horn' visible over the outer ~ 5 km of the gap. A probable cosmic ray near the outer edge can also be seen, making a spike in transmission.

4.1) and Titan ringlets in the C Ring. The horns have differing widths, with the ones in the A Ring extending tens of kilometers into the gap, gradually declining, while the horns in the Huygens Gap appear very 'peaky' and quickly decline by ~ 5 kilometers into the gap, as seen in Figure 4.5. Intermittent or less well shaped features can sometimes be seen in the smaller (Barnard, Bessel, Jeffreys, and Russell) gaps in the Cassini Division, the outer edge of the B Ring, and the edges of the Colombo, Maxwell and Bond Gaps, though due to small scattered signal or the narrowness of the features, these are less well resolved. g seen in Figure 4.3, showing the Jeffreys Gap: one edge shows no 'horn', while
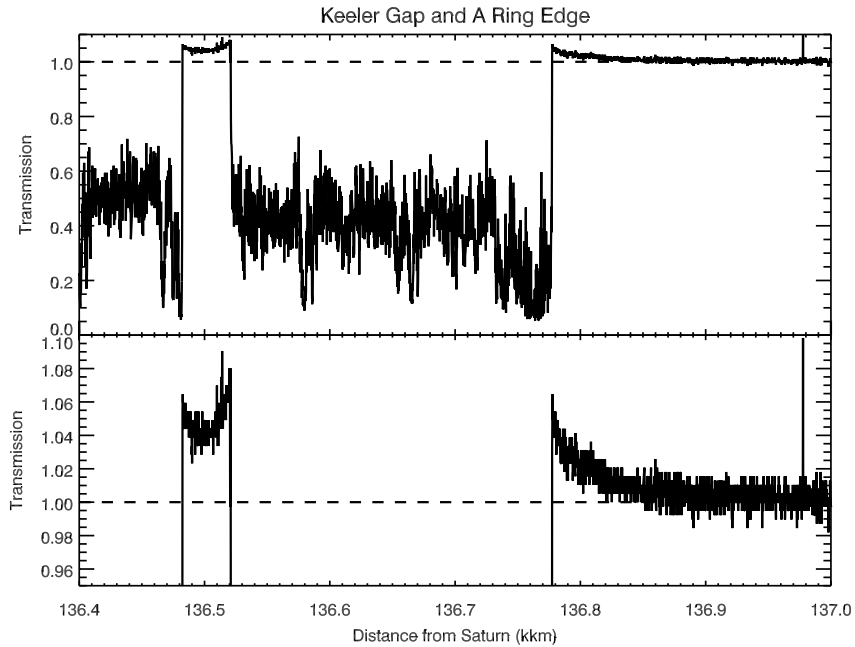
Figure 4.4: Occultation plot showing transmission the outer A Ring as a function of radius (using the Rev. 100 γ Crucis occultation), and calibrated as described in the text, with the bottom frame zoomed to better show the slight variations from full transmission. Plot is centered on the outer A Ring and shows both the Keeler Gap (left) and the A Ridge edge (right). Note the clear 'horns' at all three edges, and that the Keeler Gap is sufficiently narrow that even the middle of the gap shows an excess of light. The horn pattern in the Keeler Gap is also clearly asymmetric despite both sides of the gap being similar in optical depth, suggesting a change in particle properties on opposite sides of the gap.

the other shows a weak and relatively narrow 'horn' (and a spurious transmission spike).

These horns are caused by light scattered from ring material in the regions close to the gaps, as will be explained in the next section. The decline with distance from the edge could be caused both by less ring material contributing to the scattering (as the VIMS pixel only has an angular size of a fraction of a

104
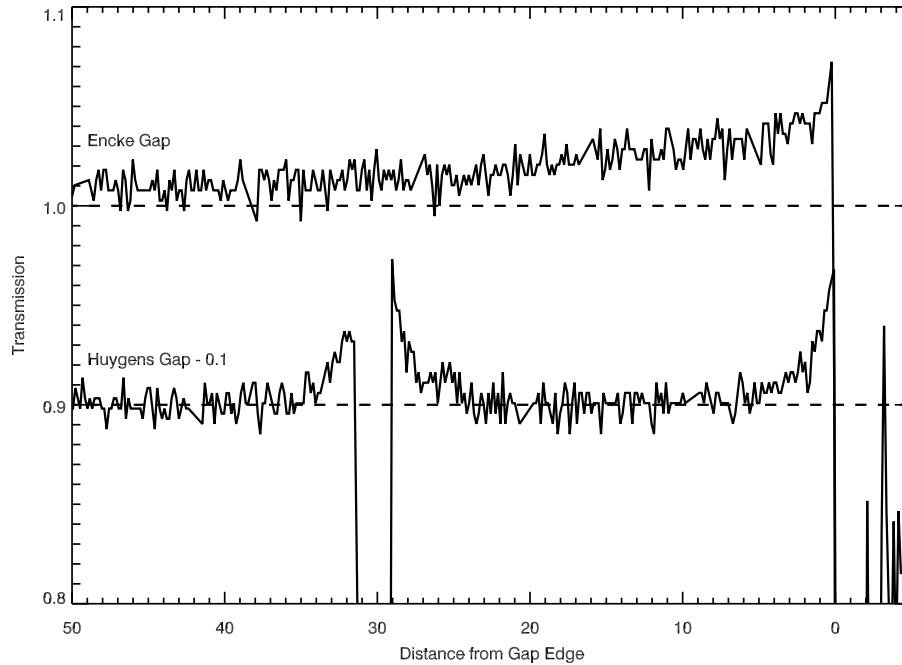
Figure 4.5: Closeup of an occultation plot showing transmission through Saturn's rings as a function of radius (using the Rev. 100 γ Crucis occultation), comparing the outer edges of the Encke (top) and Huygens (bottom) Gaps. Note that the Encke Gap's 'horn' has a gradual decline over most of the plot, while the Huygens Gap 'horn' (and that of the outer Huygens ('Strange') ringlet, both are more peaky and narrower in appearance.

milliradian), or a phase function with less scattering at large-angles. Modeling both the phase function of a population of ring particles and the scattered flux observed given the phase function and geometry of the rings as seen by Cassini will be discussed in the next section.

Astute readers may note that we observe these horns in the same gaps we use for calibrating the data. Thus, our 'unocculted' starlight, if measured too close to a ring edge, could include a small fraction of diffracted light, making it brighter than the actual unocculted star. We chose to do this because long-period drift in the 'baseline' signal (visible as slow shifts in mean DN in 'clear'

areas outside of the rings, as well as a difference between 'outside' and 'inside' (or 'ingress' and 'egress') measurements of stellar brightness) meant that a calibration well outside or inside the rings will only be useful to calibrate for the outer A Ring or inner C Ring, respectively. We attempt to minimize the amount of diffracted light inadvertently included by measuring 'baseline' levels only in the middle of the widest gaps. As the strength of the 'horns' declines with distance, the middle of wide gaps (such as the Huygens Gap between the Huygens Ringlet and the B Ring Edge, as shown in Figure 4.2), will have returned to the baseline level. We can confirm this a priori with modeling (see Section 4.3.1).

4.3 Theory

4.3.1 Scattering Theory

The intensity of diffracted light depends on the angle from the incident beam, with a characteristic scattering angle of $\theta \sim \lambda/2a$. Thus we should consider the angular scales of the problem before delving into a detailed model. The minimum angle observed is set by the sample spacing, and is on the order of a microradian. The maximum angle can be set by the smaller of the gap size or the pixel size. VIMS is operated in high-resolution mode, with rectangular pixels of 0.25 by 0.5 milliradians. Gaps in the rings can range from tens to several hundreds of kilometers. Observed from the distance of Cassini, typically half a million kilometers from the rings; this gives us angles as large as several tenths of a milliradians, comparable to the VIMS pixel size.

At 2.9 μm, microradians to tenths of miliradians correspond, by the charac-

teristic diffraction angle, $\theta \sim \lambda/2a$, to ring particle radii from several millimeters to ~ 1 meter, with the most sensitivity to centimeter- and decimeter-sized ring particles. As the ring particle-size distribution extends beyond this on the upper end (Zebker et al., 1985; French and Nicholson, 2000; Marouf et al., 2008), and on the lower end in some regions of the rings (Harbison et al., 2013), our observations most strongly constrain the slope of the particle-size distribution (or the power-law index, q) between these limits.

Figure 4.6 shows both the scale of this experiment and previous occultation work done in the infrared (red and orange shaded regions) and radio (magenta line and shaded region). The fields of view, pixel sizes and wavelength ranges of the Cassini ISS (green shaded area) are included for comparison. In this plot, particle radius (a) is on the horizontal axis, and characteristic diffraction angle (θ) on the vertical. Note that lines of equal wavelength cut diagonally from upper-left to lower right, as $\theta = \lambda/2a$.

Previous work using radio occultations, done by the Voyager and Cassini RSS teams (Zebker et al., 1985; Marouf et al., 2008), could measure ring particles from ~ 1 m to tens of meters size range (magenta shaded region), using the Doppler shift imparted by the rings to separate the scattered signal from the direct – thus, there were few limits placed on the angular resolution. Radio occultations were also used to measure the rings' differential optical depth (Zebker et al., 1985; Marouf et al., 2008), but as this is not a matter of forward-scattering, the magenta horizontal line marking the particle radii observed is near the top of the plot.

The Earth-based occultation of 28 Sgr (orange region) covered smaller particles (from ~ 1 cm to tens of meters) than the radio occultations, due to its
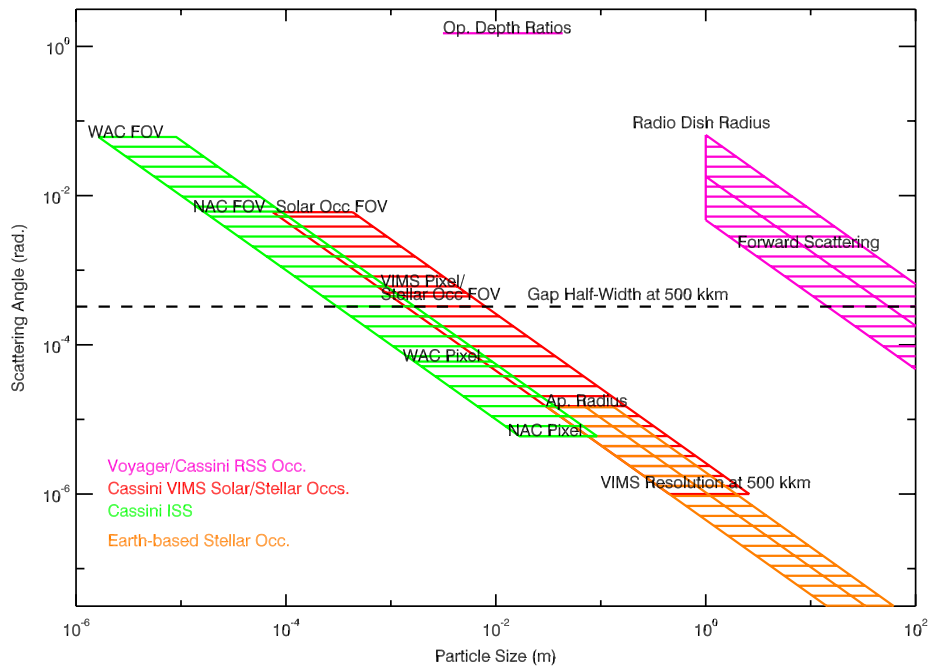
Figure 4.6: A plot of the various diffraction experiments for measuring particle size, in terms of particle radius versus characteristic scattering angle, $\theta = \lambda/2a$. In this parameter space, when plotted on a log-log plot, the characteristic diffraction angle at a given wavelength makes lines slanting from upper left to lower right. The Voyager (Zebker et al., 1985) and Cassini (Marouf et al., 2008) radio occultations; the 28 Sgr (French and Nicholson, 2000) stellar occultation and VIMS solar occultations are included, as are several angular scales relevant to this work (the angular width of a gap in the rings, and the angular distance a star moves between VIMS samples during an occultation). Finally, the scales of Cassini's Imaging Science Subsystem (ISS) field of view and pixels are included for comparison. Despite all work being in the radio and infrared, the differing angular scales cover a size range from hundreds of microns to tens of meters. See the text for more details.

shorter wavelength, despite being limited by the angular size of the aperture (3 arcseconds, or 15 micro radians) the starlight was collected in. Previous work using solar occupations observed by VIMS (Harbison et al., 2013) (upper red shaded region), though it used similar wavelengths to the 28 Sgr occultation, had a larger aperture (images were 6 miliradians across), so was sensitive to particles down to ~ 100 μm in radius. However, the VIMS pixel (and the fact the Sun is not a point source in VIMS) limited their sensitivity to particles larger than ~ 1 cm.

In this work (lower red shaded region), our 'aperture' is the VIMS pixel, making our upper limit on particle radius the same as Harbison et al.'s lower limit. The apparent angular size of the particular gap in the rings as seen from Cassini during the occultation also limits our sensitivity to small ring particles; a typical large gap (such as the Encke or Huygens Gaps) as seen by Cassini is marked with a black dashed line, and is comparable to a VIMS pixel. Our own upper limit on particle size is dependent on the angular distance the star appears to move between data points, and a typical value is set as the lower limit of the chart. While the shaded area extends to particle sizes of several meters, we would consider this an optimistic estimate, as those ring particles' scattered light would appear in only a few data-points.

To model the observed scattered light, we assume a thin homogenous ring where multiple-order scattering effects are not present, so can use the model outlined in previous work. French and Nicholson (2000) and Harbison et al. (2013) include a more detailed discussion of calculating the phase function and deriving the angle-dependent intensity, including approximations to make the problem more tractable for integration over a broad particle-size range. We will

summarize here.

Given a power-law size distribution of particles sized between a_{min} and a_{max} and differential power-law index q (i.e. $dn \propto a^{-q} \, da$), the single-scattering phase function is

$$\overline{P}(\theta) = \frac{4}{\alpha} \sin^{q-5} \theta \int_{z_{min}}^{z_{max}} z^{2-q} J_1(z)^2 \, dz \tag{4.1}$$

where $x = 2\pi a / \lambda$, $z = x \sin \theta$ and the dimensionless normalization parameter α is

$$\alpha = \begin{cases} \ln \frac{a_{max}}{a_{min}} & q = 3 \\ \frac{x_{max}^{3-q} - x_{min}^{3-q}}{3-q} & q \neq 3 \end{cases} \tag{4.2}$$

$\overline{P}$ is normalized so that $\oint \overline{P} \, d\Omega = 4\pi$. This model has singularities at $q = 2$ and 5, but given that previous work finds that $q \approx 3$ (Zebker et al., 1985; French and Nicholson, 2000; Marouf et al., 2008), that should not pose a problem. The scattered light flux in a given observation is then calculated from the phase function by the equation

$$F = F_0 \frac{\tau}{4\pi\mu} e^{-\tau/\mu} \langle \varpi_0 \rangle \int \overline{P}(\theta) \, d\Omega, \tag{4.3}$$

where F_0 is the incident flux, τ is the extinction optical depth (and typically twice the geometric optical depth for macroscopic particles), $\mu = \sin B$ (where B is the incident angle of the starlight on the rings), and $\langle \varpi_0 \rangle$ is the mean single-scattering albedo (0.5 for macroscopic particles).

Equation 4.1 is computationally expensive to integrate due to the Bessel function and the order of magnitude range between the integral's limits, and can be approximated in three angular regimes (the small, medium and large-angle

110

scattering regimes) bounded by the minimum characteristic diffraction angle, $\theta_1 = 0.5\lambda/a_{\max}$, and the maximum characteristic diffraction angle, $\theta_2 = 0.5\lambda/a_{\min}$. For the near-infrared ($\lambda \sim 3\mu$m) and particles ranging from meter-sized down to millimeters, this gives us a minimum characteristic diffraction angle in the microradians and a maximum characteristic diffraction angle in the tenths of milliradians, meaning that, unlike in the case of solar occultations (Harbison et al., 2013), medium-angle scattering will be most prominent, with possible contributions from large-angle scattering, especially if $a_{|min} \lesssim 1$ cm. small-angle scattering (i.e. $\theta < \theta_1$) may be relevant in calculating the height of the 'horns', but should not be relevant for most data.

In the medium-angle case (i.e., $\theta_1 \ll \theta \ll \theta_2$) , the dominant sources of scattered light at a given angle are those particles whose size corresponds to the characteristic diffraction angle at that radius. Approximating the integral in Equation 4.1 gives

$$\overline{P}(\theta) \approx \frac{4}{\alpha} (\sin \theta)^{q-5} \, \mathcal{J}_0^\infty (q) , \tag{4.4}$$

where $\mathcal{J}_0^\infty(q)$ is equal to the integral $\int_0^\infty z^{2-q} J_1 (z)^2 \, dz$, which is nearly constant over the range of $2 \leq q \leq 5$, except when q approaches 2 or 5. While the bounds of the particle-size distribution are included in calculating α, they have only a weak effect on the value of $\overline{P}$, provided that $q \sim 3$. q is the dominant factor defining the particle-size distribution that controls $\overline{P}$ in this size regime.

If we choose $a_{\max}$ and $a_{\min}$ based on previous studies, then only one parameter (q, the power-law index) need be fitted at each edge. This assumption should be tested in high optical depth regions (such as much of the A and B rings) where aggregates exist that would fall outside a normal power-law size distri-

bution (Salo, 1992), but for optically thin regions such as the Cassini Division or C ring, where the ring is expected to remain relatively uniform, it should be a good assumption.

In the large-angle case (i.e., $\theta > \theta_2$), the phase function is set mostly by the tails of the smallest particles' diffraction cones. Thus a_{min} (in the form of x_{min}) becomes an important term, as we can see in the approximation

$$\overline{P}(\theta) \approx \frac{4}{\pi\alpha} (\sin\theta)^{-3} \frac{x_{min}^{2-q}}{q-2}, \; \theta > \theta_2. \tag{4.5}$$

Similarly, in the small-angle case, the phase function is dominated by the largest particles with the narrowest diffraction cones, and a_{max} (or x_{max}) becomes the critical factor, as shown in

$$\overline{P}(\theta) \approx \frac{1}{\alpha} \frac{x_{max}^{5-q}}{5-q}, \; \theta < \theta_1. \tag{4.6}$$

In the case of solar occultations observed by VIMS, large-angle scattering dominates and the amount of scattering observed best constrains a_{min} (Harbison et al., 2013), whereas radio scattering experiments are in the small-angle regime and best constrain a_{max} at several meters (as the mean scattering angles are much smaller than the beam size at the centimeter wavelengths used in radio occultations).

112

4.3.2 Occultation Geometry

In order to transform a function giving the intensity of diffracted light at a given angle into a measure of the flux received by VIMS, we need to integrate over the VIMS field of view filled with ring material, all at various angles, θ, from the source star. Thus, we need to know how much of the nearby ring VIMS is seeing as its optics follow the star into the gap.

We calculated the geometry of the observations from the SPICE kernels and the reconstructed position of Cassini at the time of the observations, as described in the previous section. From this reconstruction, we know that the Cassini spacecraft is at distance r_C from the center of the planet, and inertial longitude λ_C, and latitude, B'. The star's position in the sky – specifically the star's declination relative to Saturn's equator, B, and its longitude, $\lambda_\star$ are also known. We are also able to calculate the set of radii r and longitudes λ marking the star's projected position on the ring plane, as seen by Cassini. As VIMS stellar occultations are, in part, the best constraint on the locations of ring edges and ringlets, and have revealed that some ringlets have complex non-circular behavior (Hedman et al., 2010b), we measure the position of a ring edge, r_e, based on where the transmission goes from below to above 1. This finds the local boundary of the ring material, without requiring a general model of the ring edge or ringlet's position.

We can then use a coordinate system centered on Saturn, with the planet's ring plane defining $z = 0$ (and the north pole defining the z axis) and the longitude of the star marking the positive x axis. Figure 4.7 shows the occultation geometry in this coordinate system. The star is in the direction defined by the normal vector $(\cos B, 0, \sin B)$, the spacecraft is at $(r_C \cos \phi_C \cos B', r_C \sin \phi_C \cos B',$
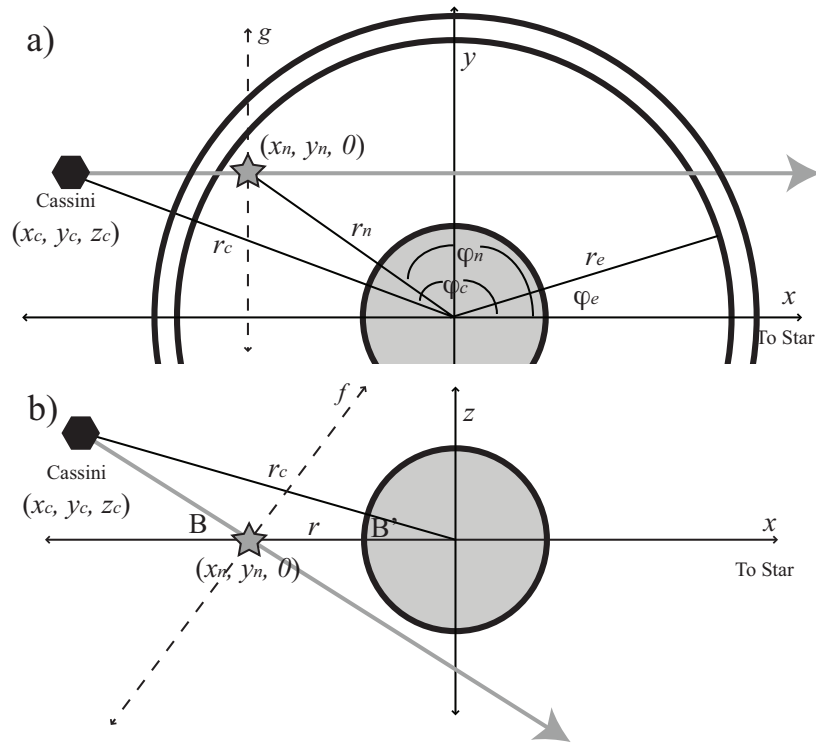
Figure 4.7: Diagram showing occultation geometry, with a top (a) and side (b) view, in a coordinate system where the ring plane defines the plane $z = 0$ (with North in the positive-z direction), and the direction to the star in that plane defines the positive-x axis. Cassini's position (black hexagon), Cassini's line of sight (gray arrow), the location where Cassini's line of sight to the star crosses the ring plane (gray star), and a ring edge (black circle in the top plot) are all marked, as are the angles defining these locations. The axes of the sky-plane coordinates to determine projected angular distances in VIMS field of view are shown as dotted lines.

$r_C \sin B'$) where ϕ_C is the longitude of Cassini relative to the star. The ring edge near the occultation track across the rings is then at $(r_e \cos \phi_e, r_e \sin \phi_e, 0)$, where ϕ_e is again measured from the stellar direction's projection into the ring plane. Even though many edges are non-circular, for such small pieces of the rings, a circular edge is a good approximation. The projected location of the star on the ring plane for each observation is then written as $(x_n, y_n, 0)$.

In order to observe the ring edge as seen by Cassini in projection, which we need to calculate angular distances from the star, we need to transform the coordinate system from the Saturnocentric one to a Cassini-centric one that will give us the view in the sky-plane, and, thus, angular positions of any point relative to any other point on Cassini's 'sky'. We assume that the star is centered in VIMS's field of view, and that the angles of interest (which are well under a milliradian) allow a 'flat' coordinate system to be used instead of a spherical one. We place the star at (0,0) in the sky 'plane', and define axes f and g such that the g axis is in the x-z plane (one with a fixed y coordinate), perpendicular to the direction towards the star, and the f axis is parallel to the y axis. In Figure 4.7, we show the new f and g axes as dashed lines (in the top frame, the f axis would be projected down to the line-of-sight to the star; in the bottom frame, the g axis would be coming straight out of the page).

Thus, the coordinate transform (a translation, then a rotation about the y/f axis by B) is

$$f \;=\; y - y_n \tag{4.7}$$

$$g \;=\; z \cos B - (x - x_n) \sin B \tag{4.8}$$

where the coordinates (x_n, y_n) mark the instantaneous stellar position projected onto the ring plane. The ring edge becomes in this coordinate system

$$f_e = r_e \sin \phi_e - r_C \sin \phi_C \cos B' \tag{4.9}$$

$$g_e = -r_e \cos \phi_e \sin B - r_C \sin B' \cos B + r_C \cos \phi_C \cos B' \sin B \tag{4.10}$$

The location of the edge closest to the origin of the $f - g$ coordinate system (or the projected location of the star on the ring plane as seen by Cassini) can be found by minimizing $\sqrt{f^2 + g^2}$ (or $\left(f^2 + g^2\right)$, which has a location in the same minimum for real values of f and g).

The derivative is

$$\frac{\partial \left(f_e^2 + g_e^2\right)}{2\partial \phi_e} = f_e \frac{\partial f_e}{\partial \phi_e} + g_e \frac{\partial g_e}{\partial \phi_e} = 0, \tag{4.11}$$

or

$$0 = 0.5 r_e \sin 2\phi_e \cos^2 B - r_n \sin \phi_n \cos \phi_e + r_n \cos \phi_n \sin \phi_e \cos B' \sin B. \tag{4.12}$$

This can be directly (if tediously) solved for ϕ_e, but it's easier to make the assumption that the difference between (r_n, ϕ_n) and (r_e, ϕ_e) is small and $r_e = r_n + \Delta r$ and $\phi_e = \phi_n + \Delta \phi$, where Δr and $\Delta \phi$ are both small ($\Delta r \ll r_e$; $\Delta \phi \ll 1$). In particular, the last assumption means that $\cos \Delta \phi \approx 1$ and $\sin \Delta \phi \approx \Delta \phi$, so the sums of angles become

$$\sin (\phi_n + \Delta \phi) = \sin \phi_n + \Delta \phi \cos \phi_n \tag{4.13}$$

116

$$\cos(\phi_n + \Delta\phi) = \cos\phi_n - \Delta\phi \sin\phi_n. \tag{4.14}$$

The coordinates of the edge near the star then become

$$f_e = r_n\Delta\phi \cos\phi_n + \Delta r \sin\phi_n \tag{4.15}$$

$$g_e = \sin B \left(r_n\Delta\phi \sin\phi_n - \Delta r \cos\phi_n\right). \tag{4.16}$$

From this, we learn that the minimum distance from the origin (the star) to the ring edge is

$$\rho = \frac{\Delta r \sin B}{\sqrt{\cos^2\phi_n + \sin^2 B \sin^2\phi_n}} \tag{4.17}$$

The angle ρ subtends on Cassini's sky is $\theta_e \approx \rho/\Delta$, where Δ is the distance from Cassini to the observation location.

The actual Cassini VIMS pixel is a rectangle of 0.5 by 0.25 milliradians. We approximate the Cassini VIMS pixel as a circular aperture $\theta_a = 0.2$ mrad in radius, as this will take up the same area on the sky as the actual 0.5×0.25 mrad pixel. We assume that the star is located in the center of the pixel (as its exact position within the pixel is not known) and that the ring edge is a linear feature that can be parameterized in the polar (θ-ψ) coordinate system as $\theta \sin\psi = \theta_e$. If we integrate the scattering function over the pixel, we should return the expected flux measured for a given set of ring properties. Equation 4.3 becomes

$$F = F_0\frac{\tau}{4\pi\mu}e^{-\tau/\mu} \int_0^\pi \int_{\theta_e/\sin\psi}^{\theta_a} \langle\varpi_0\rangle \overline{P}(\theta)\,\theta\,\mathrm{d}\theta\,\mathrm{d}\psi \tag{4.18}$$

117

which we can evaluate by the methods mentioned Section 4.3.1, assuming that the scattering properties of the ring are uniform over the VIMS aperture. Should we wish to include multiple edges in our model, the scattered flux from each edge may be summed. If we wish to model a ringlet with a finite width (two edges at r_1 and r_2), we can calculate two minimum angles, θ_{e1} and θ_{e2}, and describe the ringlet as bounded by $\theta \sin \psi = \theta_{e1}$ and $\theta \sin \psi = \theta_{e2}$, and integrate over the area filled by ringlet material. In fact, mathematically this is equivalent to the difference between two integrals: thus, if r_1 is the near edge and r_2 the far edge to the star, the flux from the ringlet is the same as the flux from a ring located at r_1 and beyond minus the flux from a ring located at r_2 and beyond.

4.4   Computation

Now that we have a model for the flux observed at each point in the light curve (Equation 4.18), based on parameters of a given particle-size model ($a_{\min}$, $a_{\max}$, q, τ) and the measured locations of rings or ringlets, we can produce a model of transmission versus radius and then find the best fit to the data. Tests of the model show roughly what we should expect when fitting the data.

A simple test of particle size is shown in Figure 4.8, where, instead of the full model, a uniform distribution of particles of a single size is used. The effect of having a sheet of material, rather than material at a single location changes the function shape from the $(J_0 z/z)^2$ of a single spherical ring particle, and smooths over the peaks and troughs of the Bessel function. As expected, the larger the particles, the narrower the 'horns' of the transmission. The effect of the aperture we chose is also visible here; the 3-mm radius particles are diffracting a fair

118
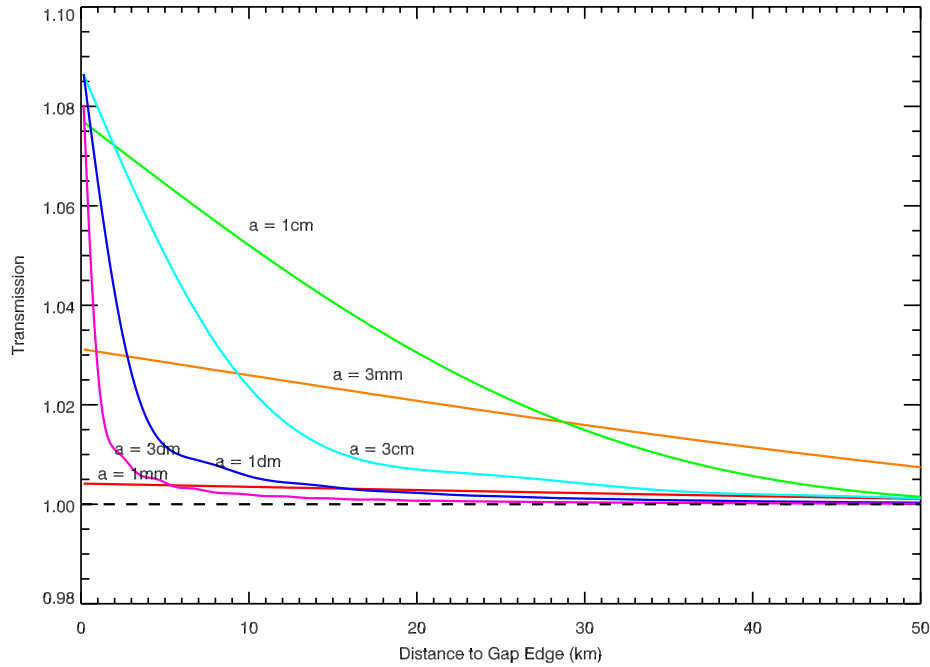
Figure 4.8: Plot of transmission (at $\lambda = 2.9\mu$m) versus distance from a ring
edge when Cassini is 500,000 km away, for a ring with $\tau/\mu = 1$
and made of uniform particles of a given radius, from $a = 1$
mm (red) to $a = 3$ dm (magenta). As expected, larger parti-
cles produce a narrower 'horn' around the gap, as they cannot
scatter light far from the ring edge. There is also a transition
between 3 mm and 1 cm sized particles when the diffraction
cone becomes smaller than the model's aperture ($\theta = 0.2$ milli-
radians is 100 km projected on the ring plane here); the shape
of the horn becomes more 'peaky' as less scattered light is lost
near the ring edge.

amount of light outside the aperture, while particles of 1 cm and bigger are
diffracting nearly all starlight within the VIMS aperture.

In Figure 4.9, we test the full model, using a fixed a_{min}, a_{max} and τ, and a
varying q. Steepening the power-law index places more small particles into
the ring relative to big particles, and having a similar effect as decreasing the
particle size did in Figure 4.8 – the horns get broader and less 'peaky'.
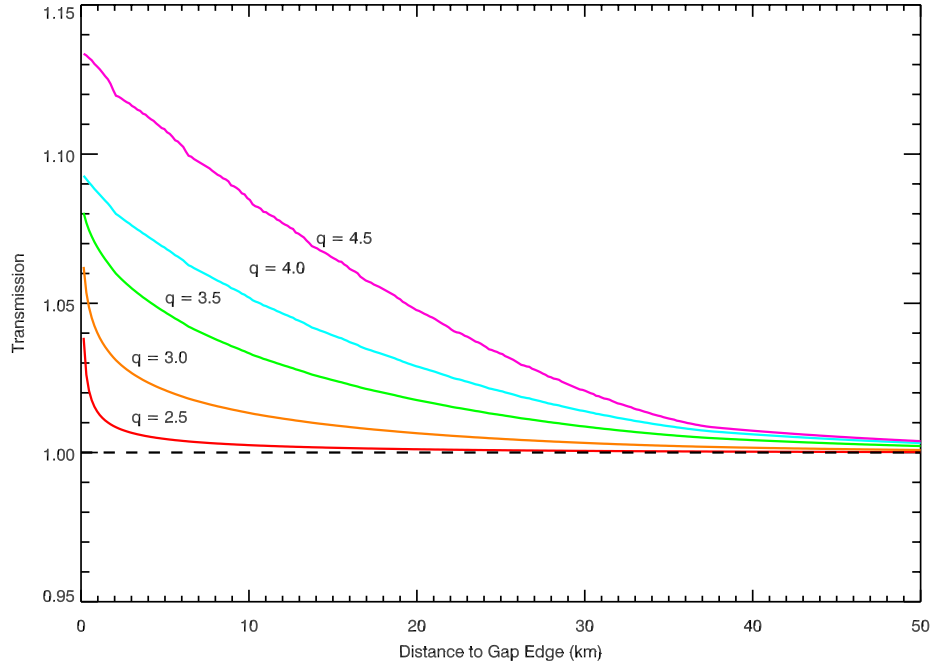
Figure 4.9: Plot of transmission versus distance from a ring edge when Cassini is 500,000 km away, for a ringlet with $\tau/\mu = 1$ and particle radii ranging from $5\,\text{mm} \leq a \leq 10\,\text{m}$ with a power-law index (q) from 2.5 (red) to 4.5 (magenta). A steeper power-law index produces a wider, less peaky horn than a shallow one. We do not see the simple θ^{q-5} dependence (distance corresponds to angle from the gap edge) from Equation 4.4 because of the changing area of 'optically active' ring material as the angular distance between the star and the edge of the ring increases.

We test our ringlet geometry model in Figure 4.10, using a fixed optical depth and particle-size distribution, but changing our semi-infinite ring to a ringlet of a finite width. To first order, this acts as a scaling parameter on the 'horns': narrower ringlets contain less material than broad ones, and have smaller horns. Beyond about 50-100 km, increasing ringlet width has no effect on the diffraction seen; at that point, the angular distance between the far edge and the star is too great to affect the diffraction seen in the gap. This also sets the limit of what region of the rings this technique can sample for all gaps.
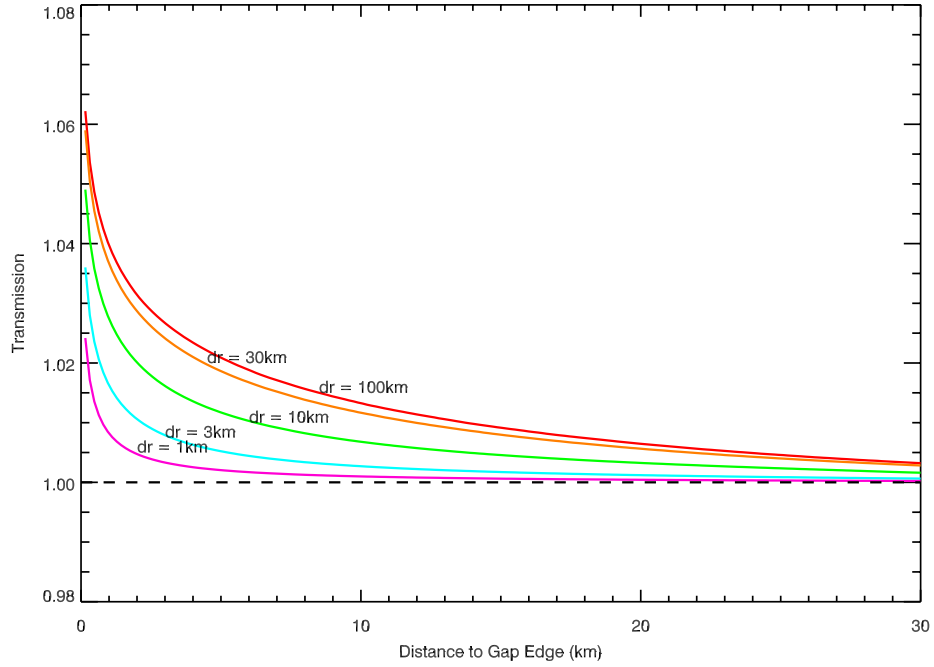
Figure 4.10: Plot of transmission versus distance from the near ring edge when Cassini is 500,000 km away, for a ringlet with $\tau/\mu = 1$ and particle radii ranging from 5 mm $\leq a \leq$ 10 m, a power-law index (q) of 3.0, and a width ranging from 1km to 100km. Narrow ringlets produce less scattering due to less area covered, despite having the same particle distribution and surface density. Ring material further than 100 km from the edge falls outside the VIMS aperture even when the star is at the edge and does not influence the diffraction horn; a 100 km wide ringlet is effectively the same as a semi-infinite ring. This also identifies the limit of what is sampled by the model.

As we begin to fit our model to data, we must chose which parameters to fix and which to leave free. Because, as shown in Figure 4.6, our technique is limited to ring particles that are less than about a meter, and previous studies (Zebker et al., 1985; French and Nicholson, 2000; Marouf et al., 2008) show an effective upper cutoff in the particle size-distribution of 5 to 20 m, we choose to fix $a_{\max} = 10$ m at all edges. Our models, as shown in Figure 4.9, indicate that the power-law index q strongly affects the observed signal, so q is fitted for all

edges.

The effect of $a_{\min}$ is less clear. Since much of the scattered light is lost from the VIMS aperture, the model is relatively insensitive to $a_{\min} < 1$ cm, as tested by Figure 4.8's weak horns for particles smaller than 1 cm. Previous studies (Harbison et al., 2013) suggest a particle size cutoff in the millimeter regime for the C and A Rings, so, for the moment, we choose to fix $a_{\min} = 5$ mm. However, in Section 4.6, we will re-examine that assumption.

Finally, we can directly measure τ in broad regions of the rings, so for outer and inner edges of gaps, τ is fixed at an extinction optical depth calculated by measuring the observed optical depth and taking twice its value (note our previous discussion on the difference between extinction and geometric optical depths). For ringlets, especially narrow ones, the measured τ may not be the true geometric optical depth or representative of a ringlet with a complex optical depth profile, so it is left as a free parameter. In addition, due to the Herschel Ringlet's complicated optical depth profile, it was modeled as two adjacent ringlets. Gaps that have dusty ringlets, like the Encke Gap, were not modeled in the occultations where these azimuthally-variable features are clearly visible.

The measured error in the data, σ, was calculated based on the observed point-to-point variation of starlight outside of the ring, leading to a χ^2 statistic of

$$\chi^2 = \frac{1}{\sigma^2} \sum (T_{obs.}(r) - T_{model}(r))^2 , \tag{4.19}$$

where $T_{model}(r)$ is the transmission calculated at each observation point, given

the ring geometry, optical depth, and particle-size distribution model parameters, and $T_{obs}(r)$ is the observed transmission profile. The sum is taken over the entire gap for purposes of finding the best fit model; however, this calculation for χ^2 may be too low for wide gaps (where observations near the middle of the gap may contain little scattered light, such that $T_{obs.} \approx 1$ for many models).

Cosmic ray hits, which can produce a single pixel 'spike' in the transmission, were removed from the set of observations to be fit by identifying all data points that were more than 5σ away from an initial 'guess' model and were *not* close to a gap or ringlet. This leaves some smaller cosmic rays that could affect the fitting procedure, but are difficult to distinguish from an actual relatively steep 'horn', but does remove the worst offenders. We also did not account for baseline wander – variations in the baseline level of the star due to motion in the field of view. As we do not use all gaps for normalization (as many gaps are not narrow enough to be confident that any part is clear of scattered light), there is the possibility that the 'actual' baseline is smaller or larger than the value we chosen. However, we do measure baselines from within the ring region we are studying (inside the C Ring and the Maxwell Gap (as far from the edges and ringlet as possible) for C Ring gaps; between the Huygens Ringlet and outer edge of the B ring and between the Laplace Ringlet and inner edge of the Laplace Gap for Cassini Division gaps, and beyond the A Ring for outer A ring gaps). We also can observe the baseline outside the rings for significant wander on these distance scales (from our baseline measurements to the gaps in question) and avoid using occultations where such can be seen.

For gaps with dense ringlets (the Huygens, Herschel, Laplace, Maxwell and Colombo gaps), the routine MPFIT (Markwardt, 2009) was used to minimize the

χ^2 of a fit by adjusting qs for each edge and ringlet and τ for each ringlet. For gaps without ringlets (the Encke, Keeler, Jeffreys, Russell, Barnard, Bessel, and Dawes gaps and the outer edge of the A Ring), MPFIT proved intractable and would return the input q without modification. Given the limited number of parameters and the lack of a complicated phase-space, the q for each edge was found by assuming a single minimum in χ^2 in the parameter space and using a downhill method to search over the one- or two-dimensional parameter space of $2.2 \leq q \leq 4.8$.

The Bond and Kuiper Gaps were not fit, due to the relative narrowness of these gaps. The Jeffreys, Russell, Barnard and Bessel gaps were not always fit; the goodness of fit of the best models for the Huygens, Herschel and Laplace Gaps was used as a barometer for the quality of the data in the Cassini Division, and only the higher quality data had all gaps (excluding the Kuiper, as mentioned previously) fit.

Thus, we fit the following variations of our model to the corresponding edges:

- A single parameter (q) model for the A Ring's outer edge.

- A two-parameter model (q_{in}, q_{out}) model for the Encke, Keeler, Jeffreys, Russell, Barnard, Bessel, and Dawes gaps.

- A four-parameter model (q_{in}, q_{out}, $q_{ringlet}$, $\tau_{ringlet}$) for the Colombo, Maxwell, and Laplace gaps.

- A six-parameter model (q_{in}, q_{out}, $q_{ringlet1}$, $\tau_{ringlet1}$, $q_{ringlet2}$, $\tau_{ringlet2}$) for the Huygens and Herschel Gaps (the Herschel Ringlet was treated as two adjacent ringlets).

4.5 Initial Results

4.5.1 A Ring

The edges used in the A Ring are those of the Encke and Keeler Gaps and the outer edge of the A ring, giving a total of five radial samples of the power-law index, q. Because gaps are only present in the outer regions of the A ring, the inner and middle A ring are unfortunately not sampled. The A Ring was well covered by occultations, enough that we chose to consider only those occultations with $\sin|B| \geq 2/3$. This limit was chosen due to possible effects of the A Ring's self-gravity wakes, linear aggregates of ring material tens of meters in scale that invalidate our assumption of a homogenous ring (Salo, 1992). These wakes have two effects: they complicate the calculation of the optical depth, and they introduce an additional effect based on the longitude of the observation geometry (Colwell et al., 2006; Hedman et al., 2007c). These geometric effects are minimized for very open occultations, where the wake orientation has less effect.

Examples of fits to A Ring edges are shown in Figures 4.11 and 4.12. As can be seen in these two figures, the 'horns', within the gaps are quite well described by the model when the correct parameters are found.

The mean values of the best-fit q found in each occultation for both edges of the Encke gap and the inner edge of the Keeler Gap are shown in Figure 4.13 and listed in Table 4.1. These fits are consistent with a similar distribution of particles near all three edges, suggesting that the trans-Encke region and the region immediately interior to the Encke Gap are similar. The Voyager RSS models
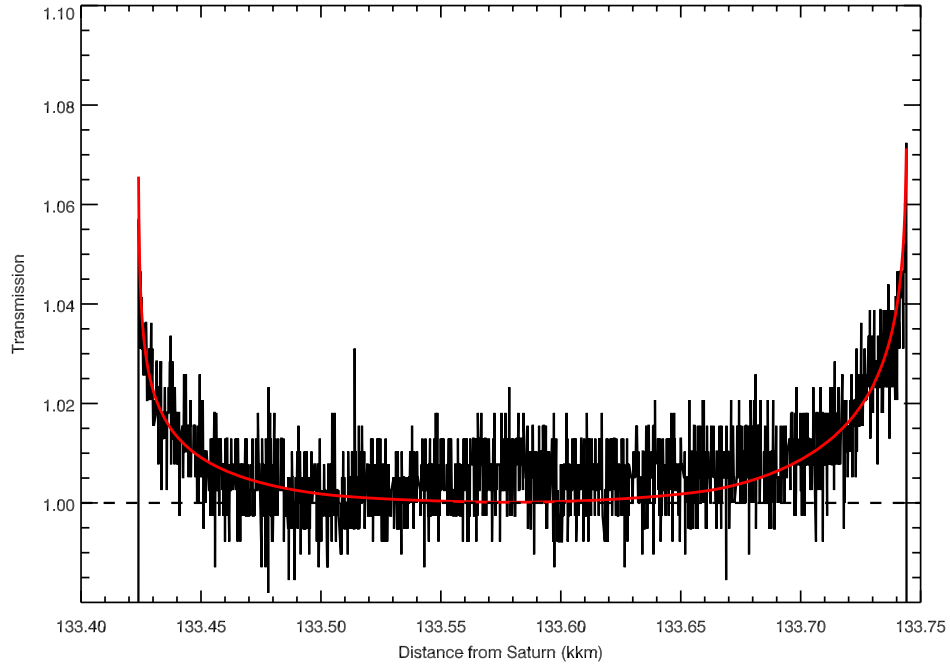
Figure 4.11: Occultation plot centered on the Encke Gap (in the outer A Ring), showing transmission as a function of radius (black line) using the Rev. 100 γ Crucis occultation, and calibrated as described in the text, with the best-fit model (plotted in red). We fixed a_{max} = 10 m and a_{min} = 5 mm and fitted q at each edge.

Edge/Ringlet	q	# Fits
A OER	3.48 ± 0.12	8
Kee OEG	3.47 ± 0.03	10
Kee IEG	2.97 ± 0.05	10
Enc OEG	3.02 ± 0.06	4
Enc IEG	2.89 ± 0.04	4

Table 4.1: Mean best-fit power-law index for A Ring gap edges, assuming a particle-size distribution from 5 mm to 10 m. The number of occultations used to calculate the mean is listed; occultations that were poorly fitted (χ^2 > 2 per degree of freedom) or were at shallow inclination angles $|\sin B|$ < 2/3 were not included in the means. Edges are labeled with IEG (inner edge of gap), OEG (outer edge of gap) and OER (outer edge of ring).
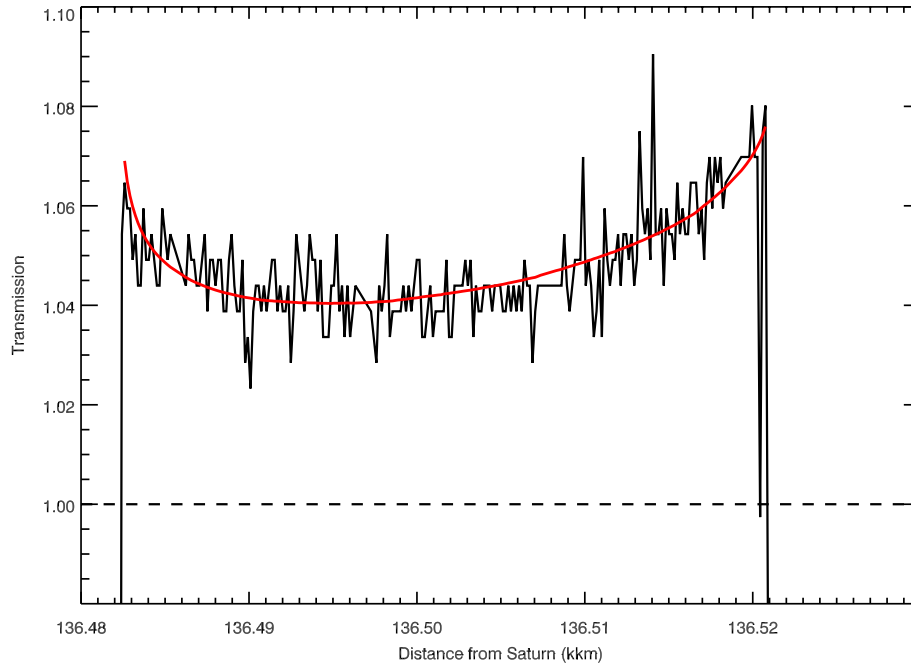
Figure 4.12: Occultation plot centered on the Keeler Gap (in the outer A Ring), showing transmission as a function of radius (black line) using the Rev. 100 γ Crucis occultation, and calibrated as described in the text, with the best-fit model (plotted in red). We fixed $a_{max} = 10$ m and $a_{min} = 5$ mm and fitted q at each edge. The difference in power-law index on either side of the gap is visible as asymmetry in both the data and model, and even the middle of this narrow gap shows transmission greater than unity.

(Zebker et al., 1985) show a trend of increasing power-law index with radius, but the measurements of the trans-Encke region and the region immediately interior to the Encke gap are consistent with the corresponding gap edges. The 28 Sgr models (French and Nicholson, 2000) of the outer A Ring (outside the Encke Gap) are slightly too shallow ($q = 2.9$) to agree with our models.

The trans-Keeler region was too narrow to be sampled by previous experiments, though there is photometric (Dones et al., 1993) and spectroscopic (Nicholson et al., 2008) evidence that it is distinct from the rest of the A Ring, and
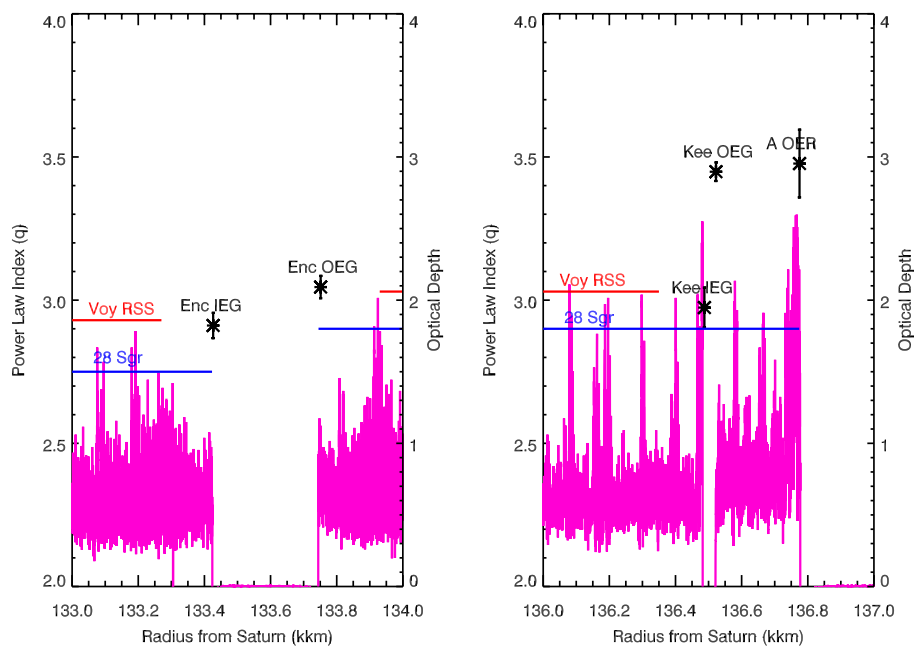
Figure 4.13: Mean modeled power-law index of the A ring gaps and the edge of the A ring, plotted versus mean radius of the gap edges. Error bars are the 1σ scatter from the ensemble of model results. Gaps are labeled with IEG (inner edge of gap), OEG (outer edge of gap) and OER (outer edge of ring). Results from the Voyager RSS (red line (Zebker et al., 1985)) and 28 Sgr (blue line (French and Nicholson, 2000)) occultations are included for comparison. Each panel covers a radial range of 1000 km. An optical depth profile (derived from the Rev. 100 γ Crucis occultation) of the outer A Ring (magenta line, with axis on right) is included to show positions of edges and the relative optical depth of the ring.

from the neighboring region between the Encke and Keeler Gaps. The asymmetry between the particle size-distribution in trans-Keeler and neighboring regions is even seen clearly in the data, such as in Figure 4.12. Our models show a remarkably steep power-law index for the outer edge of the Keeler Gap and the outer edge of the A Ring, clearly distinguishing this region from the rest of the A Ring edges studied.

The self gravity wakes make modeling this region difficult, as they violate the assumption of a homogenous ring, especially at low inclination angles where azimuthal variability becomes important. However, Lewis and Stewart (2005) predicted that regular passes by the embedded satellites Pan and Daphnis would disrupt self-gravity wakes near the Keeler and Encke Gaps, exactly the regions we are studying, making this small region of the A Ring less aggregated and well-modeled without including the effects of wakes.

Introducing self-gravity wakes affects the number of ring particles interacting with starlight. In a homogenous ring, the optical depth can be simply converted to the fraction of filled cross-sectional area of the ring, which then can be used to normalize a size distribution. However, in a wake-filled ring, some of the absorption is due to opaque wakes made of ring particle aggregates, with the remaining due to individual ring particles in the unresolved 'gaps' between the wakes. Thus the measured optical depth is greater than the effective optical depth that contributes the diffracted flux, by an amount that depends on wake properties and observational geometry.

In our model of the A Ring edges, we do not fit for the optical depth of free particles, so if our optical depth is incorrect, we will see the effects in q, the only free parameter, or in a larger χ^2, or both. Using Equation 4.3, we see that optical depth should primarily be a scaling factor of the excess transmission, rather than affecting the shape. The distribution of scattered light reaches a maximum at $\tau/\mu = 1$, with lower and higher optical depths producing less scattering. Using a value of τ closer to μ than actually exists in the interwake regions would cause the model to produce bigger horns, which would lead to fitting a shallower power-law index than exists to bring the horns back down to

those observed; the reverse would happen if a smaller optical depth was input. Either way, the shape of the horns would be incorrect, resulting in a poorer fit.

As a test, we ran fits of the Keeler Gap using a self-gravity wake model derived from Hedman et al. (2007c), as adapted for the solar occultation model in Harbison et al. (2013). Wake widths and heights were taken from Nicholson and Hedman (2010), allowing us to calculate the optical depth of interwake particles based on the ring transmission we measured. As expected, this lowered the optical depth in free particles able to diffract starlight at angles we can measure, as approximately 30% of the ring area illuminated was covered in opaque wakes too large to diffract light at these angles. Unlike the situation faced by Harbison et al. (2013), the occultations resulted in very little difference in azimuth. As expected for a dense ring ($\tau \gtrsim 1$), including self-gravity wakes steepened the power-law distribution index even further to 4.17 ± 0.11 on the inner edge of the Keeler Gap and 4.29 ± 0.08 on the outer edge of the Keeler Gap). While some occultations are better fit by a model with wakes, other occultations were only poorly-fit. The net effect seems to be that adding wakes produces no overall improvement in our model fits.

Given Lewis and Stewart's theories of wake disruption (2005), it may be that the time since Daphnis's last close approach may be a hidden factor in this: the more time since Daphnis's gravity perturbed the region, the more time self-gravity wakes have to reform. However, given that the wakeless model produces a tight constraint on the power-law index across the occultations measured, and describes the data well overall, adding wakes to our model, especially at higher incidence angles, does not appear to be necessary to describe the ring particle-size distribution. This may even extend to the edge of the A

Ring, which also is well fit without including the effects of wakes, though it is not mentioned in Lewis and Stewart's work.

4.5.2   Cassini Division and B Ring Edge
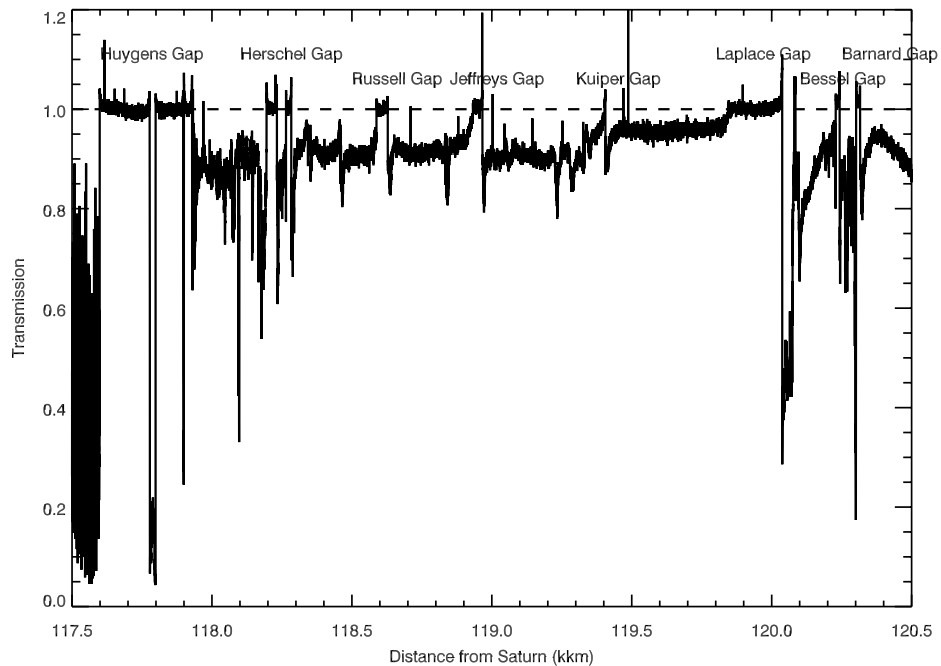
Figure 4.14: Diagram showing the named gaps of the Cassini Division, from the Huygens Gap at the inner edge of the Cassini Division to the Barnard and Bessel Gaps right before the Cassini Division ramp (not shown) that marks the outer edge of the Cassini Division. The Herschel and Laplace Gaps have obvious ringlets named for the gaps they are located in, while the Huygens Gap has two obvious ringlets, the wide Huygens Ringlet and the narrow outer Huygens/'Strange' ringlet.

The gaps in the Cassini Division offer a broad coverage of the region from the Huygens Gap at the inner edge out to the Barnard and Bessel Gaps, as shown in the diagram in Figure 4.14. The one area sampled well by radio science, the outer Cassini Division (or the Cassini Division ramp), lacks the gaps of the rest

of this ring region; making our results complementary (but difficult to compare) with RSS models. Because of the generally low optical depths in this region, we also made an effort to include more of the low-incidence angle occultations, giving anywhere from 2 to 23 cuts with good fits to include in our analysis. Note that these low incidence angle occultation often showed diffuse ringlets in some gaps, which had to be manually removed from the χ^2 calculations.
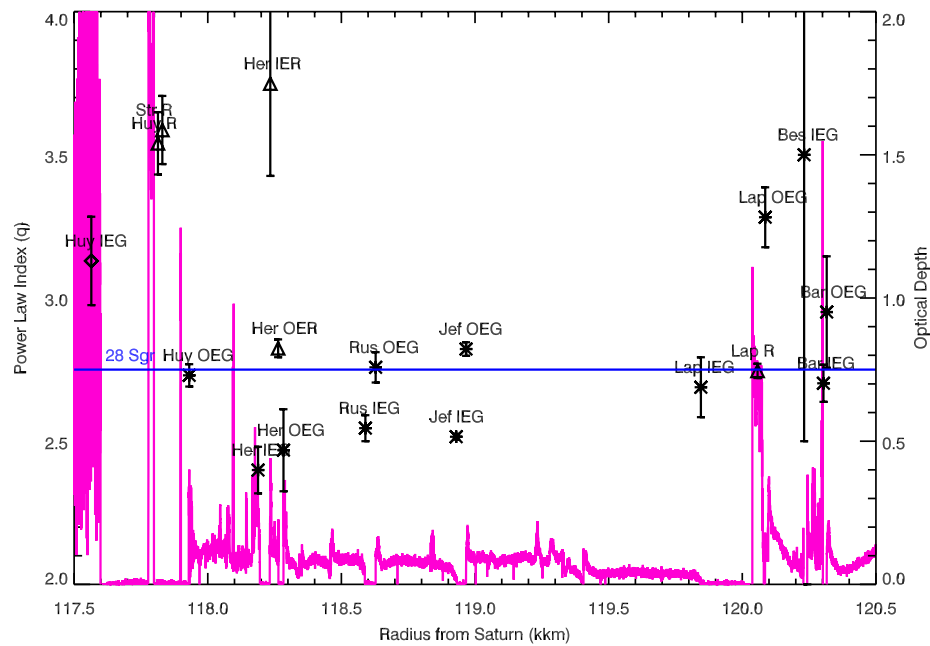
Figure 4.15: Mean modeled power-law index of the Cassini Division ring gaps, plotted versus mean radius of the gap edges. Error bars are the 1σ error from the ensemble of model results, and gap edges that failed to return multiple good (reduced χ^2 of under 2) fits are omitted. Gaps are labeled with IEG (inner edge of gap), OEG (outer edge of gap) and OER (outer edge of ring). Results from the 28 Sgr (blue line, (French and Nicholson, 2000)) occultation are included for comparison. An optical depth profile (derived from the Rev. 100 γ Crucis occultation) of the Cassini Division (magenta line, with axis on right) is included to show positions of edges and the relative optical depth of the ring.

Edge/Ringlet	q	τ (if applicable)	# Fits
Bar OEG	2.95 ± 0.19		7
Bar IEG	2.82 ± 0.07		7
Bes OEG	2.5		2
Bes IEG	3.5 ± 1.0		2
Lap OEG	3.30 ± 0.12		12
Lap Ring	2.67 ± 0.04	1.12 ± 0.07	12
Lap IEG	2.69 ± 0.10		12
Jef OEG	2.81 ± 0.02		12
Jef IEG	2.62 ± 0.07		12
Rus OEG	2.73 ± 0.05		13
Rus IEG	2.64 ± 0.08		13
Her OEG	2.47 ± 0.14		3
Her OER	2.82 ± 0.03	0.26 ± 0.01	5
Her IER	3.75 ± 0.32	0.40 ± 0.02	5
Her IEG	2.40 ± 0.08		5
Huy OEG	2.74 ± 0.04		23
Strange Ring	3.59 ± 0.12	0.66± 0.08	24
Huy Ring	3.54 ± 0.11	1.71± 0.14	24
B OER	3.13 ± 0.15		20

Table 4.2: Mean best-fit power-law index for Cassini Division gap edges and ringlets (including the outer edge of the B Ring), assuming a particle-size distribution from 5 mm to 10 m. The number of occultations used to calculate the mean is listed; occultations that were poorly fitted ($\chi^2 > 2$ per degree of freedom) were omitted. Mean fitted optical depths are listed for ringlets, though this mean does not account for any variation in optical depth between occultations. Gaps are labeled with IEG (inner edge of gap), OEG (outer edge of gap), while ringlets and rings are labeled with IER (inner edge of ringlet), OER (outer edge of ring(let)), or Ring (entire ringlet).

The inner edge of the Huygens Gap is also the outer edge of the B ring, an area of the rings agitated by the 2:1 Mimas resonance, and with complex structure visible in images (Spitale and Porco, 2010). We find that $q = 3.13 \pm 0.15$ at the outer edge of the B Ring, which is much steeper than the 28 Sgr value of 2.75 (French and Nicholson, 2000) for the entire B Ring. Removing low-inclination ($B < 30°$) occultations from the sample, to account for reduced signal to noise due to the B Ring's opacity, raises this to 3.65 ± 0.2, even farther away from the 28 Sgr value. It may be, like the trans-Keeler region, the outermost 100 km or so of the B Ring is not representative of the ring as a whole.

The extremely steep power-law indices of the Huygens Ringlet ($q = 3.54\pm 0.11$) and the outer Huygens Gap ringlet (colloquially known as the 'Strange Ringlet', and yielding $q = 3.59\pm 0.12$) are quite striking compared to the q of 2.75 reported by French and Nicholson (2000), and also seen by us for other edges, especially the outer edge of the Huygens Gap ($q = 2.74 \pm 0.04$). The Huygens Ringlet is well-separated from both gap edges, and the mean q includes a large number (24) of occultation cuts, so we have little reason to doubt these results. The Strange Ringlet, while narrower, still shows distinct horns that can be fitted. Figure 4.16 shows a sample fit of the Huygens Gap, where the Strange Ringlet has more visible horns than the model seems to reflect. This seems to hold true for many occultations.

Most of the other Cassini Division gaps and ringlets produce a value of q consistent with the French and Nicholson (2000) value of 2.75, extending from the outer edge of the Huygens Gap to at least the inner edge of the Laplace Gap and the Laplace Ringlet. The inner edge of the Herschel Ringlet is an anomaly in this region, being both steeper than average and either poorly constrained or
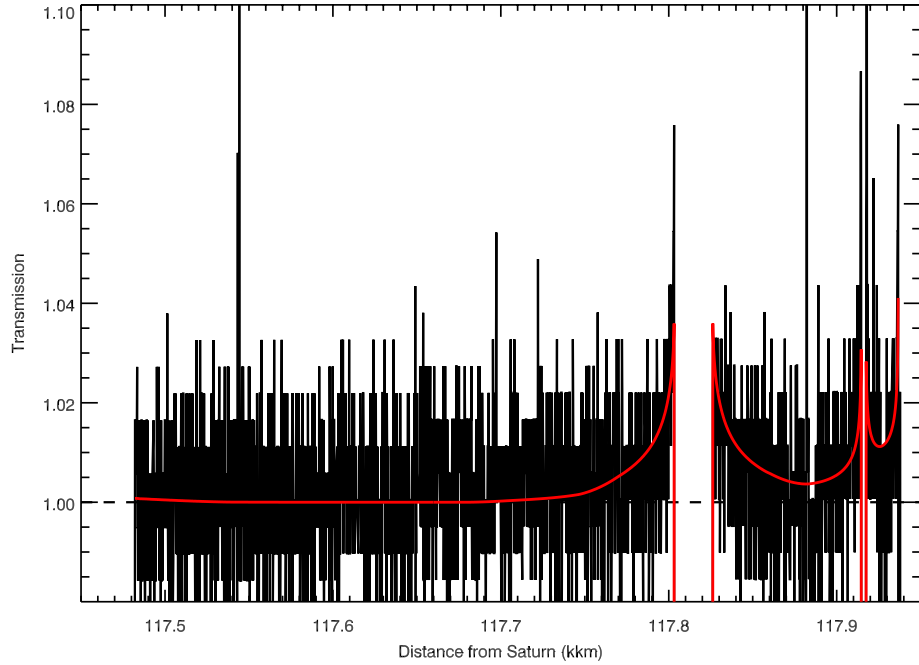
Figure 4.16: Occultation plot showing transmission through the Huygens Gap in the Cassini Division as a function of radius (black line using the Rev. 94 ϵ Muscae occultation), and calibrated as described in the text, with the best-fit model (with fixed $a_{\max} = 10$ m and $a_{\min} = 5$ mm and fitted q at each edge and fitted q and τ for each ringlet) plotted in red. In this particular occultation, the inner edge has little scattered signal to fit, unlike the γ Crucis occultation shown in Figure 4.2, but the clear effects of both ringlets can be seen.

variable. As a reminder, we chose to model the Herschel Ringlet as two separate regions, due to its distinct shape in occultations, as shown in Figure 4.17. As a result, we have parameters for the inner and outer edges. It is possible that the inner ringlet is simply too narrow to be easily modeled, or that the more complex transmission profile of the Herschel Ringlet is poorly handled by simply assuming a ringlet with two uniform steps in optical depth, or, conversely, that it could easily be handled as a simple uniform ringlet. A sample fit can be seen in Figure 4.18 where, despite the asymmetry of the ringlet's optical depth
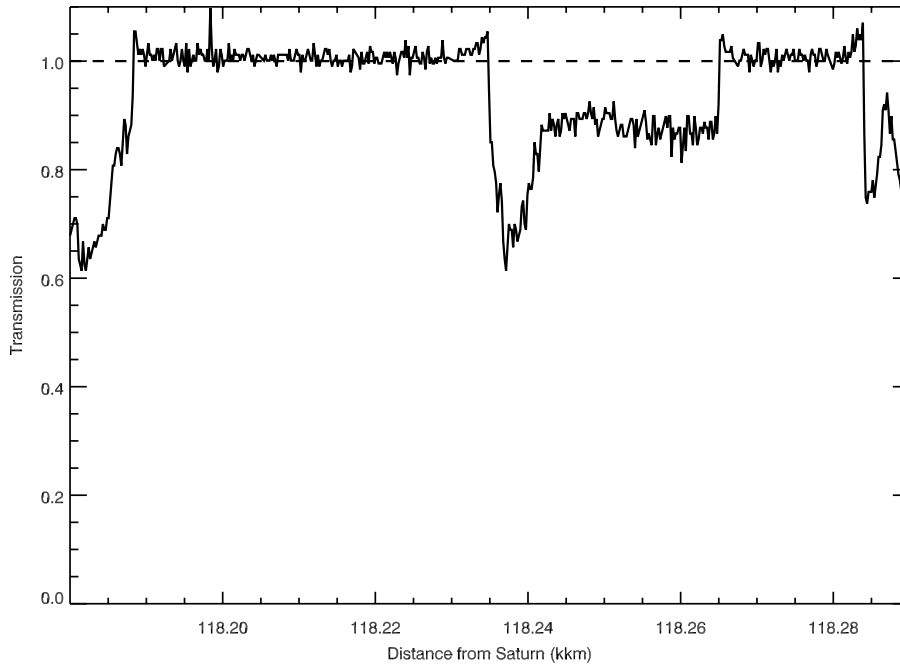
Figure 4.17: Occultation plot showing transmission through the Herschel Gap in the Cassini Division as a function of radius (black line using the Rev. 94 ϵ Muscae occultation), and calibrated as described in the text. The complex transmission profile of the Herschel Ringlet (from 118,235 to 118,265 km) is clearly visible.

profile (not shown), the horns appear mostly symmetric.

The outer edge of the Laplace Gap may have the same problem as the Herschel Ringlet's inner edge: the gap between the outer edge of the Laplace Gap and the outer edge of the Laplace Ringlet is extremely narrow, meaning the 'horn' visible from the outer edge is cut off by the ringlet and its own horns, as can be seen in in Figure 4.19. The ringlet can be constrained by its inner 'horn' which is in the broad inner part of the gap. The inner edge of the Bessel gap provides little help – it is steep, like the outer edge of the Laplace Gap, but poorly constrained as the Bessel Gap is narrow. Finally, there may be a rise to-

Figure 4.18: Occultation plot showing transmission through the Herschel Gap in the Cassini Division as a function of radius (black line using the Rev. 94 ϵ Muscae occultation), and calibrated as described in the text, with the best-fit model (with fixed $a_{max} = 10$ m and $a_{min} = 5$ mm and fitted q at each edge and two fitted qs and τs for the ringlet) plotted in red. The asymmetry of the optical depth of the Herschel Ringlet, echoed in the model, is not seen in the horns surrounding it.

wards $q = 3.0$ as seen in the outer edge of the Bessel Gap and both edges of the Barnard Gap, but this is barely significant. It is worth noting that Zebker et al. (1985) and Marouf et al. (2008) report a q of 2.75 for the Cassini Division ramp, exterior to the Barnard Gap, the same as the value reported by French and Nicholson (2000) for the entire Cassini Division, and similar to the mean seen here from the Huygens Gap to the Laplace Gap.

We also see a curious local pattern: the outer edges of the Herschel, Russell, Jeffreys, and Barnard Gaps have slightly steeper power-law indices than their

Figure 4.19: Occultation plot showing transmission through the Laplace Gap in the Cassini Division as a function of radius (black line using the Rev. 94 ϵ Muscae occultation), and calibrated as described in the text, with the best-fit model (with fixed $a_{\text{max}} = 10$ m and $a_{\text{min}} = 5$ mm and fitted q at each edge and fitted q and τ for the ringlet) plotted in red. The narrow outer region of the gap is not well fit here, or in any occultation, while the inner edge borders a mostly empty portion of the ring, so diffraction effects are weak in open occultations.

inner edges. As these Cassini Division gaps show a pattern of the inner edge being eccentric and outer edge being circular (Hedman et al., 2007c), this pattern bears further study. Bodrova et al. (2012) calculate the minimum size of free ring particles theoretically based on collisional models. Based on their modeling, in regions where inter-particle collisional velocities increase, as one would expect near an eccentric ring edge, the minimum free particle size would decrease.

While naively one would expect that adding small particles would steepen the particle-size distribution, the particles freed would be smaller than the usual

ring particles in the Cassini Division. Thus, Bodrova et al.'s model would pre-
dict no change in the power-law index of the existing particles, but a drop in
$a_{\min}$. Our modeling of the Cassini Division does not account for a changing $a_{\min}$
(but see Section 4.6), but we can look for changes indirectly by considering what
a larger or smaller $a_{\min}$ than the effective $a_{\min}$ in the ring region does to the fitted
power-law index q.

Consider the $1/\alpha$ factor in the equation for intermediate-angle scattering,
Equation 4.4. The only place $a_{\min}$ appears in this equation is buried in $1/\alpha$. A
larger $a_{\min}$ results in a larger $1/\alpha$. A larger q also results in a larger $1/\alpha$. So, if
we assume that our fitting is sensitive to the magnitude of the 'horns' (and thus,
the value of $1/\alpha$) first and the shape (set by the $\sin^{q-5}\theta$ term) second, an incorrect
value of $a_{\min}$ may change the best fit q slightly. If we make $a_{\min}$ too large, then
the best-fit q will be smaller than the one using the correct $a_{\min}$ in order to get
the same value of α. This would produce the effect observed, i.e., perturbed
edges where ring regions we expect to find smaller particles show a shallower
power-law index than unperturbed edges.

4.5.3 C Ring

The gaps in the C ring, shown in Figure 4.20 with the rest of the C Ring structure,
sample a variety of regions: the Colombo Gap (Figure 4.22) occurs in the inner
C Ring, while the Maxwell (Figure 4.24) and Dawes Gaps occur in the outer
portions of the C Ring, with the latter just interior to the C Ring ramp. Fewer
occultations are available in the C Ring, especially covering the Colombo Gap,
as most chord occultations do not pass this close to the planet. The mean power-
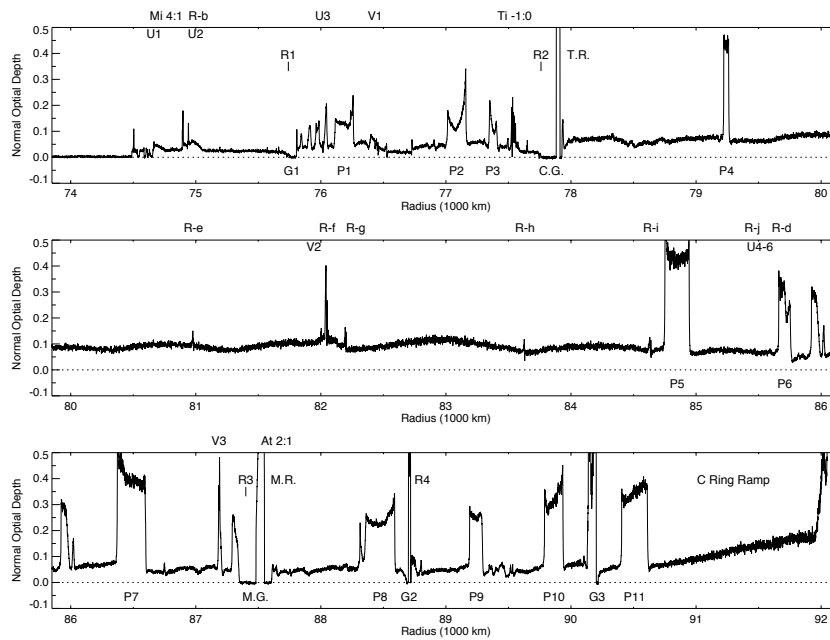
Figure 4.20: Diagram showing the named gaps of the C Ring, with the Colombo Gap (CG) in the inner C Ring, and the Maxwell (MG), Bond (G2) and Dawes (G3) Gaps just interior to the C Ring ramp in the outer C Ring. The Colombo, Maxwell and Bond Gaps all have ringlets within them.

law indices in this section are based on between six and thirteen occultations. In addition, the C Ring has a wide range of optical depths, with the majority of the ring being relatively low in optical depth, but several ringlets (the Titan and Maxwell Ringlets) being nearly opaque, as can be seen in Figure 4.20.

In addition, the gaps in the C Ring are often less sharp than those in the Cassini Division or A Ring, adding an extra source of error to our models. Both the Maxwell and Dawes Gaps have a plateau (a region of the C Ring with enhanced optical depth) directly interior to the gap edge, and the Colombo Gap has a second fuzzy ringlet (R2) almost at the edge. These structures make the C

Edge/Ringlet	q	τ (if applicable)	# Fits
Daw OEG	2.92 ± 0.11		7
Daw IEG	2.70 ± 0.08		7
Max OEG	2.71 ± 0.19		5
Max Ring	3.32 ± 0.22	3.6 ± 1.8	6
Max IEG	2.55 ± 0.11		5
Col OEG	2.81 ± 0.27		4
Col Ring	3.61 ± 0.27	5.8 ± 1.4	5
Col IEG	3.42 ± 0.32		2

Table 4.3: Mean best-fit power-law index for C Ring gap edges, assuming a particle-size distribution from 5 mm to 10 m. The number of occultations used to calculate the mean is listed; occultations that were poorly fitted ($\chi^2 > 2$ per degree of freedom) or were at shallow inclination angles $|\sin B| < 2/3$ were not included in the means. Mean fitted optical depths are listed for ringlets, though this mean does not account for any variation in optical depth between occultations. Gaps are labeled with IEG (inner edge of gap), OEG (outer edge of gap), while ringlets are labeled with Ring (entire ringlet).

Ring gaps unexpectedly challenging to fit, as the model relies on having a relatively uniform sheet of ring material, and unobstructed sampling of the light close to the gap edges – as mentioned when fitting the Laplace Gap in the previous section, a ringlet too close to an edge can cover the edge's horn pattern.

Because the best occultations for the nearly opaque ringlets are not necessarily the best for the usually far more diffuse edges of the gaps, we checked for effects of inclination on the gap edges. To check that, we split the set of occultations into two groups, 'high inclination' ($\sin B > 2/3$) and 'lower inclination' ($\sin B < 2/3$) and compared the mean best-fit q of each subsample. With the exception of the inner edge of the Colombo Gap (where limited data meant that only a single lower inclination occultation fit existed), the results appear consistent with no difference in the data. However, there does appear to be a
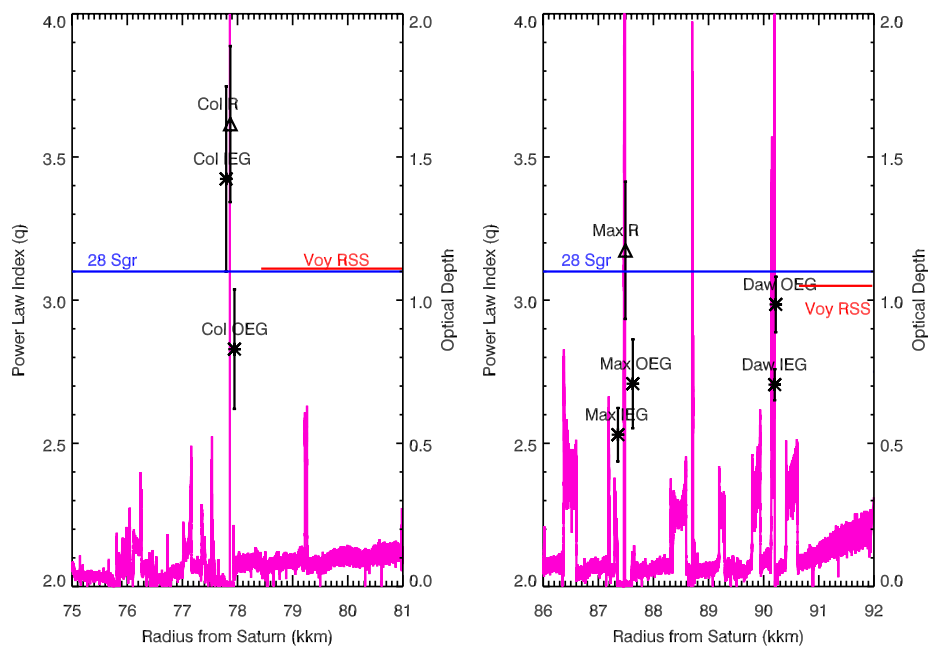
Figure 4.21: Mean modeled power-law index of the C ring gaps and the edge of the C ring, plotted versus mean radius of the gap edges. Error bars are the 1σ error from the ensemble of model results. Gaps are labeled with IEG (inner edge of gap) and OEG (outer edge of gap). Results from the Voyager RSS (red line, (Zebker et al., 1985)) and 28 Sgr (blue line, (French and Nicholson, 2000)) occultations are included for comparison. Each panel covers 5,000 km in radius. An optical depth profile (derived from the Rev. 100 γ Crucis occultation) of the C Ring (magenta line, with axis on right) is included to show positions of edges and the relative optical depth of the ring.

possible systematic trend in which those gap edges with shallower power-law indices show steeper indices with inclination, while those with steeper indices show the opposite effect.

Despite these sources of error, both edges of the Colombo Gap have a power-law index consistent with the values of $q = 3.1$ quoted for the entire C Ring in the 28 Sgr occultation (French and Nicholson, 2000) and $q = 3.11$ for the mid-
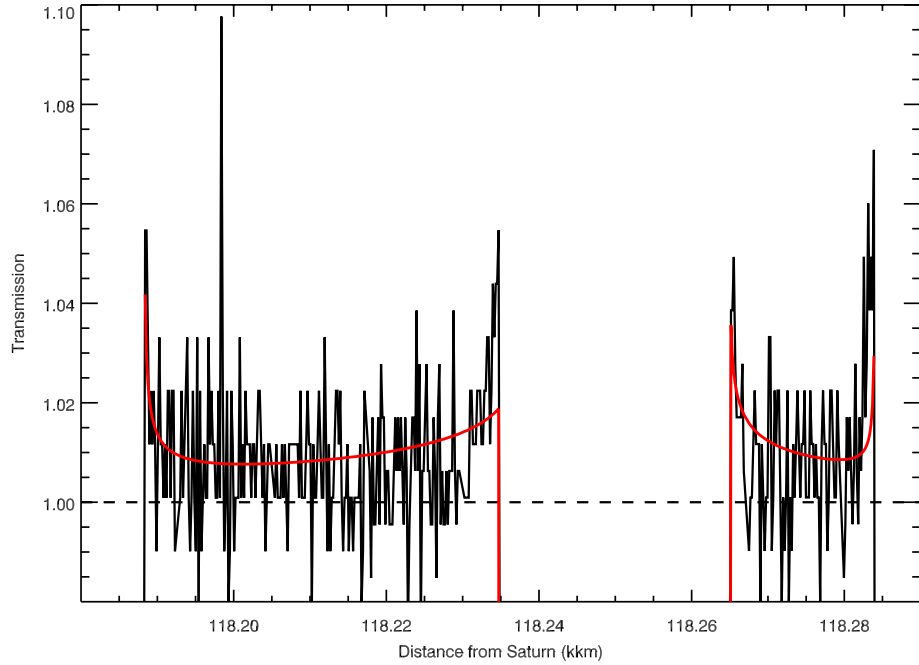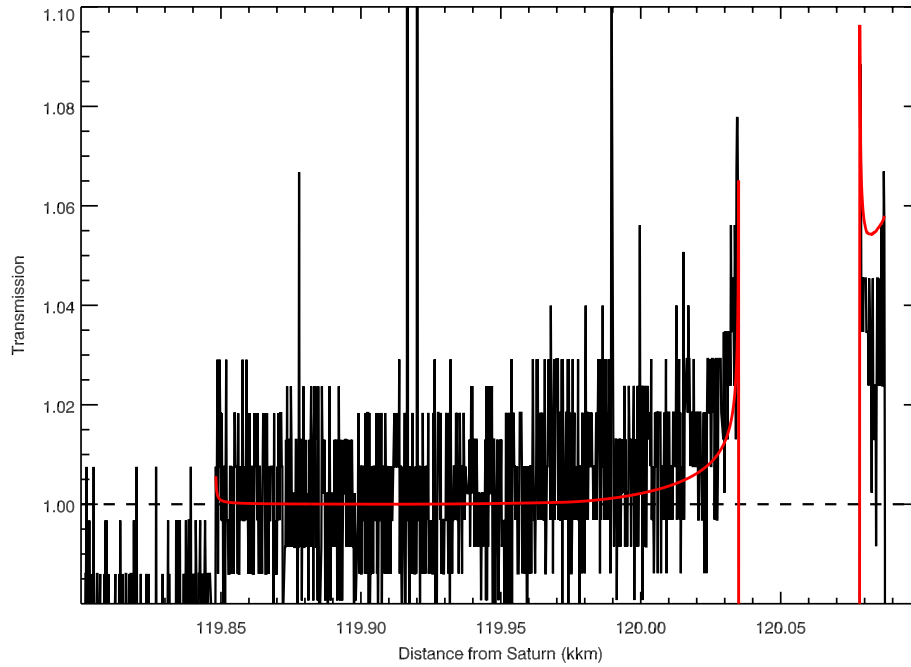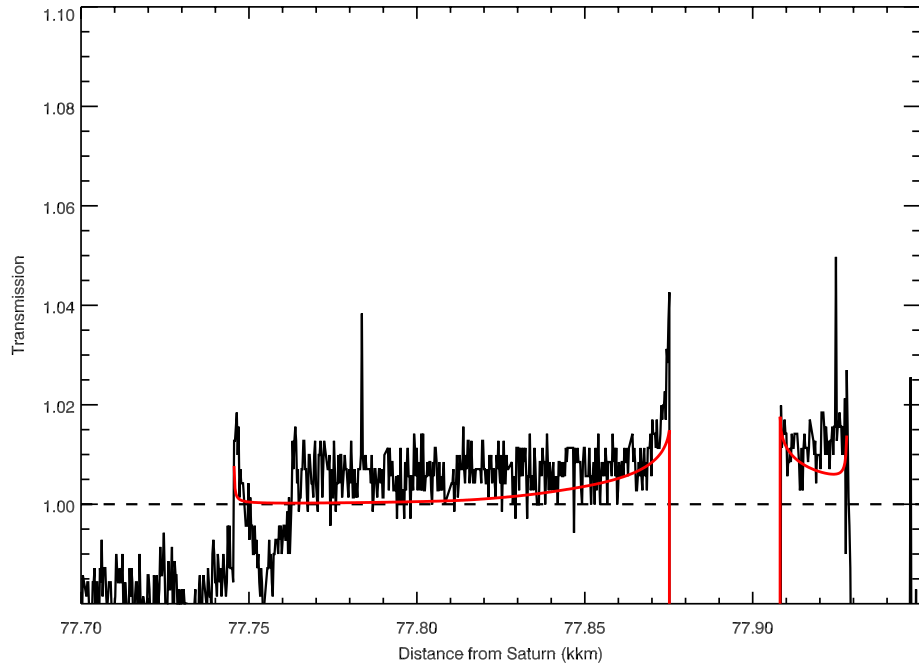
Figure 4.22: Occultation plot showing transmission through the Colombo Gap in the C Ring as a function of radius (black line using the Rev. 89 γ Crucis occultation), and calibrated as described in the text, with the best-fit model (with fixed a_{max} = 10 m and a_{min} = 5 mm and fitted q at each edge and fitted q and τ for the ringlet) plotted in red. The peculiar ringlet-like structure on the inner edge of the gap (R2 in Colwell et al. (2009)) is shown well here.

C Ring in the Voyager radio occultation (Zebker et al., 1985), albeit with large uncertainties. The Titan Ringlet in the Colombo Gap has a steeper power-law than the gap's inner edge and all but the steepest values of q reported for the C Ring in previous studies. Given the sizes on the error bars, and the unusually high τ of the Titan Ringlet, this is not a strong constraint on the average power-law index of the particle-size distribution of the inner C ring.

The Maxwell and Dawes Gaps benefited from more data and are better constrained. The power-law index of the outer edge of the Dawes Gap, q = 2.92 ±
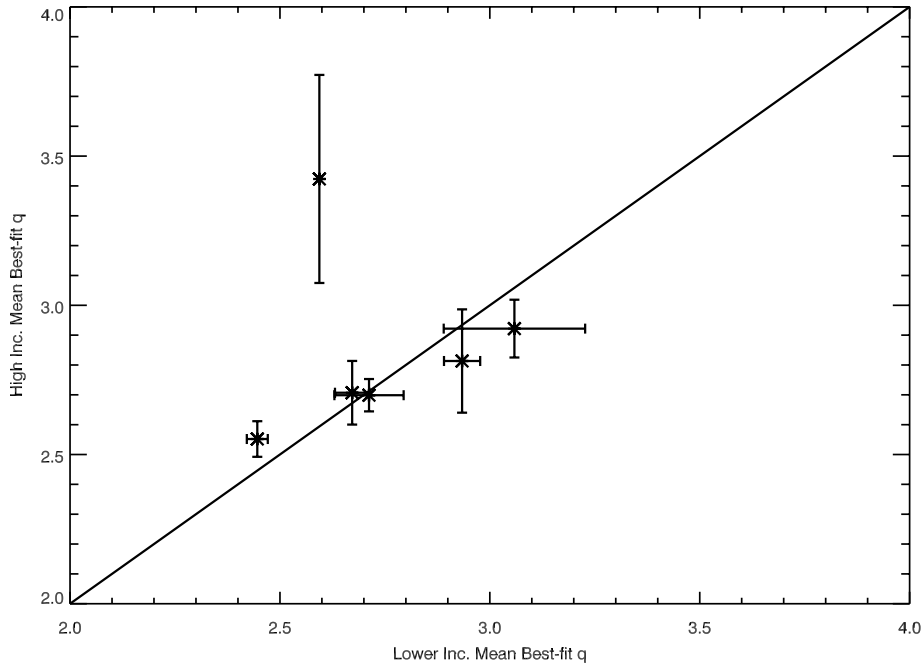
Figure 4.23: Plot of the mean best-fit power-law index for the gap edges (excluding the ringlets) of the C Ring, to check for trends with inclination of the occultation. The mean of the 'higher inclination' ($\sin B > 2/3$) subsample of occultation fits was plotted versus the 'lower inclination' subsample. Except for the inner Colombo Gap edge (which is derived from few occultations), the results are consistent with inclination of the occultation having a statistically insignificant effect on the best-fit power-law index of the edge. However, there is a slight trend that does not reach levels of statistical significance.

0.11, agrees with the Voyager RSS model of the C Ring ramp ($q = 3.05$) (Zebker et al., 1985). The Maxwell ringlet's power-law index also agrees with the 28 Sgr C Ring model value of $q = 3.1$(French and Nicholson, 2000). However, the other three gap edges (the inner Dawes Gap edge and both Maxwell Gap edges) are significantly shallower ($q = 2.55 \pm 0.11$, 2.71 ± 0.19, and 2.70 ± 0.08) than the values determined from the 28 Sgr and Voyager RSS measurements of the middle C Ring
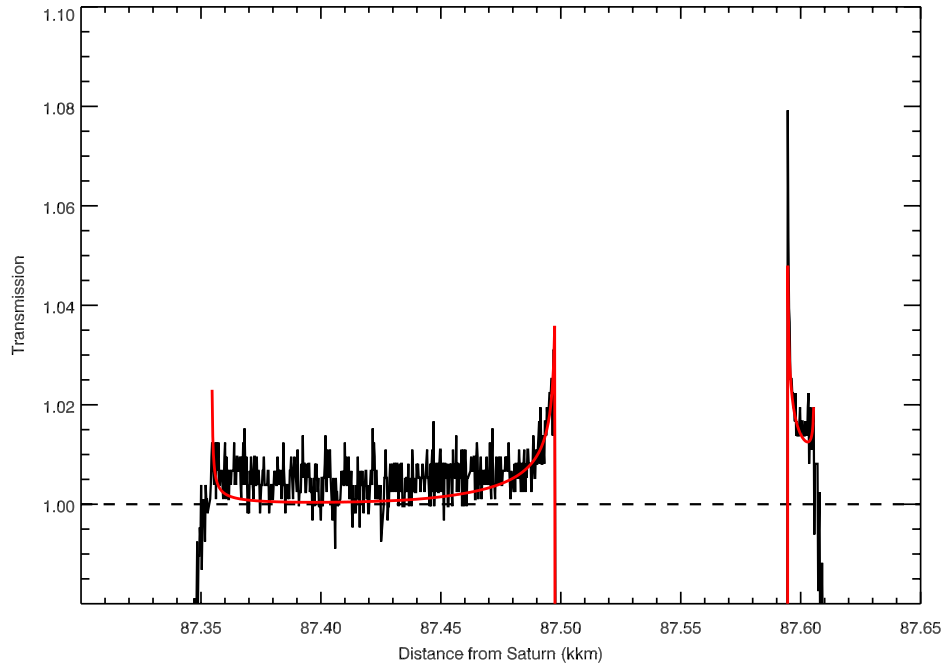
Figure 4.24: Occultation plot showing transmission through the Maxwelll
Gap in the C Ring as a function of radius (black line using the
Rev. 89 γ Crucis occultation), and calibrated as described in
the text, with the best-fit model (with fixed a_{max} = 10 m and
a_{min} = 5 mm and fitted q at each edge, and fitted q and τ for
the ringlet) plotted in red.

It could be that the C Ring ramp is different from the region directly interior
to it in particle-size distribution, just as the region is distinct in spectroscopy
and photometry (Nicholson et al., 2008), though Nicholson et al. (2008) also in-
clude the region between the Maxwell Gap and the start of the ramp itself as
part of the distinct ramp region. However, it could also suggest that, as in the
Cassini Division, the power-law is constant, but the minimum particle size is
varying: the Maxwell Ringlet is known to be eccentric and the Colombo Gap is
near a resonance with Titan, making these areas candidates for larger random
velocities, which Bodrova et al. (2012) predict would mean a smaller minimum
particle size.

145

The Maxwell and Titan Ringlets both have power-law indices steeper than the nearby gap edges. Given both ringlets are nearly opaque even in relatively steep occultations, the optical depth can be tricky to constrain. Though our model fits for optical depth of ringlets, it is possible that the optical depth and power-law index are not completely independent. A larger optical depth (when $\tau/\mu > 1.$, as is always the case in these ringlets) paired with a steeper power-law index could keep the maximum transmission of the resulting model 'horns' constant, though it would change the shape. If the horns in these ringlets are predominantly caused by the optically-thinner outer portions of the ringlets, rather than the nearly-opaque center, the optical depth that would best describe the 'horns' would be far lower than the expected optical depth given the ringlet's mean transmission (and the power-law index required to reproduce the horns, shallower). This could also be a possible explanation for the steep power-law indices of the Huygens and Strange Ringlets mentioned in the previous section. Perhaps our abilities to understand the particle-size distribution of these opaque ringlets is limited by our ability to account for their optical depth profiles.

And perhaps an equally interesting question, given the concerns that have arisen in the Cassini Division and C ring fits, would be how good our assumption is that our fits are relatively insensitive to the limits of the particle-size distribution (which justifies not fitting for the minimum particle size). We will examine this assumption in the following section.

4.6   Effects of Minimum Particle Size

In the previous section, we assume a particle-size distribution from 5 mm to 10 m. However, we have very little constraints on the minimum particle size. Pre-Cassini work (Zebker et al., 1985; French and Nicholson, 2000) could put very limited constraints on the minimum particle size of the trans-Encke A Ring and the Cassini Division as "smaller than 1 cm". Work using the Cassini RSS occultations (Marouf et al., 2008) suggests a minimum in the millimeter size regime for the trans-Encke A ring as well.

French and Nicholson (2000) report a large (30 cm) minimum size cutoff for the B Ring, while Marouf et al. (2008)'s work on the radio occultations report that for all but the inner regions of the B ring, either the power-law index is very shallow (~ 2.5) or the minimum particle size is very large ($> \sim 50$ cm). The C Ring has 'small but uncertain' values of a_{min} from pre-Cassini results (Zebker et al., 1985; French and Nicholson, 2000), while Marouf et al. (2008)'s work reports a clear minimum particle size of 4 mm and Harbison et al. (2013) reports an identical $4.1^{+3.8}_{-1.3}$ mm.

With the exception of the B ring, all the regions studied in this paper have small (less than 1 cm) cutoffs, similar to the 5 mm assumed in the previous section. However, it is worth examining our assumption that minimum particle size can be only weakly constrained, and that an assumed value does not affect the fitted power-law index, especially in light of the pattern observed in the Cassini Division's eccentric edges.

As we have mentioned previously, most of the scattering is in what we call the 'medium-angle scattering regime', where the power at a given angle is most

strongly affected by the intermediate-size particles, so the parameter that most strongly affects the phase function is q, the power-law index, and α, a composite parameter that depends on q (so also involves q). Simply put, q affects the angular distribution of diffracted light, while α only affects the amplitude. However, α also depends on $a_{\min}$ and $a_{\max}$: therefore different particle-size distributions with the same q (but different $a_{\min}$ and $a_{\max}$) can be distinguished by their differing α. This requires having not only a good determination of the amplitude of the diffracted light, but also a shape that lets us see the angular distribution. This also requires a good measurement of the effective optical depth, τ, which also affects the amplitude of the scattering.

Thus, in order to fit an $a_{\min}$ (or $a_{\max}$) to the data, or even place limits on possible $a_{\min}$, the models with similar amplitudes must have different enough shapes (relative to the noise in the data) such that the fitting routine can be distinguished between them. If all reasonable scattered-light models would be indistinguishable under even good observing conditions, all we can do is produce a single parameter defining the particle-size distribution (in this case, q) that creates the correct amount of scattered light.

For fitting $a_{\min}$, we only consider those occultation fits that have a low χ^2 and will ignore the ringlets (as there is more question of their correct optical depth). We ignore the small gaps of the Cassini Division due to a lack of data points and because they often do not show the clear 'horns' that we need, and low optical depth regions like the inner edge of the Laplace Gap. We also ignore the C Ring, due to the high scatter between different occultations in those gaps; as most of the C Ring is either low optical depth regions or the dense, nearly opaque (and, thus, with poorly-known τ) ringlets, the data are not high quality.

Some of the effect of letting $a_{\min}$ be a fitted parameter can be seen by simply finding the best fit q and the χ^2 at a ring edge in an occultation for a given minimum particle size and varying the latter systematically, effectively creating a function of q versus $a_{\min}$. This is best done at an isolated edge, as the model parameters of each side of a narrow gap may not be able to be independently fitted; the model of a gap such as the Keeler Gap has contributions from both edges.

In the case of the A Ring and B Ring, the outer edges serve nicely – the empty space between the Huygens Ringlet and the edge of the B Ring being wide enough that assumptions about the Huygens Ringlet's particle-size distribution do not influence the fitting procedure. The Encke Gap is also wide enough to serve as a test, as shown in Figure 4.11, as both edges appear independent of one another. In the Cassini Division, there are no truly wide gaps without ringlets; our compromise was to use the outer edge of the Huygens Gap and to fix the parameters of the 'Strange Ringlet' and assume this ringlet is narrow enough that the amount of light it scatters affects only a few data points. We did attempt the Keeler Gap: varying the $a_{\min}$ and q of one edge while leaving the other edge constant, but due to the lack of independence between the edges, the results should be taken with a grain of salt.

Results are presented in Table 4.4 and Figure **??**, with sample plots of the best-fit power-law index as a function of minimum particle size shown in Figures 4.25 and 4.26.

Figure 4.25 shows a typical best-fit q versus $a_{\min}$ function for the edge of a ring with $q \gtrsim 3$, in this case, the A Ring's outer edge. For edges like this, there is more total surface area in small particles per unit ring surface area than there
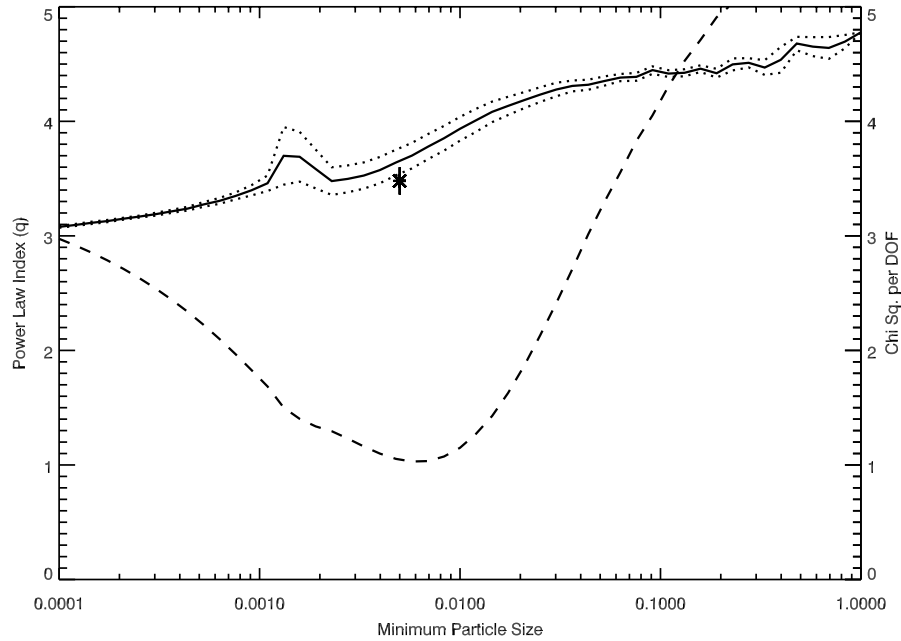
Figure 4.25: Plot of mean best fit power-law index (q) over five occulta-
tions as a function of minimum particle size at the outer A
Ring edge. Dotted lines mark the one-sigma errors to the
mean, and the starred point includes the best-fit value from
the previous section (at a fixed a_{min} = 5 mm, but for more oc-
cultations). The lower line (dashed) is the χ^2 per degree of
freedom. The bump around 1 mm is an artifact of the ap-
proximations used. Note that the χ^2 has a distinct minimum
around 6-7 mm, corresponding to a q of 3.75.

is in large particles. As a result, a small change in the minimum particle size
will produce a large change in the distribution, making it easy to distinguish
between models. We can see that a minimum which is either 'too small' or 'too
large' will increase the χ^2. The lack of small particles in the 'too large' case to
scatter light at large-angles makes the fit poorer. In the case of a too small a_{min}
however, the particle radii are small enough – as shown in Figure 4.8 – that it is
likely that light is being lost by being scattered outside the pixel, which lowers
the amplitude of the 'horns' for a given q and τ.
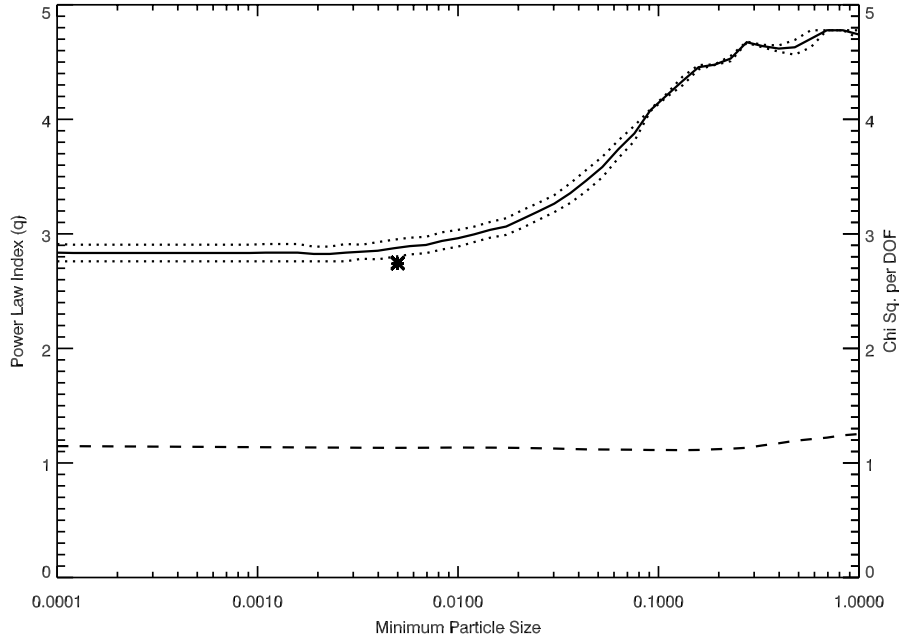
Figure 4.26: Plot of mean best fit power-law index (q) over the two cuts of the ϵ Muscae Rev. 94 occultation as a function of minimum particle size at the Huygens gap outer edge in the Cassini Division. Dotted lines mark the one-sigma errors to the mean, and the starred point includes the best-fit value from the previous section (at a fixed a_{min} = 5 mm, but for more occultations). Parameters of the two ringlets in the Huygens gap and the B Ring edge were fixed. The lower line (dashed) is the χ^2 per degree of freedom. The χ^2 shows no strong minimum, and a power-law index of ~ 2.8 produces a good fit for all minimum particle sizes smaller than 1 cm.

Figure 4.26, showing the best-fit q versus a_{min} function for the outer edge of the Huygens Gap, with a possible $q \lesssim 3$, looks quite different. The function itself still shows the upward trend expected, but it is nearly flat for a value of $a_{min} \lesssim$ 1 cm. There is more surface area in large particles per unit of surface area than in small particles. This is reflected in the parameter α, which becomes more strongly affected by a_{max} at $q < 3$. Thus the effect of a small a_{min} – light lost because it is scattered outside the pixel, lowering the amplitude of the horns

151

Edge/ Ringlet	mean q for $a_{\min}$ = 5mm	mean best-fit q for 0.1 mm $\leq a_{\min} \leq$ 1 m	mean best-fit $a_{\min}$ (mm)	No. of Occ. Cuts
A OER	3.48 ± 0.12	$3.70^{+0.15}_{-0.13}$	$5.8^{+2.6}_{-1.8}$	5
Kee OEG	3.47 ± 0.03	3.43 ± 0.06	$5.8^{+1.2}_{-1.0}$	5
Kee IEG	2.97 ± 0.05	2.94 ± 0.03	$6.9^{+1.4}_{-1.2}$	5
Enc OEG	3.02 ± 0.06	$2.96^{+0.21}_{-0.02}$	$3.3^{+8.7}_{-2.4}$	5
Enc IEG	2.89 ± 0.04	$2.90^{+0.20}_{-0.05}$	$4.8^{+12.6}_{-3.9}$	5
Huy OEG	2.74 ± 0.04	$4.33^{+0.34}_{-1.51}$	132^{+346}_{-131}	2
B OER	3.13 ± 0.15	$3.38^{+0.23}_{-0.25}$	$3.3^{+8.7}_{-2.4}$	5

Table 4.4: Values of the mean best-fit power-law index q and minimum particle size $a_{\min}$ for various edges, using a model that systematically varied $a$min from 0.1 mm to 1.0 m and found the best-fit q for each occultation cut. The values of q listed in Tables 4.1 and 4.2 are included for comparison. With the exception of the outer edge of the Huygens Gap, an assumption of $a_{\min}$ = 5 mm produced satisfactory results, though ring regions with especially steep power-law indices (such as the outer edges of the A and B Ring) are especially sensitive to $a_{\min}$.

– is minimal and we can only constrain the upper bound of $a_{\min}$ based on the amount of light at larger angles.

All the gaps in the outer A Ring, listed in Table 4.4 and plotted in Figure 4.27 roughly agrees with previous studies of the trans-Encke region (Zebker et al., 1985; French and Nicholson, 2000), producing a best-fit particle size of 3-7 mm. It should also be noted that here, the inner edge of the Encke Gap agrees more with the trans-Encke region than the varying attempts to measure the minimum particle size in the inner and mid A Ring. (French and Nicholson, 2000; Marouf et al., 2008; Harbison et al., 2013).

The Huygens Gap Edge (and the rest of the Cassini Division) does not have that strong lower constraint, and places only a weak upper constraint on $a_{\min}$. We find the best-fit value of $a_{\min}$ as $13.2^{+34.6}_{-13.1}$ cm, with a corresponding q to match. At best, we can note that the power-law index of the region outside the Huy-
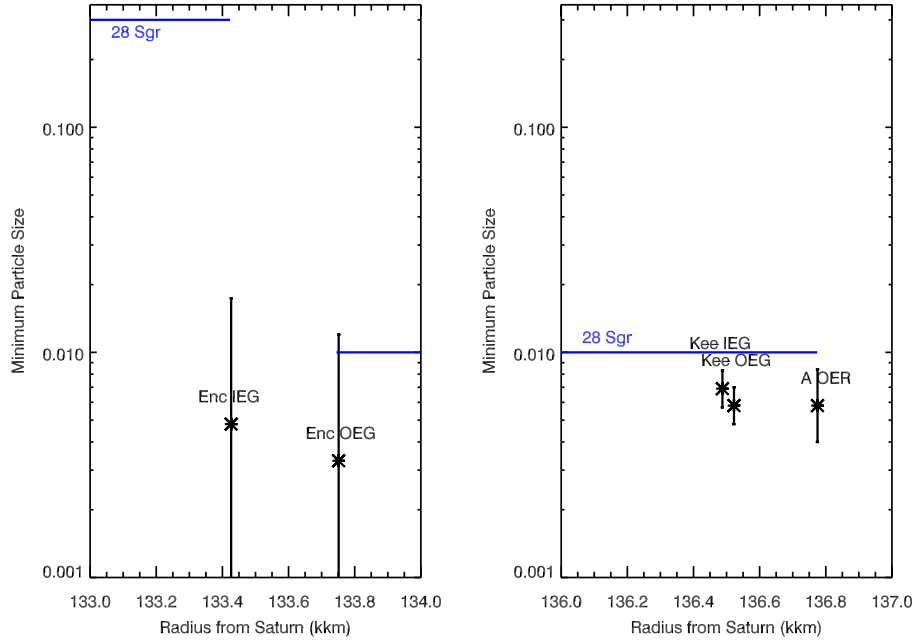
Figure 4.27: Mean modeled minimum particle size of the A ring gaps and the edge of the A ring, plotted versus mean radius of the gap edges. Error bars are the 1σ scatter from the ensemble of model results. Gaps are labeled with IEG (inner edge of gap), OEG (outer edge of gap) and OER (outer edge of ring). Results from the 28 Sgr (blue line (French and Nicholson, 2000)) occultation are included for comparison. Each panel covers a radial range of 1000 km.

gens Gap is ~ 2.8 if the minimum particle size is less than 1 cm, as French and Nicholson (2000) report, with a steeper index if the cutoff is larger.

The B Ring edge disagrees with the French and Nicholson (2000) and Marouf et al. (2008) results by around two orders of magnitude – 3mm in this work versus ~ 30 cm – but it is entirely possible that the high random velocities from the 2:1 Mimas resonance in the region could free smaller particles, making the particle-size distribution near the edge of the B Ring unrepresentative of regions of the B Ring closer in to the planet.

4.7 Conclusions

The outer A ring has a very steep (> 3.4) power-law index outside of the Keeler gap, and a shallower one (2.9 - 3.05) inside of the Keeler gap, in agreement with previous studies of this region. We also find that the trans-Encke region has ring particles that extend down to 3-7 mm in radius, slightly lower than the 1 cm reported by French and Nicholson (2000).

The Cassini Division has a shallow power-law index that makes it difficult to see where the actual particle size cutoff is; the power-law index can be as low as 2.8, consistent with previous work. The Cassini Division ringlets are problematic to fit due to their complex optical depth profiles: while the Huygens and 'Strange Ringlets' appear to have power-law indices steeper than the rest of the Cassini Division, this could also be an effect of underestimating the role the less optically-thick regions near the ringlet edge play. The B Ring edge has ring particles down to one centimeter or smaller, just as the outer A Ring does, and a steep power-law index of greater than 3, and possibly as high as 3.4. This is different from previous work done on the interior of the B Ring, and may be a result of the strong resonance creating the edge.

The C Ring is hard to fit due to low optical depth and nearly-opaque ringlets, which suffer from the same 'steeper than the neighboring ring' problem that the Huygens and 'Strange' ringlets do, suggesting a systematic problem in how we model ringlets. The power-law index of the inner region of the C Ring is roughly consistent with previous results of 3.0 to 3.1, but with large error bars of several tenths. However, the outer region just interior to the C Ring ramp (including the Maxwell and Dawes Gaps) has a shallower index of ~2.7. The outermost

C Ring power-law index value (the outer edge of the Dawes Gap) agrees quite nicely with accepted values for the neighboring C Ring ramp.

CHAPTER 5

CONCLUSIONS ON SATURNIAN RING PARTICLE SIZES

My studies of the infrared solar and stellar occultations confirmed a lot of what previous studies reveal about Saturn's rings, while presenting new data on ring regions not as well studied.
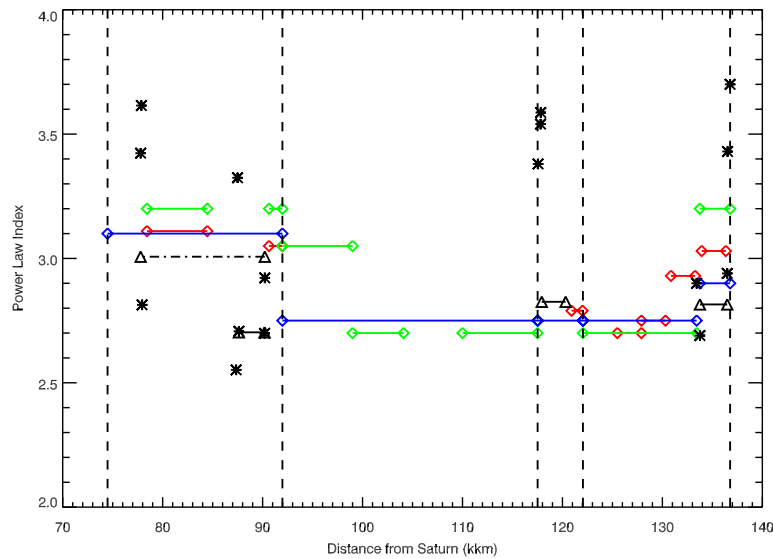
Figure 5.1: Figure 1.2, showing the ring particle power-law index versus radius from Saturn, with data from Chapter 4 added in black. Stars mark average qs for individual edges, while triangles mark averages of many edges' average qs. The region of the Cassini Division (from the outer edge of the Huygens gap to the Barnard and Bessel gaps) was averaged over, as were the region between the Maxwell and Dawes gap, and Encke and Keeler gaps for better comparisons with past data sets, and error bars were omitted. A C-Ring average is also plotted as a dot-dash line. For more details on those individual measurements, see Chapter 4.

My results indicate the C Ring has a minimum particle size of ~4mm, exactly matching Marouf et al. (2008)'s result within errors. However, my estimates of the power-law index using the edges of the Colombo, Maxwell and Dawes
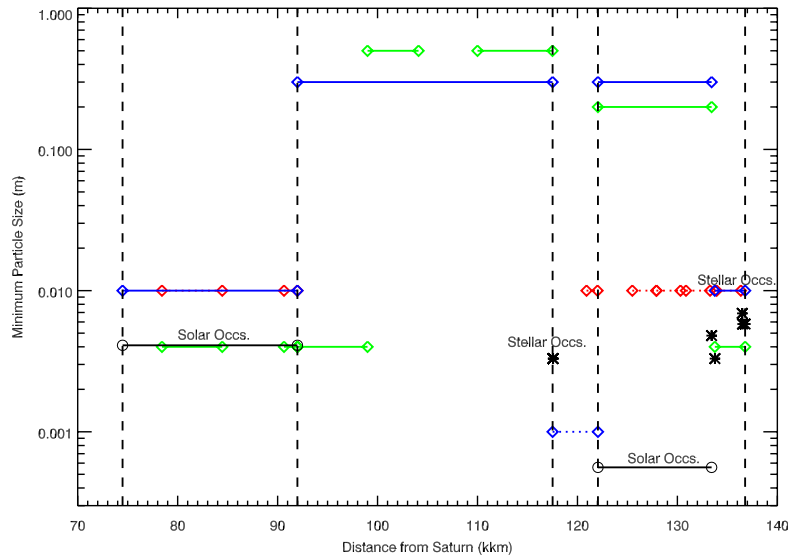
Figure 5.2: Figure 1.3, showing the minimum particle radius of the ring particle-size distribution versus radius from Saturn, with data from Chapters 3 and 4 added in black (and labeled). As strong constraints on minimum particle size were not found in Chapter 4's analysis of the Cassini Division and C Ring (but constraints on the C Ring were found in Chapter 3), values of a_{min} from stellar occultations are not plotted in those regions.

gaps, and the Titan and Maxwell ringlets are both strongly radially variable and, on average, shallower than previous work. It may be that the low optical depth of the C Ring requires more edge-on occultations than I studied to better characterize the low optical depth regions without such large error bars.

My work on the Cassini Division was able to replicate French and Nicholson (2000)'s power-law index across the region containing gaps, as well as point to the ringlets as potential deviations from this particle-size index. My work also showed a systematic trend in the fitted power-law index that might be an artifact of dynamical interactions within the ring. Sadly, I was unable to answer the question as to the Cassini Division's smallest particles: the region is too narrow to study using solar occultations and the shallow power-law index makes

constraints from stellar occultations weak. I did affirm French and Nicholson (2000)'s result that the Cassini Division, like the C Ring and outer portions of the A Ring, likely holds centimeter sized particles. I also showed that the outer hundred kilometers of the B Ring may be quite different from other regions studied, having a power-law index greater than 3, and a minimum particle size that is smaller than the 20 to 30 centimeters reported by French and Nicholson (2000) and Marouf et al. (2008).

For the A Ring, the solar-occultation data produced the startling discovery of particles down to a fraction of a millimeter in radius, contradicting work in the radio (Marouf et al., 2008) and French and Nicholson's (2000) near-infrared occultation study, which set a minimum particle size of well above 10 cm. In truth, the amount of scattered light I observed during A Ring solar occultations was difficult to explain with the middle A Ring's shallow power-law index as measured by these studies. I was the first to include self-gravity wakes within my occultation models, accounting for extra sources of opacity beyond absorption by single ring particles, as well as to show that this modeling could reproduce the amount of scattered light seen in the inner and mid A Ring, but a model including wakes was not necessary to replicate the Cassini-based stellar occultation data in the outer A Ring. I confirmed the result from previous studies (Zebker et al., 1985; French and Nicholson, 2000; Marouf et al., 2008) that the trans-Encke region of the A Ring is distinct from the inner and mid A ring, in having many centimeter-sized particles and a steeper power-law index. Furthermore, I was able to focus on the narrow trans-Keeler region, showing that it has an even steeper power-law index than the region between the Encke and Keeler Gaps.

The apparent inconsistency between my and previous work (French and Nicholson, 2000; Marouf et al., 2008) deserves further comment and perhaps additional studies. Measuring the smallest particles within the A Ring is already a difficult problem because the observed power law is shallow enough that relatively little surface area would be in these smaller particles. Thus, any study would expect to see a small signal. French and Nicholson (2000) were limited to a lower particle-size limit by the width of the ring features used and by their photometric aperture size (3 arc second). They could only model smaller particles by using large amounts of radial data or by finding light removed from the beam. While larger ring particles' scattered light showed up in the relative sharpness of small-scale optical depth features, the smallest particles' detection depended on knowing exactly how much light was scattered outside the aperture. In addition, in the A Ring, French and Nicholson (2000) suffered from a problem of their 'reference' optical depth being incompatible with the 28 Sgr data without using an ad hoc scaling factor. Marouf et al. (2008)'s work, likewise, is most sensitive to those ring particles that cover the most surface area in the rings at sizes of several millimeters to around ten centimeters. While using three bands permits the minimum particle size and power-law index to be disentangled (with eventual direct inversion of the signal to better anchor the size distribution at the large end), these two parameters are not totally non-degenerate in differential optical depth space. Shallow power laws tend to have very little differential optical depth at the 0.9 and 3.6 cm wavelengths the Cassini RSS uses, regardless of the minimum particle size.

Both works could be improved by incorporating self gravity wakes into the models. While the Voyager PPS occultation French and Nicholson (2000) use as their optical depth reference to compare the 28 Sgr occultation data against is

close in geometry, it is not identical. In addition, while the incidence angles are closely matched, the relative longitudes were not, and it was not known at the time that the rings were not azimuthally symmetric. The fudge factor of 0.9 that French and Nicholson (2000) use to align the geometric optical depths obtained from the 28 Sgr and Voyager PPS could be replaced by the expected difference in transmission due to wake geometry. If this factor were lower, then that would indicate that the 28 Sgr data had more light scattered over relatively wide angles, which would imply smaller ring particles (or a steeper size distribution, or both).

Looking at the occultation geometries (the δ Sco occultation was presented in Showalter and Nicholson (1990), and the 28 Sgr occultation was presented in French et al. (1993)), the δ Sco occurred at a slightly higher inclination ($B = 28.7°$ versus $B = 25.4°$ for 28 Sgr), but farther from the longitude where the wakes appear most 'open'. A less considered effect is that the normal optical depth no longer can be found by simply multiplying the observed optical depth by $\sin B$, as the wake visibility is also dependent on incidence angle. Using the Hedman et al. (2007c) model, and assuming wake properties of $H/\lambda = 0.1$, $W/\lambda = 0.5$, $\tau_G = 0.4$ (in extinction), which are typical for the A Ring, I find that the potential ratio between the 'normal' optical depth measured from the δ Sco and 28 Sgr occultations (ignoring wakes) would be between 0.88 and 1.01 depending on the longitudes of the ring observed, with my best estimate as approximately 0.91. This is nicely comparable in magnitude to French and Nicholson's ad hoc assumption of 0.9, suggesting an explanation for their mysterious fudge factor, but a difference of only a few percent in estimates of the geometric optical depth of the A ring in this geometry would lead to differences in the particle-size distribution model that best fit the observations.

In addition, both French and Nicholson (2000) and Marouf et al. (2008) assume they can calculate the factor n_0 in the size distribution by simply requiring that the size distribution be such that the total surface area obscured by all particles be the geometric optical depth. When one introduces self-gravity wakes, that is simply not the case – the transmission is a weighted average of the essentially-opaque weights, and the partially-opaque inter-wake regions containing the free ring particles. However, only the free ring particles would be observed as scattering light in the 28 Sgr occultation or producing a difference in optical depth between 0.9 and 3.6 cm in radio-science experiments. For a given set of parameters – a power-law index and minimum and maximum particle size – a model where part of the geometric optical depth is derived from giant aggregates like self-gravity wakes will have fewer free-floating centimeter-sized particles (and, thus, less signal of their presence, be that signal scattered light at the correct angles or differential optical depth at the correct wavelengths) than a model that assumes a homogenous ring. Thus, one would expect a model that lacked self-gravity wakes to yield a larger minimum particle size than one that did have them, which is exactly what we see comparing the results of French and Nicholson (2000) and Marouf et al. (2008) to this work.

The downside to the self-gravity wake model is that it requires additional parameters to either specify the size and orientation of the wakes (to correctly predict their orientation at a given viewing geometry) or the optical depth of the gaps between the wakes. Thus, none of our studies of the particle-size distribution can be done completely independently; most require some use of outside data – or at least outside analysis of the same data, as the best parameters of the self-gravity wakes come from Cassini stellar occultations – to constrain parameters that are weakly constrained in a given data set.

Because the A ring has strong self-gravity wakes with effects visible in many, many Cassini and Earth-based data sets, I favor using a self-gravity wake model unless it can be shown to make no difference from a simpler model or it proves to be inappropriate (as it did when it could not reproduce scattered light at the edges of the Encke Gap). Thus, future occultation-based analysis of the particle-size distribution should include a self-gravity wake model as a standard element of modeling the optical depth in the rings.

APPENDIX A

PHASE FUNCTIONS: ORIGINALLY AN APPENDIX TO "THE SMALLEST PARTICLES IN SATURN'S A AND C RINGS"

For a single-size particle distribution, the forward-scattering, or diffraction, phase function for light scattered at an angle θ is given by (Liou, 1980)

$$P(\theta) = \left[\frac{2J_1(z)}{\sin \theta} \right]^2, \tag{A.1}$$

where we introduce the dimensionless variable $z = 2\pi a \sin \theta / \lambda$, a being the radius of the particles and λ being the wavelength observed. $J_1(z)$ is the first-order Bessel function of the first kind. Integrating Equation A.1 over a truncated power law distribution of particle sizes, $dn/da = n_0 (a/a_0)^{-q}$, where $a_{\min} \leq a \leq a_{\max}$ and n_0 and a_0 are constants that can be folded into the value of τ, we find

$$\overline{P}(\theta) = \frac{4}{\alpha} \sin^{q-5} \theta \int_{z_{\min}}^{z_{\max}} z^{2-q} J_1(z)^2 \, dz, \tag{A.2}$$

where

$$\alpha = \begin{cases} \ln \frac{a_{\max}}{a_{\min}} & \text{for} q = 3 \\ \frac{x_{\max}^{3-q} - x_{\min}^{3-q}}{3-q} & \text{for} q \neq 3 \end{cases} \tag{A.3}$$

The usual dimensionless size parameter x is defined by $x = 2\pi a/\lambda$, with subscripts denoting the limiting values of a.

The mean phase function (Equation A.2) can be conveniently approximated in different limiting cases, as the full function can be computationally expensive to integrate. The limiting cases are set by the relevant angles in the problem,

which are determined by the ratio of particle size to wavelength (as quantified by x). Let the minimum characteristic diffraction angle – the angle where the largest particles will be diffracting light – be $\theta_1 = \pi x_{\text{max}}^{-1}$. Similarly, we define the maximum characteristic diffraction angle (where the smallest particles will be diffracting light) as $\theta_2 = \pi x_{\text{min}}^{-1}$.

Two angles give us three cases to consider, but only two are of real interest in this case. Small-angle diffraction – where the angles we observe at are all smaller than θ_1 – isn't relevant here, as the upper boundary of the ring particle size-distribution in the A and C Rings extends to 5m in radius (Zebker et al., 1985), and at near infrared wavelengths (0.9 to 5.2 μm), this corresponds to a θ_1 of tenths of microradians. Thus we either have a case of medium-angle diffraction (the angles we observe are between θ_1 and θ_2) or large-angle diffraction (all angles observed are larger than θ_2).

The value of θ_2 is unknown, because the minimum particle size is the quantity we are trying to measure. Given that the size of one VIMS pixel – and coincidentally the solar radius at 9 AU – is 0.5 milliradians on the sky, our data will be most sensitive to diffraction by particles with $x \lesssim 6000$, or, at 2 microns wavelength, particle sizes of 2 millimeters or less. Barring a much-lower-than-expected minimum size cutoff, the large-angle scattering case will be most relevant, though we will include the medium-angle case in our calculations to account for the possibility of free-floating particles from ~100 μm to ~2 millimeters.

For the large-angle case, (i.e., $\theta \gg \theta_2$), all particles are scattering most of their light at angles smaller than those we can measure. Thus the bounds on the integral of Equation A.2 are both much larger than unity. We can then use the

approximation $J_1(z) \approx \sqrt{2/\pi z}\cos(z - 3\pi/4)$, giving

$$\overline{P}(\theta) \approx \frac{4}{\pi\alpha}(\sin\theta)^{-3}\frac{x_{min}^{2-q} - x_{max}^{2-q}}{q-2}. \tag{A.4}$$

Because the particle-size distribution is very broad (remember we're dealing with particles with radii from millimeters to meters in size), we also know that $x_{max} \gg x_{min}$, and both are very large. So, a further approximation is to drop the x_{max}^{2-q} term (which will be very small as long as $q > 2$), which leaves the simpler expression

$$\overline{P}(\theta) \approx \frac{4}{\pi\alpha}(\sin\theta)^{-3}\frac{x_{min}^{2-q}}{q-2}. \tag{A.5}$$

In the case of medium-angle diffraction (i.e., $\theta_1 \ll \theta \ll \theta_2$), we again use a broad particle-size distribution to approximate a phase function. Because of this distribution and an angle (θ) that is between the minimum and maximum characteristic diffraction angle, we are mostly sampling light neither from the smallest nor the largest particles, but from medium-sized ring particles those have that characteristic diffraction angles. Because θ is much smaller than the maximum (θ_2), we can assume that $z_{min} = \pi\sin\theta/\theta_2$ is much less than unity, and because θ is much larger than the minimum (θ_1), we can assume that $z_{max} = \pi\sin\theta/\theta_1$ is much greater than unity. We can then approximate the integral in Equation A.2, as covering the full range of positive values of z, from zero to infinity, as most of the power is around $z \approx 1$. This leads to a constant that is only dependent on q, allowing the integral to be calculated once per q. Thus, we have the approximation

$$\overline{P}(\theta) \approx \frac{4}{\alpha}(\sin\theta)^{q-5}\,\mathcal{J}_0^\infty(q)\,,\ \theta_2 \leq \theta \leq \theta_1. \tag{A.6}$$

The $\mathcal{J}_0^\infty(q)$ in Equation A.6 is shorthand for $\int_0^\infty z^{2-q}J_1(z)^2\,dz$. It is nearly constant over the range of $2 \leq q \leq 5$, except when q approaches 2 or 5. Previous studies indicate that q is between 2.7 and 3.1 within the main rings, giving $J_0^\infty \approx 0.5$ (Zebker et al. 1985, French and Nicholson 2000, Cuzzi et al. 2009).

BIBLIOGRAPHY

G J Black, Philip D Nicholson, and Peter C Thomas. Hyperion: Rotational dynamics. *Icarus*, 117(1):149–161, September 1995.

Anna Bodrova, Jürgen Schmidt, Frank Spahn, and Nikolai V Brilliantov. Adhesion and collisional release of particles in dense planetary rings. *Icarus*, 218 (1):60–68, March 2012.

Robert H Brown, Kevin H Baines, G Bellucci, J-P Bibring, Bonnie J Buratti, F Capaccioni, P Cerroni, Roger N Clark, Angioletta Coradini, Dale P Cruikshank, Pierre Drossart, V Formisano, Ralf Jaumann, Y Langevin, Dennis L Matson, Thomas B McCord, V Mennella, E Miller, Robert M Nelson, Philip D Nicholson, Bruno Sicardy, and C Sotin. The Cassini Visual And Infrared Mapping Spectrometer (VIMS) Investigation. *Space Science Reviews*, 115:111–168, 2004.

Joshua E Colwell, Larry W Esposito, and Miodrag Sremčević. Self-gravity wakes in Saturn's A ring measured by stellar occultations from Cassini. *Geophysical Research Letters*, 33(7):7201–7204, April 2006.

Joshua E Colwell, Philip D Nicholson, Matthew S Tiscareno, Carl D Murray, Richard G French, and Essam A Marouf. The Structure of Saturn's Rings. In Michele Dougherty, Larry W Esposito, and Stamatios Krimigis, editors, *Saturn from Cassini-Huygens*, chapter 13, pages 375–412. Springer, 2009.

Maren Leyla Cooke. Saturn's rings: Photometric studies of the C Ring and radial variation in the Keeler Gap. *Ph.D. Thesis Cornell Univ., Ithaca, NY.*, 1991.

Jeffrey N Cuzzi. Rings of Uranus - Not so thick, not so black. *Icarus*, 63:312–316, August 1985.

Jeffrey N Cuzzi and J B Pollack. Saturn's rings: Particle composition and size distribution as constrained by microwave observations. I - Radar observations. *Icarus*, 33:233–262, February 1978.

Jeffrey N Cuzzi, J B Pollack, and A L Summers. Saturn's rings - Particle composition and size distribution as constrained by observations at microwave wavelengths. II - Radio interferometric observations. *Icarus*, 44:683–705, December 1980.

Jeffrey N Cuzzi, Roger N Clark, Gianrico Filacchione, Richard G French, Robert E Johnson, Essam A Marouf, and Linda J Spilker. Ring Particle Composition and Size Distribution. In Michele Dougherty, Larry W Esposito, and Stamatios Krimigis, editors, *Saturn from Cassini-Huygens*, pages 459–509. Springer, 2009.

E D'Aversa, G Bellucci, Philip D Nicholson, Matthew M Hedman, Robert H Brown, Mark R Showalter, F Altieri, F G Carrozzo, Gianrico Filacchione, and F Tosi. The spectrum of a Saturn ring spoke from Cassini/VIMS. *Geophysical Research Letters*, 37(1):1203–1207, January 2010.

Luke Dones, Jeffrey N Cuzzi, and Mark R Showalter. Voyager photometry of Saturn's A ring. *Icarus*, 105:184–215, September 1993.

L R Doyle, Luke Dones, and Jeffrey N Cuzzi. Radiative transfer modeling of Saturn's outer B ring. *Icarus*, 80:104–135, July 1989.

L Duriez and A Vienne. Theory of motion and ephemerides of Hyperion. *Astronomy and Astrophysics*, 324:366, August 1997.

Gianrico Filacchione, F Capaccioni, M Ciarniello, Roger N Clark, Jeffrey N Cuzzi, Philip D Nicholson, Dale P Cruikshank, Matthew M Hedman, Bon-

nie J Buratti, J I Lunine, L A Soderblom, F Tosi, P Cerroni, Robert H Brown, Thomas B McCord, Ralf Jaumann, K Stephan, Kevin H Baines, and E Flamini. Saturn's icy satellites and rings investigated by Cassini–VIMS: III – Radial compositional variability. *Icarus*, 220(2):1064–1096, August 2012.

Gianrico Filacchione, F Capaccioni, Roger N Clark, Philip D Nicholson, Dale P Cruikshank, Jeffrey N Cuzzi, J I Lunine, Robert H Brown, P Cerroni, F Tosi, M Ciarniello, Bonnie J Buratti, Matthew M Hedman, and E Flamini. The radial distribution of water ice and chromophores across Saturn's system. *The Astrophysical Journal*, 766(2):76, April 2013.

Grant R Fowles and George L Cassiday. *Analytical Mechanics: Sixth Edition*. Thomson Learning, Inc., 1999.

Richard G French and Philip D Nicholson. Saturn's Rings II. Particle sizes inferred from stellar occultation data. *Icarus*, 145:502–523, 2000.

Richard G French, Philip D Nicholson, Maren Leyla Cooke, J L Elliot, K Matthews, O Perkovic, E Tollestrup, P Harvey, N J Chanover, M A Clark, E W Dunham, W Forrest, J Harrington, J Pipher, A Brahic, I Grenier, F Roques, and M Arndt. Geometry of the Saturn system from the 3 July 1989 occultation of 28 SGR and Voyager observations. *Icarus*, 103:163–214, 1993.

Rebecca A Harbison, Philip D Nicholson, and Matthew M Hedman. The smallest particles in Saturn's A and C rings. *Icarus*, 226(2):1225–1240, September 2013.

Matthew M Hedman, Joseph A Burns, Mark R Showalter, Carolyn C Porco, Philip D Nicholson, Amanda S. Bosh, Matthew S Tiscareno, Robert H Brown,

Bonnie J Buratti, Kevin H Baines, and Roger N Clark. Saturn's dynamic D ring. *Icarus*, 188(1):89–107, May 2007a.

Matthew M Hedman, Joseph A Burns, Matthew S Tiscareno, and Carolyn C Porco. The heliotropic rings of Saturn. *American Astronomical Society*, 39:427–427, October 2007b.

Matthew M Hedman, Philip D Nicholson, Heikki J Salo, and B D Wallis. Self-gravity wake structures in Saturn's A ring revealed by Cassini VIMS. *The Astrophysical Journal*, 133:2624–2629, June 2007c.

Matthew M Hedman, Jennifer A Burt, Joseph A Burns, and Matthew S Tiscareno. The shape and dynamics of a heliotropic dusty ringlet in the Cassini Division. *Icarus*, 210(1):284–297, November 2010a.

Matthew M Hedman, Philip D Nicholson, Kevin H Baines, Bonnie J Buratti, C Sotin, Roger N Clark, Robert H Brown, Richard G French, and Essam A Marouf. The architecture of the Cassini Division. *Astronomical Journal*, 139(1): 228–251, January 2010b.

Matthew M Hedman, Philip D Nicholson, Mark R Showalter, Robert H Brown, Bonnie J Buratti, Roger N Clark, Kevin H Baines, and C Sotin. The Christiansen Effect in Saturn's narrow dusty rings and the spectral identification of clumps in the F ring. *Icarus*, 215(2):695–711, October 2011.

James Jay Klavetter. Rotation of Hyperion. II - Dynamics. *Astronomical Journal*, 98:1855, November 1989.

Mark C Lewis and Glen R Stewart. Expectations for Cassini observations of ring material with nearby moons. *Icarus*, 178(1):124–143, November 2005.

K N Liou. *An introduction to atmospheric radiation.* Academic Press, 1980.

P Y Longaretti. Saturn's main ring particle size distribution - an analytic approach. *Icarus*, 81:51–73, September 1989.

C B Markwardt. Non-linear least-squares fitting in IDL with MPFIT. In D A Bohlender, D Durand, and P Dowler, editors, *arXiv.org*, pages 251–255, 2009.

Essam A Marouf, G L Tyler, and V R Eshleman. Theory of radio occultation by Saturn's rings. *Icarus*, 49:161–193, February 1982.

Essam A Marouf, G L Tyler, H A Zebker, R A Simpson, and V R Eshleman. Particle size distributions in Saturn's rings from Voyager 1 radio occultation. *Icarus*, 54:189–211, 1983.

Essam A Marouf, R French, N Rappaport, K Wong, C McGhee, and A Anabtawi. Physical properties of Saturn's rings from Cassini radio occultations. In *AAS/Division for Planetary Sciences Meeting Abstracts*, page 429, 2008.

A V Melnikov and I I Shevchenko. On the rotational dynamics of Prometheus and Pandora. *Celestial Mechanics and Dynamical Astronomy*, 101:31, May 2008.

C J Mitchell, M Horányi, O Havnes, and C C Porco. Saturn's spokes: Lost and found. *Science*, 311(5767):1587–1589, March 2006.

C J Mitchell, Carolyn C Porco, H L Dones, and J N Spitale. The behavior of spokes in Saturn's B ring. *Icarus*, 225(1):446–474, July 2013.

Ryuji Morishima, Scott G Edgington, and Linda J Spilker. Regolith grain sizes of Saturn's rings inferred from Cassini-CIRS far-infrared spectra. *Icarus*, 221 (2):888–899, November 2012.

Philip D Nicholson and Matthew M Hedman. Self-gravity wake parameters in Saturn's A and B rings. *Icarus*, 206:410–423, April 2010.

Philip D Nicholson, Richard G French, Donald B Campbell, Jean-Luc Margot, Michael C Nolan, Gregory J Black, and Heikki J Salo. Radar imaging of Saturn's rings. *Icarus*, 177(1):32–62, September 2005.

Philip D Nicholson, Matthew M Hedman, Roger N Clark, Mark R Showalter, Dale P Cruikshank, Jeffrey N Cuzzi, Gianrico Filacchione, F Capaccioni, P Cerroni, Gary B Hansen, Bruno Sicardy, Pierre Drossart, Robert H Brown, Bonnie J Buratti, Kevin H Baines, and Angioletta Coradini. A close look at Saturn's rings with Cassini VIMS. *Icarus*, 193:182–212, 2008.

S J Peale. Origin and evolution of the natural satellites. *Annual Review of Astronomy and Astrophysics*, 37:533–602, 1999.

F Roques, M Moncuquet, and B Sicardy. Stellar occultations by small bodies - Diffraction effects. *Astronomical Journal*, 93:1549–1558, June 1987.

Heikki J Salo. Gravitational wakes in Saturn's rings. *Nature*, 359:619–621, October 1992.

M Seiß, F Spahn, Miodrag Sremčević, and H Salo. Structures induced by small moonlets in Saturn's rings: Implications for the Cassini Mission. *Geophysical Research Letters*, 32(1):11205, June 2005.

Mark R Showalter and Philip D Nicholson. Saturn's rings through a microscope: Particle size constraints from the Voyager PPS scan. *Icarus*, 1990.

F Spahn, Jürgen Schmidt, and Miodrag Sremčević. Structures in planetary rings stability and gravitational scattering. *Stochastic Processes in Physics*, 557:507, 2000.

Linda J Spilker, S G Edgington, B D Wallis, S M Brooks, J C Pearl, and F M Flasar.

Cassini CIRS observations of a roll-off in Saturn ring spectra at submillimeter wavelengths. *Earth, Moon, and Planets*, 96:149–163, June 2005.

J N Spitale and Carolyn C Porco. Detection of free unstable modes and massive bodies in Saturn's outer B ring. *Astronomical Journal*, 140(6):1747–1757, December 2010.

Miodrag Sremčević, Jürgen Schmidt, Heikki Salo, Martin Seiß, Frank Spahn, and Nicole Albers. A belt of moonlets in Saturn's A ring. *Nature*, 449(7): 1019–1021, October 2007.

Peter C Thomas, J W Armstrong, S W Asmar, Joseph A Burns, Tilmann Denk, B Giese, Paul Helfenstein, L Iess, T V Johnson, A S McEwen, L Nicolaisen, Carolyn C Porco, Nicole J Rappaport, J Richardson, L Somenzi, P Tortora, E P Turtle, and J Veverka. Hyperion's sponge-like appearance. *Nature*, 448:50, July 2007.

Matthew S Tiscareno, Joseph A Burns, Matthew M Hedman, Carolyn C Porco, John W Weiss, Luke Dones, Derek C Richardson, and Carl D Murray. 100-metre-diameter moonlets in Saturn's A ring from observations of 'propeller' structures. *Nature*, 440(7):648–650, March 2006.

Matthew S Tiscareno, Joseph A Burns, and Matthew M Hedman. Propeller population in Saturn's A ring. *Astronomical Journal*, 135:1083–1091, 2008.

Matthew S Tiscareno, Joseph A Burns, Miodrag Sremčević, Kevin Beurle, Matthew M Hedman, Nicholas J Cooper, Anthony J Milano, Michael W Evans, Carolyn C Porco, Joseph N Spitale, and John W Weiss. Physical characteristics and non-Keplerian orbital motion of "propeller" moons embedded in Saturn's rings. *The Astrophysical Journal Letters*, 718(2):L92–L96, August 2010a.

Matthew S Tiscareno, Randall P Perrine, Derek C Richardson, Matthew M Hedman, John W Weiss, Carolyn C Porco, and Joseph A Burns. An analytic parameterization of self-gravity wakes in Saturn's rings, with application to occultations and propellers. *Astronomical Journal*, 139(2):492–503, February 2010b.

Sanaz Vahidinia, Jeffrey N Cuzzi, Matt Hedman, Bruce Draine, Roger N Clark, Ted Roush, Gianrico Filacchione, Philip D Nicholson, Robert H Brown, Bonnie J Buratti, and Christophe Sotin. Saturn's F ring grains: Aggregates made of crystalline water ice. *Icarus*, 215(2):682–694, October 2011.

J Wisdom, S J Peale, and F Mignard. The chaotic rotation of Hyperion. *Icarus*, 58:137–152, May 1984.

H A Zebker, Essam A Marouf, and G L Tyler. Saturn's rings - Particle size distributions for thin layer model. *Icarus*, 64:531–548, 1985.